

Cluster Dynamical Mean-Field Theory:  
Applications to High- $T_c$  Cuprates  
and to Quantum Chemistry

Nan Lin

Submitted in partial fulfillment of the  
Requirements for the degree  
of Doctor of Philosophy  
in the Graduate School of Arts and Sciences

COLUMBIA UNIVERSITY

2012

© 2012

Nan Lin

All Rights Reserved

# Abstract

## Cluster Dynamical Mean-Field Theory: Applications to High- $T_c$ Cuprates and to Quantum Chemistry

Nan Lin

In this thesis we use the recently developed dynamical mean-field approximation to study problems in strongly correlated electron systems, including high- $T_c$  cuprate superconductors as well as a few quantum chemical reference systems.

We start with an introduction to the background of the interacting electron systems, followed by a brief description on the current understanding of the physics of high- $T_c$  cuprate superconductors. The approximate models that enter the theoretical framework will be discussed afterwards. Some quantum chemical methods for many-body quantum systems are included for review.

Next we present the numerical methods employed in our study. The formalism of the dynamical mean-field approximation will be introduced including the single-site and cluster versions, followed by the Exact Diagonalization impurity solver for the solution of the quantum impurity model. Maximum Entropy analytic continuation method is also discussed, which is useful to obtain the physically relevant response functions.

Then we apply dynamical mean-field approximation to high- $T_c$  cuprate superconductors. The two-particle response functions, such as Raman scattering intensity and optical conductivity, are computed for the two dimensional Hubbard model. The

calculations include the vertex corrections which are essential to obtain physically reasonable results in interacting electron systems. We also study the physics of the pseudogap in cuprates. The suppression of density of states near Fermi surface is present in our calculations, which is in qualitative agreement with the experimental data.

Finally we discuss the application of dynamical mean-field theory to quantum chemistry. We extend the formalism of dynamical mean-field approximation to finite systems, and compare its performance in hydrogen clusters with different spatial configurations to other leading quantum chemical approaches. Dynamical mean-field theory involves mapping onto a quantum impurity model. We further examine the quantum impurity model representation of the transition metal dioxide molecules. The conceptual and technical difficulties will be discussed.

# Contents

<b>Contents</b>	<b>i</b>
<b>List of Tables</b>	<b>iv</b>
<b>List of Figures</b>	<b>v</b>
<b>1 Introduction</b>	<b>1</b>
1.1 Overview . . . . .	1
1.2 Interacting Electron Systems . . . . .	1
1.3 Cuprate Superconductors . . . . .	3
1.4 Molecular Orbital Theory . . . . .	8
1.4.1 Hartree-Fock method . . . . .	8
1.4.2 Post-Hartree-Fock Methods . . . . .	10
<b>2 Numerical Methods</b>	<b>15</b>
2.1 Overview . . . . .	15
2.2 Dynamical Mean-Field Theory . . . . .	15
2.2.1 Sketch of the procedure . . . . .	16
2.2.2 Cluster DMFT . . . . .	18
2.3 Exact Diagonalization . . . . .	24
2.4 Analytic Continuation . . . . .	26
<b>3 Two-Particle Response Functions</b>	<b>33</b>
3.1 Overview . . . . .	33

3.2	Introduction . . . . .	33
3.3	Model and Methods . . . . .	35
3.4	Raman Scattering . . . . .	45
3.4.1	Isolated Cluster . . . . .	46
3.4.2	Two Dimensional Square Lattice . . . . .	49
3.5	Optical Conductivity . . . . .	57
3.5.1	4-site DCA . . . . .	57
3.5.2	8-site DCA . . . . .	64
3.6	Summary . . . . .	67
<b>4</b>	<b>Pseudogap in Cuprates</b>	<b>69</b>
4.1	Overview . . . . .	69
4.2	Introduction . . . . .	69
4.3	Model and Methods . . . . .	73
4.4	Electron Spectral Function . . . . .	77
4.5	Interplane Conductivity . . . . .	80
4.6	Raman Scattering Intensity . . . . .	83
4.7	In-plane Conductivity . . . . .	87
4.8	Electron Self-Energy . . . . .	92
4.9	Discussion . . . . .	100
<b>5</b>	<b>Quantum Chemistry</b>	<b>103</b>
5.1	Overview . . . . .	103
5.2	Introduction: Quantum Chemistry . . . . .	103
5.3	Formalism . . . . .	105
5.4	Hydrogen Cluster . . . . .	110
5.5	Transition Metal Dioxides . . . . .	116
5.6	Summary . . . . .	125

<b>A</b>	<b>Note on the technical details for computing the vertex correction</b>	<b>126</b>
A.1	Two dimensional Fourier transform . . . . .	126
A.2	Symmetry . . . . .	128
A.3	Data Storing . . . . .	130
A.4	The Covariance . . . . .	132
<b>B</b>	<b>Note on the non-orthogonal basis set</b>	<b>134</b>
<b>C</b>	<b>Note on the fitting of the bare Green's function in the ED solver</b>	<b>136</b>
	<b>Bibliography</b>	<b>138</b>
	<b>Curriculum Vitae</b>	<b>158</b>

# List of Tables

4.1	Integrated spectral weight of interplane optical conductivity in 8-site DCA approximation to 2d Hubbard model . . . . .	82
4.2	Integrated spectral weight of low frequency in-plane optical conductivity in 8-site DCA approximation to 2d Hubbard model . . . . .	89
5.1	Comparison of different approximations in the reduced model for the collinear CrO <sub>2</sub> molecule . . . . .	123



# List of Figures

1.1	Crystal structure of $\text{La}_2\text{CuO}_4$ and $\text{Nd}_2\text{CuO}_4$ parent compounds . . .	4
1.2	Phase diagram of hole- and electron-doped cuprate superconductors .	5
2.1	Sketch of the DMFT self-consistency loop . . . . .	17
2.2	The coordinates for $2 \times 2$ clusters in real and reciprocal space . . . .	19
2.3	Example of the constructed $L$ -curve in Maximum Entropy analytic continuation . . . . .	29
2.4	Analytically continued $\text{Im}\Sigma(\omega)$ in 8-site DCA approximation to 2d Hubbard model . . . . .	30
2.5	Spectral function in 8-site DCA approximation to 2d Hubbard model	31
3.1	Feynman Diagrams corresponding to computation of the two-particle response function . . . . .	37
3.2	Brillouin-zone partitioning associated with different clusters . . . . .	38
3.3	Polarization orientations for Raman $B_{1g}$ and $B_{2g}$ scattering channels .	45
3.4	Raman $B_{1g}$ scattering intensity in isolated 8-site cluster . . . . .	47
3.5	Raman $B_{1g}$ scattering intensity in isolated 4-site cluster . . . . .	48
3.6	Interaction dependence of Raman $B_{1g}$ scattering in 4-site DCA approximation to 2d Hubbard model . . . . .	49
3.7	Temperature dependence of the Raman $B_{1g}$ scattering in 8-site DCA approximation to half-filled 2d Hubbard model . . . . .	50
3.8	Cluster dependence of the Raman $B_{1g}$ scattering in DCA approximation to 2d Hubbard model . . . . .	51

3.9	Doping dependence of the Raman $B_{1g}$ scattering in 8-site DCA approximation to 2d Hubbard model . . . . .	52
3.10	Decomposition of the Raman $B_{1g}$ scattering in 8-site DCA approximation to 2d Hubbard model . . . . .	53
3.11	Temperature dependence of the Raman $B_{1g}$ scattering in 8-site DCA approximation to the doped 2d Hubbard model . . . . .	54
3.12	Doping dependence of the Raman $B_{2g}$ scattering in 8-site DCA approximation to 2d Hubbard model . . . . .	55
3.13	Doping and temperature dependence of the “reinterpreted” optical conductivity in 8-site DCA approximation to 2d Hubbard model . . . . .	55
3.14	Raman scattering intensity in the high doping “isotropic Fermi liquid” region in 8-site DCA approximation to 2d Hubbard model . . . . .	56
3.15	Optical conductivity in 4-site DCA approximation to 2d Hubbard model	59
3.16	Doping dependence of the optical conductivity in 4-site DCA approximation to 2d Hubbard model . . . . .	60
3.17	Spectral function in the 4-site DCA approximation to 2d Hubbard model	62
3.18	Current-current response function in 8-site DCA approximation to 2d Hubbard model . . . . .	66
4.1	Brillouin zone partitioning associated with the 8-site cluster. . . . .	75
4.2	Temperature dependence of the many-body density of states averaged over sector $C$ in 8-site DCA approximation to 2d Hubbard model . . . . .	78
4.3	Doping dependence of the many-body density of states averaged over sector $B$ and $C$ in 8-site DCA approximation to 2d Hubbard model . . . . .	79
4.4	Temperature and doping dependence of the interplane conductivity in 8-site DCA approximation to 2d Hubbard model . . . . .	81
4.5	Temperature dependence of the Raman $B_{1g}$ and $B_{2g}$ scattering intensity in 8-site DCA approximation to 2d Hubbard model . . . . .	84

4.6	Doping dependence of the Raman $B_{1g}$ scattering intensity in 8-site DCA approximation to 2d Hubbard model . . . . .	86
4.7	Doping dependence of the Raman $B_{2g}$ scattering intensity in 8-site DCA approximation to 2d Hubbard model . . . . .	86
4.8	Doping and temperature dependence of the in-plane optical conductivity in 8-site DCA approximation to 2d Hubbard model . . . . .	88
4.9	Contribution to the in-plane optical conductivity from sector $B$ and $C$ in 8-site DCA approximation to 2d Hubbard model . . . . .	89
4.10	Temperature dependence of the optical scattering rate in 8-site DCA approximation to 2d Hubbard model . . . . .	91
4.11	Temperature dependence of sector $B$ and $C$ self-energy at low doping	93
4.12	Temperature dependence of sector $B$ and $C$ self-energy at high doping	94
4.13	Electron self-energy computed for sector $B$ in 8-site DCA approximation to 2d Hubbard model . . . . .	95
4.14	Electron self-energy computed for sector $C$ in 8-site DCA approximation to 2d Hubbard model . . . . .	96
4.15	Illustration of the determination of Fermi-liquid behavior . . . . .	97
4.16	Quasiparticle residue $Z$ in 8-site DCA approximation to 2d Hubbard model . . . . .	99
4.17	Doping dependence of the pseudogap size in 8-site DCA approximation to 2d Hubbard model . . . . .	101
5.1	Sketch of the DMFT method in finite systems . . . . .	109
5.2	Potential energy curves for the dissociation of $H_6$ chain and ring . . .	111
5.3	Potential energy curve for the dissociation of $H_{50}$ chain . . . . .	113
5.4	Potential energy curve for the dissociation of tetrahedrally configured $H_4$ . . . . .	114
5.5	Electron spectral function for $H_6$ ring . . . . .	115

5.6	RHF solutions for the collinear TiO <sub>2</sub> molecule . . . . .	118
5.7	Comparison of ground state energies for the collinear TiO <sub>2</sub> molecule .	119
5.8	Comparison of Ti 3 <i>d</i> -orbital occupancy in the collinear TiO <sub>2</sub> molecule	120
5.9	Comparison of ground state energies for the collinear TiO <sub>2</sub> molecule .	121
5.10	Comparison of Cr 3 <i>d</i> -orbital occupancy in the collinear CrO <sub>2</sub> molecule	122
5.11	Excitation spectra for the collinear CrO <sub>2</sub> molecule . . . . .	123
A.1	Characteristic four-point function for Raman <i>B</i> <sub>1<i>g</i></sub> scattering . . . . .	130
A.2	Consuming time of the four-point function measurement . . . . .	131
A.3	Characteristic covariance matrix for the two-particle response function	132
C.1	Fitting of a non-diagonal bare Green's function . . . . .	136

## Acknowledgments

First and foremost, I would like to thank my advisors, Prof. Andrew J. Millis in Department of Physics and Prof. David R. Reichman in Department of Chemistry, Columbia University. This thesis would not have been possible without their solid support throughout these years. Their profound breadth and depth of knowledge, inspiring guidance, and encouragement have always been a source of confidence and inspiration. From discussions with them, whether in office or online, I have not only learned physics, but also the way in which research should be done.

Next I would like to thank Prof. Chris A. Marianetti in Department of Applied Physics, Columbia University. He has been very helpful in the projects we worked on together. I am grateful for the enlightening discussions with him. I would also like to thank Dr. Emanuel Gull and Dr. Dominika Zgid. The collaborations with them are very enjoyable and fruitful. They are always very patient and responsive, answering my questions and motivating me. From our research group, I benefit a lot from the discussions with Dr. Xin Wang, Hung Dang and Junichi Okamoto.

I am grateful to Professors Igor Aleiner, Tony F. Heinz and Irving P. Herman for serving on my dissertation defense committee. I also want to take this opportunity to thank all the faculty members in Physics Department. I own special thanks to Prof. Philip Kim for his great help and

understanding in my first two years at Columbia, and Prof. Allan Blaer for offering a lot of suggestions.

Last but not least, a sincere thank you to my parents Daiwei Lin and Fen Chen, my sister Luan Lin and my boyfriend Nanshi Sha, for their unconditional love, dedication and support in my life. They are always behind me in the pursuit of my goals. Without their everlasting understanding, this endeavor would have been much more challenging.

To my family

# Chapter 1

## Introduction

### 1.1 Overview

In this thesis, we focus on two main topics: the investigation of the correlated electron systems with applications to the high-temperature cuprate superconductors, and the numerical study of the quantum chemical systems. Our calculations rely on the recently developed dynamical mean-field theory. This chapter is an introduction to this thesis. We shall begin with some general remarks of “strongly correlated electron systems” in Sec. 1.2. In Sec. 1.3 we will describe the fundamental aspects of cuprate superconductors, whose study is a topic of active theoretical and experimental research and constitutes one of the main topics of this thesis. We will introduce the one-band Hubbard model on the two-dimensional square lattice as the simplest model describing cuprates. We briefly review a few existing quantum chemical approaches for many-body systems in Sec. 1.4.

### 1.2 Interacting Electron Systems

In solid state physics, band theory explains qualitative difference between metals and insulators [[Bethe \(1928\)](#); [Sommerfeld \(1928\)](#); [Bloch \(1929\)](#)] using a model of non-interacting (or weakly interacting) electrons. In a single isolated atom the electrons



occupy atomic orbitals, which form a discrete set of energy levels; while in solids the energy bands are continuous with band gaps in between which are ranges of energy where no electron states can exist. The energy bands are occupied by electrons, starting from lowest and upwards. Band theory says that if the highest filled band is partially filled, the system will be metallic, otherwise if the highest filled band is completely filled, the system will be insulating. These original ideas have been refined to describe many experimental observations. However, major challenge arises for a system of many strongly interacting electrons.

Strongly correlated electron systems [Imada et al. (1998)], those materials with strong electron interactions, have attracted much attention in both communities of condensed matter physics and quantum chemistry. Conventional approaches, such as the Fermi liquid theory and the local density approximation to the density functional theory [Hohenberg and Kohn (1964); Kohn and Sham (1965)], fail to completely describe the behavior of such systems.

One of the earliest problems that caught attention is the transition metal oxides [de Boer and Verwey (1937)]. The  $d$ -shells of transition metal oxides are partially filled, therefore they should be metallic according to band theory. However, the transition metal oxides are usually found to be poor conductors and often insulating. Proposed by Mott and Peierls (1937), this behavior was due to the presence of strong Coulomb repulsion between electrons which would have significant effect on the physics of such materials. In his subsequent work, Mott (1949, 1956) showed that the strong Coulomb repulsion between two electrons occupying the same site might result in an insulating state, what is now called “Mott insulators”. Later the Hubbard model [Hubbard (1963)], which is an approximate model for the interaction between electrons in narrow energy bands (e.g.  $d$ - and  $f$ - bands), was introduced. By varying the strength of the on-site Coulomb repulsion, the transition between metallic and insulating states occurs, known as the “Mott transition”. A general study of the

metal-insulator transition was presented in [Mott \(1968\)](#).

There has been increasing theoretical interest in strongly correlated electron systems since the discovery of “high-temperature cuprate superconductors” by [Bednorz and Müller \(1986\)](#), which has been one of the most intensively studied materials since then. The unprecedented high transition temperature  $T_c$  [[Schilling et al. \(1993\)](#)] and other abnormal properties are mysterious to researchers. In cuprates the copper  $d_{x^2-y^2}$  orbital is half-filled, and the strong Coulomb repulsion on this orbital prevents electrons from moving through the lattice. Therefore the high- $T_c$  cuprate superconductors were identified as Mott insulators. However, [Zaanen et al. \(1985\)](#) took the neighboring oxygen sites into account and classified the cuprates as charge-transfer insulators rather than Mott insulators. The investigation of the strength of the on-site Coulomb repulsion and the nature of the insulating state remains an active research area [[Gull et al. \(2008b\)](#); [de’ Medici et al. \(2009\)](#)].

Apart from the crystalline systems in condensed matter physics, it is also challenging to describe the strong correlations in molecular systems, such as the breaking of chemical bonds, and transition metal clusters. Chap. 5 will be related to quantum chemistry.

## 1.3 Cuprate Superconductors

Johannes Bednorz and Karl Müller were the 1987 Nobel Prize laureates in Physics for their discovery of the high- $T_c$  superconductivity at 30 K in a LaBaCuO system [[Bednorz and Müller \(1986\)](#)]. Until recent discovery of iron-based superconductors [[Takahashi et al. \(2008\)](#)], most high-temperature superconductors were copper oxide compounds (also known as “cuprates”), which are quasi-two-dimensional materials characterized by copper-oxide ( $\text{CuO}_2$ ) layers. Currently the record for the highest

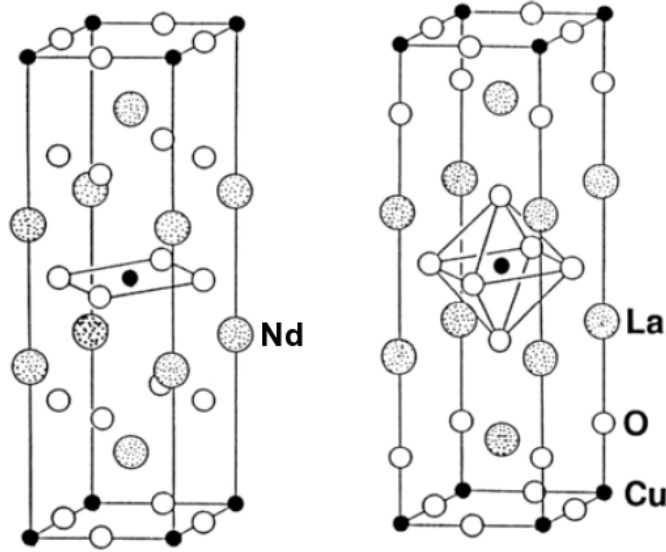


**Figure 1.1:** Crystal structure of  $\text{La}_2\text{CuO}_4$  and  $\text{Nd}_2\text{CuO}_4$  parent compounds. Reproduced from [Maple et al. \(2008\)](#).

value of  $T_c$  ( $\sim 133$  K) is held by the mercury-based compound  $\text{HgBa}_2\text{Ca}_2\text{Cu}_3\text{O}_{8+x}$  (Hg-1223) [[Schilling et al. \(1993\)](#)].

Fig. 1.1 shows the crystal structures of the  $\text{La}_2\text{CuO}_4$  and  $\text{Nd}_2\text{CuO}_4$  parent compounds. Both compounds have a tetragonal crystal structure and are single  $\text{CuO}_2$  layer compounds with one  $\text{CuO}_2$  plane per unit cell, but  $\text{Nd}_2\text{CuO}_4$  has no apical oxygen atoms. It is generally believed that the  $\text{CuO}_2$  planes dominate the physics of high-temperature cuprate superconductors.

The undoped cuprate is an insulator in its ground state, while doping with charge carriers (holes or electrons) renders metallic behavior or superconductivity. For example, the  $\text{CuO}_2$  planes are doped with mobile holes by substituting divalent Sr for trivalent La in  $\text{La}_2\text{CuO}_4$ . Similarly, when some of trivalent Nd in  $\text{Nd}_2\text{CuO}_4$  is substituted by tetravalent Ce, electrons are introduced to the  $\text{CuO}_2$  planes.

Fig. 1.2 displays the temperature-dopant concentration phase diagram for the hole-doped  $\text{La}_{2-x}\text{Sr}_x\text{CuO}_4$  and electron-doped  $\text{Nd}_{2-x}\text{Ce}_x\text{CuO}_4$  systems. One immediately sees a number of common elements in both the hole- and electron-doped materials.

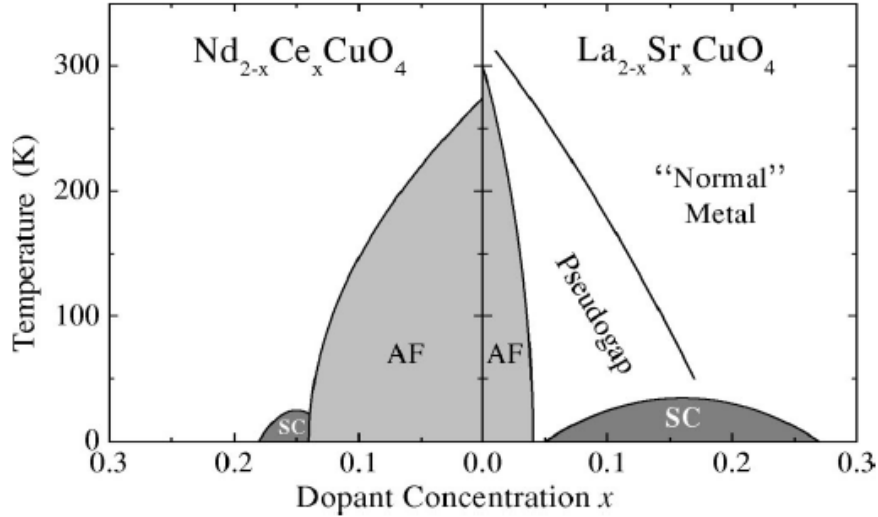


**Figure 1.2:** Temperature-dopant concentration phase diagram of hole- and electron-doped cuprate superconductors, showing antiferromagnetic phase (AF), superconducting phase (SC), pseudogap and normal metal regions. Reproduced from [Damascelli et al. \(2003\)](#).

The parent compounds are both in the antiferromagnetic insulating phase. The antiferromagnetic ordering is seen to persist in a wider range of doping in electron-doped  $\text{Nd}_{2-x}\text{Ce}_x\text{CuO}_4$  material. The superconductivity is observed above a critical doping level under the transition temperature  $T_c$ . The transition temperature increases with doping (underdoped regime) and reaches the maximum value at the optimal doping, then decreases when the doping level is further increased (overdoped region). The maximum value of  $T_c$  is  $\sim 40$  K at  $x \approx 0.17$  in  $\text{La}_{2-x}\text{Sr}_x\text{CuO}_4$  [[Cava et al. \(1987\)](#)] and  $\sim 25$  K at  $x \approx 0.15$  in  $\text{Nd}_{2-x}\text{Ce}_x\text{CuO}_4$  [[Tokura et al. \(1989\)](#)]. The compounds are in a “normal metal” region at high temperature and doping level. When the temperature is sufficiently high (above the Néel temperature), the antiferromagnetism is absent even in the undoped case.

A remarkable difference between the hole- and electron-doped materials is the presence of the pseudogap region on the hole-doped side of the phase diagram. In the

pseudogap region, a temperature and doping dependent gap in the density of states is developed, which is visible well above the superconducting transition temperature, but below the onset temperature  $T^*$  [Timusk and Statt (1999)]. The pseudogap was first inferred from measurements of the NMR spin-lattice relaxation rate and NMR Knight shift in underdoped  $\text{YBa}_2\text{Cu}_3\text{O}_{6+x}$  samples [Warren et al. (1989); Alloul et al. (1989)], and later from various transport, thermal, magnetic and spectroscopic measurements. The origin of the pseudogap is still in dispute. In Chap. 4 we present a study of the physics of the pseudogap.

In the hole-doped high- $T_c$  cuprate compounds such as  $\text{La}_{2-x}\text{Sr}_x\text{CuO}_4$ , the degeneracy of the Cu  $3d$  orbitals as in free space is lifted as a result of the Jahn-Teller distortion of the  $\text{CuO}_6$  octahedra. The Cu  $3d$  levels are split into a doublet  $e_g = d_{x^2-y^2}, d_{3z^2-r^2}$  and a triplet  $t_{2g} = d_{xy}, d_{xz}, d_{yz}$  states due to the cubic crystal field. When the tetragonal symmetry as in cuprates is applied, the orbitals are further split into singlets  $d_{x^2-y^2}, d_{3z^2-r^2}, d_{xy}$  and a doublet consisting of  $d_{xz}$  and  $d_{yz}$ . The electronic configurations for  $\text{Cu}^{2+}$  and  $\text{O}^{2-}$  ions in cuprates are copper  $3d^9$  and oxygen  $2p^6$ , therefore the Cu  $d_{x^2-y^2}$  orbital which has the highest energy among the five Cu  $3d$  levels is half-filled, while the Cu  $t_{2g}$  and  $d_{3z^2-r^2}$  orbitals and the oxygen  $p$  orbitals are completely filled. The one-band Hubbard model

$$H_{ij} = \sum_{ij\sigma} t_{ij} d_{i\sigma}^\dagger d_{j\sigma} + U \sum_i n_{i\uparrow} n_{i\downarrow} \quad (1.1)$$

serves as the simplest approximate model for the cuprate compounds in which we retain the Cu  $d_{x^2-y^2}$  orbital and neglect other Cu orbitals and all O orbitals. In Eq. 1.1  $t_{ij}$  denotes the hopping energy between sites and  $U$  is the strong on-site correlation between electrons which is generally believed to play an important role in the description of the physics of the cuprates. Our work presented in Chap. 3 and 4 follows by approximating the copper oxide compounds by one-band Hubbard model.

de' Medici et al. (2009) and Wang et al. (2011b) presented a dynamical mean-field study of the three band model including both Cu  $d_{x^2-y^2}$  and planar O  $2p_{x,y}$  orbitals. In Wang et al. (2011a) a six band model of high- $T_c$  cuprate superconductors is solved which further includes Cu  $d_{3z^2-r^2}$  orbital and two apical oxygen orbitals.

However, the solution of the simplified Hubbard model is still theoretically challenging, with an exception in the one-dimensional case which was solved by Lieb and Wu (1968, 2003) using the Bethe ansatz. The non-perturbative nature in the vicinity of the metal-insulator transition limits the applicability of approximate analytical methods such as the perturbation theory expansion. A more quantitative study of the correlation physics in the region around the transition between the metallic and insulating states was enabled by the availability of the advanced high performance computing systems. Nevertheless the numerical methods, such as exact diagonalization (ED) or quantum Monte Carlo (QMC), also have limitations, either because the size of the Hilbert space (and therefore the size of the matrix to be diagonalized) grows exponentially with the system size in the case of ED or the fermionic sign problem limits the standard lattice QMC calculations to high temperatures.

The recently developed dynamical mean-field theory (DMFT) accumulates much research interest, where the lattice problem is mapped onto a quantum impurity problem that is numerically solvable. This method provides exact numerical solutions both for very weak and very strong interactions, and in infinite dimensions. It is generally believed that the DMFT method is able to capture the correlation physics of interest in the Hubbard model. Our calculations rely on the DMFT approach for the solution of the one-band Hubbard model near the metal-insulator transition.

## 1.4 Molecular Orbital Theory

The efficient and accurate description of strong correlations in quantum systems, often associated with partially filled and highly localized  $d$ - and  $f$ -shells, has remained a frontier research area. In molecular orbital theory the molecular orbitals are represented as a linear combination of atomic orbitals. The molecular orbital methods, such as second-order Møller-Plesset perturbation theory (MP2) [Møller and Plesset (1934)], configuration interaction (CI) [Shavitt (1998)], coupled cluster theory (CC) [Bartlett and Musial (2007)], can be used to obtain properties of many small molecules without strong correlation effect. In this section we shall present an overview of solutions to correlation problem in quantum many-body systems, including a few popular molecular orbital methods.

### 1.4.1 Hartree-Fock method

Hartree-Fock theory is the basis of the molecular orbital theory, and is conceptually fundamental to much of the electronic structure theory. The Born-Oppenheimer approximation [Born and Oppenheimer (1927)] is inherently assumed in Hartree-Fock method, which separates the electronic from the nuclear degrees of freedom. The Hamiltonian in the Born-Oppenheimer approximation is:

$$H(\mathbf{R}) = -\frac{1}{2} \sum_{i=1}^n \nabla^2(\mathbf{r}_i) - \sum_{i,\alpha} \frac{Z_\alpha}{|\mathbf{r}_i - \mathbf{R}_\alpha|} + \frac{1}{2} \sum_{i,j=1}^n \frac{1}{|\mathbf{r}_i - \mathbf{r}_j|} + \frac{1}{2} \sum_{\alpha,\beta} \frac{Z_\alpha Z_\beta}{|\mathbf{R}_\alpha - \mathbf{R}_\beta|}, \quad (1.2)$$

where  $\mathbf{r}_i$  specifies the position of the electrons and  $\mathbf{R}_\alpha$  the nuclei.  $Z_\alpha$  denotes the atomic number of the nucleus  $\alpha$ . The first term in Eq. 1.2 represents the non-relativistic kinetic energy of the electrons, and the second term denotes the attraction between electrons and nuclei. The Coulomb repulsion between electrons is shown as

the third term. The last term is a constant at any geometry which is the repulsion between nuclei.

Hartree-Fock method approximates the electronic wave function of the many-body system by a single Slater determinant which is anti-symmetric and consequently satisfies the Pauli exclusion principle, and is equivalent to the mean-field approximation that each electron moves independently but subject to the mean-field created by all other electrons. The full Hartree-Fock equations are given by

$$\begin{aligned} \epsilon_i \psi_i(\mathbf{r}) = & \left( -\frac{1}{2} \nabla^2 + V_{\text{ion}}(\mathbf{r}) \right) \psi_i(\mathbf{r}) + \sum_j \int d\mathbf{r}' \frac{|\psi_j(\mathbf{r}')|^2}{|\mathbf{r} - \mathbf{r}'|} \psi_i(\mathbf{r}) \\ & - \sum_j \delta_{\sigma_i \sigma_j} \int d\mathbf{r}' \frac{\psi_j^*(\mathbf{r}') \psi_i(\mathbf{r}')}{|\mathbf{r} - \mathbf{r}'|} \psi_j(\mathbf{r}). \end{aligned} \quad (1.3)$$

The first and second terms on the right hand side of Eq. 1.3 give rise to the kinetic energy contribution and the local electron-ion potential. The third term denotes the average local potential at  $\mathbf{r}$  arising from the charge distribution from the electron in orbital  $\psi_j$ , and is also known as the Hartree-term. The fourth term, or the exchange term, results from the antisymmetry and cancels out the unphysical self-interaction of electrons in the Hartree-term when  $i = j$ .

The Hartree-Fock equations are usually solved numerically in the space spanned by a set of basis functions:

$$\psi_i = \sum_k^M c_{ik} \phi_k, \quad (1.4)$$

transforming the Hartree-Fock equations into the Roothaan equations in restricted open shell Hartree-Fock [Roothaan (1951)] or the Pople-Nesbet-Berthier equations in unrestricted Hartree-Fock [Pople and Nesbet (1954)]. The numerical solutions of the resulting equations can be obtained by iterative diagonalization. Hartree-Fock approximation is a variational method and provides an upper bound to the true ground state energy of the given molecule.



## 1.4.2 Post-Hartree-Fock Methods

Although Hartree-Fock theory is qualitatively correct in many materials and compounds, the quantitative prediction is insufficiently reliable and a set of post-Hartree-Fock methods are developed to improve on the Hartree-Fock method. The electron correlation is taken into account in post-Hartree-Fock methods which provides a more accurate way to include the Coulomb repulsion between electrons.

### Møller-Plesset (MP) Perturbation Theory

Møller-Plesset perturbation theory is a special application of Rayleigh-Schrödinger perturbation theory. In MP perturbation theory, the shifted Fock operator serves as the unperturbed Hamiltonian operator:

$$H_0 \equiv F + \langle \Phi_0 | H - F | \Phi_0 \rangle \quad (1.5)$$

with a small perturbation (correlation potential)

$$V \equiv H - (F + \langle \Phi_0 | H - F | \Phi_0 \rangle), \quad (1.6)$$

where  $\Phi_0$  denotes the normalized Slater determinant corresponding to the lowest eigenvalue of the Fock operator.

One easily sees that the zero-order energy is the Hartree-Fock energy and the first-order MP energy vanishes as stated in the Møller-Plesset theorem [Møller and Plesset (1934)] that “the correlation potential does not contribute in first-order to

the exact electronic energy”. The second order energy can be obtained as

$$E_{\text{MP2}} = \sum_{i,j,a,b} \left\langle \phi_i(1)\phi_j(2) \left| \frac{1}{r_{12}} \right| \phi_a(1)\phi_b(2) \right\rangle \times \frac{2 \langle \phi_a(1)\phi_b(2) | r_{12}^{-1} | \phi_i(1)\phi_j(2) \rangle - \langle \phi_a(1)\phi_b(2) | r_{12}^{-1} | \phi_j(1)\phi_i(2) \rangle}{\varepsilon_i + \varepsilon_j - \varepsilon_a - \varepsilon_b} \quad (1.7)$$

where  $\phi_i$  and  $\phi_j$  denote canonical occupied orbitals,  $\phi_a$  and  $\phi_b$  denote canonical virtual orbitals.  $\varepsilon_i, \varepsilon_j, \varepsilon_a, \varepsilon_b$  are the energies of the corresponding orbitals.

### Configuration Interaction

Configuration Interaction (CI) improves on the Hartree-Fock method by adding electron correlation effects. In order to account for electron correlation, CI approximates the wave function by a linear combination of Slater determinants (or configuration state functions built from spin orbitals):

$$\Psi = \sum_{I=0} c_I \Phi_I^{\text{SO}} = c_0 \Phi_0^{\text{SO}} + c_1 \Phi_1^{\text{SO}} + c_2 \Phi_2^{\text{SO}} \dots \quad (1.8)$$

In Eq. 1.8,  $\Phi_0^{\text{SO}}$  is normally the Hartree-Fock determinant, and  $\Phi_1^{\text{SO}}, \Phi_2^{\text{SO}}$  are the singly, doubly excited determinant, and so forth.

Full configuration interaction (FCI) which includes all possible configuration state functions of the appropriate symmetry, exactly solves the electronic Schrödinger equation within the finite space defined by the basis set. FCI is computationally expensive for large molecules, therefore truncation of the CI-space is important, e.g. the CISD method is limited to single and double excitations. CI solution can be obtained variationally by diagonalization of the resulting Hamiltonian in the truncated CI-space:

$$H_{ij} = \langle \Phi_i^{\text{SO}} | H | \Phi_j^{\text{SO}} \rangle. \quad (1.9)$$

## Coupled Cluster Theory

Introduced by [Coester and Kümmel \(1960\)](#), coupled cluster theory offers very accurate results for weakly correlated small to moderate sized molecules. Coupled cluster method accounts for the electron correlation by constructing multi-electron wave functions using the exponential cluster operator:

$$\Psi = e^T \Phi_0 \quad (1.10)$$

where  $\Phi_0$  is usually constructed from Hartree-Fock molecular orbitals, and the cluster operator  $T$  consists of a set of connected operators:

$$T = T_1 + T_2 + \dots + T_n \quad (1.11)$$

where  $T_1$  introduces all single excitations,  $T_2$  introduces all double excitations and so forth:

$$T_1 \Phi_0 = \sum_{i,a} t_i^a \Phi_i^a, \quad (1.12)$$

$$T_2 \Phi_0 = \sum_{i>j,a>b} t_{ij}^{ab} \Phi_{ij}^{ab}. \quad (1.13)$$

The indices  $i, j$  denote occupied orbitals and  $a, b$  denote unoccupied orbitals. The coefficients  $t_i^a, t_{ij}^{ab}$  are to be determined.

The coupled cluster Schrödinger equation is given by

$$H e^T \Phi_0 = E e^T \Phi_0. \quad (1.14)$$

Applying  $e^{-T}$  to both sides of Eq. 1.14

$$e^{-T} H e^T \Phi_0 = E \Phi_0, \quad (1.15)$$

and projecting Eq. 1.15 onto the Hartree-Fock determinant  $\Phi_0$  and excited determinants  $\Phi^*$ , we have

$$\langle \Phi_0 | e^{-T} H e^T | \Phi_0 \rangle = E, \quad (1.16)$$

$$\langle \Phi^* | e^{-T} H e^T | \Phi_0 \rangle = E \langle \Phi^* | e^{-T} e^T | \Phi_0 \rangle = 0. \quad (1.17)$$

Eq. 1.17 are solved for the wave functions and the energy is evaluated via Eq. 1.16.

Coupled cluster methods truncate the cluster operator  $T$ , e.g. the  $T$  operator in the coupled cluster singles doubles theory (CCSD) is

$$T = T_1 + T_2 \quad (1.18)$$

which only allows single and double excitations. The computational cost increases sharply with the highest level of excitation. For example, the computational scalings of the CCSD and coupled cluster singles doubles theory with perturbative triples [CCSD(T)] are  $n^6$  and  $n^7$  respectively, where  $n$  is the size of the basis.

Other methods are also available, including multi-configurational self-consistent field (MCSCF), quantum Monte Carlo, density matrix renormalization group, just to name a few. A lot of effort is still being devoted to research in this field. However most methods scale poorly with the system size, e.g.  $n^5$  for the hierarchy of second-order Møller-Plesset perturbation theory, severely restricting the systems that can be investigated. The fermionic sign problem prevents direct application of quantum Monte Carlo methods in strongly interacting situations which have been proven very successful for bosonic problems. The density matrix renormalization group formalism, essentially a wave function based approach, has been adapted to problems of relevance in quantum chemistry. While exact, this approach is currently restricted to small systems or to large, but one dimensional molecules [White (1993); Chan and Head-Gordon (2002)]. It is therefore important to have approximate methods that are

more computationally efficient, and numerically solvable. The recent development of the dynamical mean-field theory which expresses the solution of the many fermion problem in terms of a more numerically tractable quantum impurity problem serves as a promising alternative. The exploration of the dynamical mean-field concept in the context of quantum chemistry is the subject of Chap. 5.

# Chapter 2

## Numerical Methods

### 2.1 Overview

This chapter describes the numerical methods we have employed in our study of strongly correlated electron systems. In Sec. 2.2 we introduce the dynamical mean-field theory, which provides an approximate solution to correlated lattice problems, then we proceed to exact diagonalization technique (Sec. 2.3) that solves the quantum impurity problem. Next in Sec. 2.4 we shall discuss the analytic continuation of quantum Monte Carlo data from Matsubara domain to real frequencies. In particular, the Maximum Entropy (MaxEnt) method is the primary tool in our calculations.

### 2.2 Dynamical Mean-Field Theory

Dynamical mean-field theory (DMFT) [[Metzner and Vollhardt \(1989\)](#),[Georges and Kotliar \(1992\)](#),[Georges et al. \(1996\)](#),[Georges \(2004\)](#),[Kotliar et al. \(2006\)](#)] provides an approximate solution to the electronic structure of strongly correlated materials, and has been known to be useful in many problems. In this section, we discuss the single-site [[Georges et al. \(1996\)](#)] and cluster DMFT [[Maier et al. \(2005\)](#)]. The overall procedure in the context of single-site DMFT is briefly sketched in Sec. 2.2.1, and Sec. 2.2.2 presents the extension to its cluster form.

### 2.2.1 Sketch of the procedure

DMFT consists in mapping a many-body lattice problem to a many-body local problem, called an effective quantum impurity model, and a self-consistency condition. In contrast to the lattice problem which is in general intractable with the usual perturbation expansion techniques, impurity models are numerically tractable. The impurity model describes the interaction of the impurity site with a non-interacting electron “bath” through a hybridization function. By representing the partition function  $Z$  of the impurity model as an imaginary-time path integral [Negele and Orland (1988)], one can easily eliminate the bath degrees of freedom following Feynman and Vernon (1963). The effective quantum impurity model, in the example of the Hubbard model, can be described by the following action:

$$Z = \int \mathcal{D}[d^\dagger, d] e^{-S_{\text{eff}}}, \quad (2.1)$$

$$S_{\text{eff}} = - \int_0^\beta d\tau \int_0^\beta d\tau' \sum_\sigma c_\sigma^\dagger(\tau) \mathcal{G}_0^{-1}(\tau - \tau') c_\sigma(\tau') + U \int_0^\beta d\tau n_\uparrow(\tau) n_\downarrow(\tau) \quad (2.2)$$

where  $\mathcal{G}_0$  is a “bath” mean-field function formally obtained by integrating all other lattice sites except for the chosen impurity site, and is related to the hybridization function by the relation:

$$\mathcal{G}_0^{-1}(i\omega_n) = i\omega_n + \mu - \Delta(i\omega_n). \quad (2.3)$$

The hybridization function compactly encodes the environment that the impurity is embedded, which will be determined self-consistently. The self-consistency condition in DMFT is for the impurity Green’s function to reproduce the lattice local Green’s function through the hybridization function.

The mapping to an effective quantum impurity model fundamentally retains a many-body problem which captures the temporal fluctuations due to electron-electron

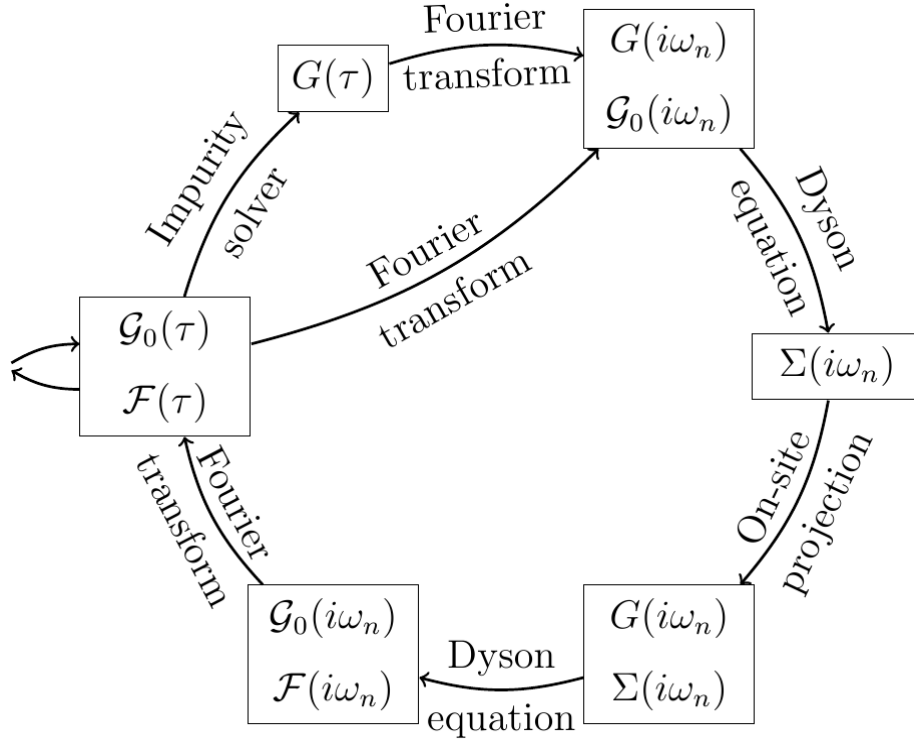


**Figure 2.1:** The iterative self-consistency loop of the dynamical mean-field theory. Reproduced from [Comanac \(2007\)](#).

correlations. The approximation made in DMFT schemes is to assume the lattice self-energy to be a momentum-independent (local in single-site DMFT or within the cluster in cluster DMFT) quantity, which becomes exact in the limit of infinite dimension.

There exist a number of ways to solve the quantum impurity model, such as the exact diagonalization [[Caffarel and Krauth \(1994\)](#); [Capone et al. \(2007\)](#)], numerical renormalization group theory [[Wilson \(1975\)](#); [Sakai and Kuramoto \(1994\)](#)], density matrix renormalization group theory [[Schollwöck \(2005\)](#); [García et al. \(2004\)](#)], non-crossing approximation [[Bickers \(1987\)](#)], and the quantum Monte Carlo technique [[Hirsch and Fye \(1986\)](#); [Rubtsov et al. \(2005\)](#); [Werner et al. \(2006\)](#)].

Fig. 2.1 shows the sketch of the DMFT procedure. One starts with an initial guess for the bare Green's function  $\mathcal{G}_0$  which defines the effective quantum impurity model.



After the quantum impurity model is solved by either of the impurity solvers, the self-energy is obtained from the impurity Green's function:

$$\Sigma_{\text{imp}}(i\omega_n) = \mathcal{G}_0^{-1}(i\omega_n) - G_{\text{imp}}^{-1}(i\omega_n). \quad (2.4)$$

The lattice Green's function can be expressed as:

$$G_{\text{latt}}(k, i\omega_n) = \frac{1}{i\omega_n + \mu - \varepsilon_k - \Sigma(k, i\omega_n)}. \quad (2.5)$$

The on-site Green's function is obtained by integrating  $G_{\text{latt}}(k, i\omega_n)$  over the Brillouin zone:

$$G_{\text{on-site}}(i\omega_n) = \frac{1}{N} \sum_k \frac{1}{i\omega_n + \mu - \varepsilon_k - \Sigma(k, i\omega_n)}. \quad (2.6)$$

One makes the DMFT approximation:

$$\Sigma(k, i\omega_n) \approx \Sigma_{\text{on-site}}(i\omega_n) \approx \Sigma_{\text{imp}}(i\omega_n) \quad (2.7)$$

and computes the on-site Green's function. The bare Green's function  $\mathcal{G}_0$  is updated by a Dyson equation

$$\mathcal{G}_0(i\omega_n) = [G_{\text{on-site}}^{-1}(i\omega_n) + \Sigma_{\text{on-site}}(i\omega_n)]^{-1} \quad (2.8)$$

and the self-consistency loop is completed.

### 2.2.2 Cluster DMFT

In single-site version of dynamical mean-field theory, the approximation is that there is only one impurity site in the quantum impurity model, and the self-energy is approximated to be local or constant in momentum space. In this section, we

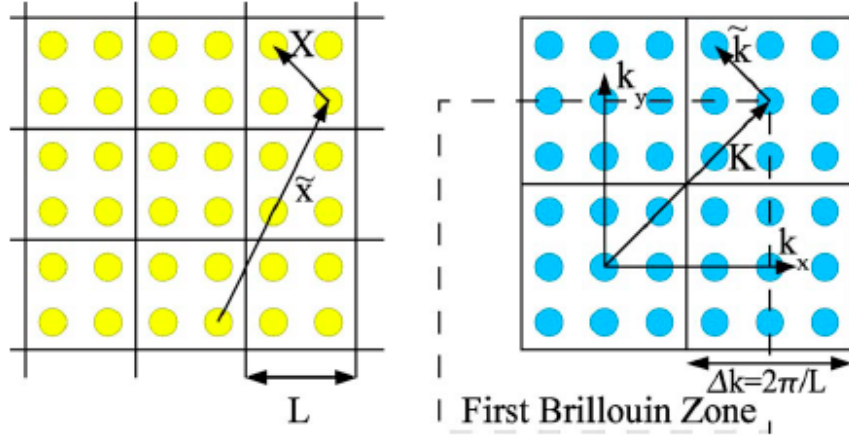


**Figure 2.2:** The coordinates for  $2 \times 2$  clusters in real and reciprocal space. Reproduced from [Maier et al. \(2005\)](#).

briefly review the dynamical mean-field theory in its cluster extension including the Cellular Dynamical Mean-Field Theory (CDMFT) scheme developed by [Lichtenstein and Katsnelson \(2000\)](#) and [Kotliar et al. \(2001\)](#) based on real-space clusters, and Dynamical Cluster Approximation (DCA) scheme developed by [Hettler et al. \(1998\)](#) that describes momentum-space clusters. Cluster DMFT becomes exact when the cluster size diverges, and reduces to single-site DMFT when the cluster size becomes 1.

[Maier et al. \(2005\)](#) reviews quantum cluster theories in much detail. We follow this paper and refer interested readers to the original review article for more detailed information.

### Cellular Dynamical Mean-Field Theory

The CDMFT is based on the embedding of a real space cluster in a self-consistent medium. We divide the lattice of  $N$  sites into a set of clusters of  $N_c$  sites, each with origin  $\tilde{\mathbf{x}}$ . We denote the sites within a cluster as  $\mathbf{X}$ , and the site indices of the original lattice can be described as  $\mathbf{x} = \mathbf{X} + \tilde{\mathbf{x}}$ . Fig. 3.8 shows the coordinates in real and

reciprocal space for  $2 \times 2$  clusters. In reciprocal space we describe the wave vectors in the full Brillouin zone  $\mathbf{k}$  by a vector  $\tilde{\mathbf{k}}$  in the reciprocal space corresponding to the superlattice formed by  $\tilde{\mathbf{x}}$  and a vector  $\mathbf{K}$  in the reciprocal space corresponding to the sites  $\mathbf{X}$  within a cluster:  $\mathbf{k} = \mathbf{K} + \tilde{\mathbf{k}}$ .

To separate out the cluster degrees of freedom, we split the hopping amplitude and the self-energy into intracluster part and intercluster part:

$$\mathbf{t}(\tilde{\mathbf{x}}_i - \tilde{\mathbf{x}}_j) = \mathbf{t}_c \delta_{\tilde{\mathbf{x}}_i, \tilde{\mathbf{x}}_j} + \delta \mathbf{t}(\tilde{\mathbf{x}}_i - \tilde{\mathbf{x}}_j), \quad (2.9)$$

$$\Sigma(\tilde{\mathbf{x}}_i - \tilde{\mathbf{x}}_j, i\omega_n) = \Sigma_c(i\omega_n) \delta_{\tilde{\mathbf{x}}_i, \tilde{\mathbf{x}}_j} + \delta \Sigma(\tilde{\mathbf{x}}_i - \tilde{\mathbf{x}}_j, i\omega_n). \quad (2.10)$$

All the quantities in bold are matrices of size  $N_c \times N_c$  in the cluster sites.  $\mathbf{t}_c$  and  $\delta \mathbf{t}$  are the intracluster and intercluster hopping, while  $\Sigma_c$  and  $\delta \Sigma$  are intracluster and intercluster self-energies.

We then write the Green's function using an expansion in  $\delta \mathbf{t}$  and  $\delta \Sigma$  around the cluster limit:

$$\begin{aligned} \mathbf{G}(\tilde{\mathbf{x}}_i - \tilde{\mathbf{x}}_j, i\omega_n) &= \mathbf{g}(i\omega_n) \delta_{\tilde{\mathbf{x}}_i, \tilde{\mathbf{x}}_j} \\ &+ \mathbf{g}(i\omega_n) \sum_l [\delta \mathbf{t}(\tilde{\mathbf{x}}_i - \tilde{\mathbf{x}}_l) + \delta \Sigma(\tilde{\mathbf{x}}_i - \tilde{\mathbf{x}}_l, i\omega_n)] \mathbf{G}(\tilde{\mathbf{x}}_l - \tilde{\mathbf{x}}_j, i\omega_n), \end{aligned} \quad (2.11)$$

where

$$\mathbf{g}(i\omega_n) = [(i\omega_n + \mu)\mathbf{1} - \mathbf{t}_c - \Sigma_c(i\omega_n)]^{-1} \quad (2.12)$$

is the Green's function of the cluster which is an  $N_c \times N_c$  matrix, and  $\mu$  is the chemical potential. Fourier transforming the intercluster coordinates  $\tilde{\mathbf{x}}$ , Eq. 2.11 simplifies to

$$\mathbf{G}(\tilde{\mathbf{k}}, i\omega_n) = \mathbf{g}(i\omega_n) + \mathbf{g}(i\omega_n) \left[ \delta \mathbf{t}(\tilde{\mathbf{k}}) + \delta \Sigma(\tilde{\mathbf{k}}, i\omega_n) \right] \mathbf{G}(\tilde{\mathbf{k}}, i\omega_n). \quad (2.13)$$

In CDMFT the self-energy is approximated to be local within the cluster, that is

to neglect  $\delta\Sigma$  to get

$$\mathbf{G}(\tilde{\mathbf{k}}, i\omega_n) = \mathbf{g}(i\omega_n) + \mathbf{g}(i\omega_n)\delta\mathbf{t}(\tilde{\mathbf{k}})\mathbf{G}(\tilde{\mathbf{k}}, i\omega_n) = \left[\mathbf{g}^{-1}(i\omega_n) - \delta\mathbf{t}(\tilde{\mathbf{k}})\right]^{-1}. \quad (2.14)$$

The Green's function restricted to the cluster can be obtained by ‘‘coarse-graining’’ or ‘‘ $\tilde{\mathbf{k}}$ -averaging’’  $\mathbf{G}(\tilde{\mathbf{k}}, i\omega_n)$ :

$$\bar{\mathbf{G}}(i\omega_n) = \frac{N_c}{N} \sum_{\tilde{\mathbf{k}}} \mathbf{G}(\tilde{\mathbf{k}}, i\omega_n). \quad (2.15)$$

The excluded-cluster Green's function is obtained by

$$\mathcal{G}_0(i\omega_n) = \left[\bar{\mathbf{G}}^{-1}(i\omega_n) + \Sigma_c(i\omega_n)\right]^{-1}. \quad (2.16)$$

Using these equations, a self-consistent iteration procedure is defined:

1. Start with a guess for the initial cluster self-energy  $\Sigma_c$ , e.g. zero or the second-order perturbation theory approximation.
2. Obtain the ‘‘coarse-grained’’ Green's function  $\bar{\mathbf{G}}(i\omega_n)$  by summing up the lattice Green's function:

$$\bar{\mathbf{G}}(i\omega_n) = \frac{N_c}{N} \sum_{\tilde{\mathbf{k}}} \left[\mathbf{G}_0^{-1}(\tilde{\mathbf{k}}, i\omega_n) - \Sigma_c(i\omega_n)\right]^{-1} \quad (2.17)$$

where the bare Green's function is given by

$$\mathbf{G}_0(i\omega_n) = \left[(i\omega_n + \mu)\mathbf{1} - \mathbf{t}(\tilde{\mathbf{k}})\right]^{-1}. \quad (2.18)$$

3. Solve the effective cluster impurity model defined from the excluded-cluster

Green's function  $\mathcal{G}_0(i\omega_n)$ :

$$\begin{aligned} \mathcal{H}_c = & \sum_{ij,\sigma} (t_{ij} - \mu\delta_{ij}) c_{i\sigma}^\dagger c_{j\sigma} + \sum_{ij,\tilde{\mathbf{k}},\sigma} \lambda_{ij\tilde{\mathbf{k}}} \left[ a_{i\tilde{\mathbf{k}}\sigma}^\dagger a_{j\tilde{\mathbf{k}}\sigma} + \text{H.c.} \right] \\ & + \sum_{ij,\tilde{\mathbf{k}},\sigma} \left[ V_{ij}(\tilde{\mathbf{k}}) c_{i\sigma}^\dagger a_{j\tilde{\mathbf{k}}\sigma} + \text{H.c.} \right] + U \sum_i n_{i\uparrow} n_{i\downarrow} \end{aligned} \quad (2.19)$$

and obtain the cluster Green's function  $\mathbf{G}_c(i\omega_n)$ . Then we calculate a new estimate of the cluster self-energy  $\Sigma_c$  by

$$\Sigma_c(i\omega_n) = \mathcal{G}_0^{-1}(i\omega_n) - \mathbf{G}_c^{-1}(i\omega_n). \quad (2.20)$$

4. Use the new estimate of the cluster self-energy to recalculate the “coarse-grained” Green's function. Iterate until convergence, i.e. the cluster Green's function  $\mathbf{G}_c(i\omega_n)$  to reproduce the “coarse-grained” Green's function  $\bar{\mathbf{G}}(i\omega_n)$  within the desired accuracy.

### Dynamical Cluster Approximation

In dynamical cluster approximation (DCA), the self-energy is approximated to be piecewise constant on different momentum sectors of the Brillouin zone. DCA is introduced to restore translational symmetry within the cluster. We represent the hopping integral  $\mathbf{t}(\tilde{\mathbf{k}})$  by Fourier transforming the dispersion  $\epsilon_{\mathbf{K}+\tilde{\mathbf{k}}}$ :

$$\left[ \mathbf{t}(\tilde{\mathbf{k}}) \right]_{\mathbf{x}_i \mathbf{x}_j} = \frac{1}{N_c} \sum_{\mathbf{K}} e^{i(\mathbf{K}+\tilde{\mathbf{k}}) \cdot (\mathbf{x}_i - \mathbf{x}_j)} \epsilon_{\mathbf{K}+\tilde{\mathbf{k}}}. \quad (2.21)$$

The phase factors  $e^{i\tilde{\mathbf{k}} \cdot (\mathbf{x}_i - \mathbf{x}_j)}$  causes the violation of translational invariance with respect to the cluster sites  $\mathbf{X}$ . We restore the translational symmetry using the

Fourier transform

$$\begin{aligned} \left[ \mathbf{t}_{\text{DCA}}(\tilde{\mathbf{k}}) \right]_{\mathbf{x}_i \mathbf{x}_j} &= \left[ \mathbf{t}(\tilde{\mathbf{k}}) \right]_{\mathbf{x}_i \mathbf{x}_j} e^{-i\tilde{\mathbf{k}} \cdot (\mathbf{x}_i - \mathbf{x}_j)} \\ &= \frac{1}{N_c} \sum_{\mathbf{K}} e^{i\mathbf{K} \cdot (\mathbf{x}_i - \mathbf{x}_j)} \epsilon_{\mathbf{K} + \tilde{\mathbf{k}}}. \end{aligned} \quad (2.22)$$

Splitting  $\mathbf{t}_{\text{DCA}}$  which is fully cyclic in the cluster sites into intracluster and intercluster hopping integrals, we obtain

$$\left[ \mathbf{t}_{c,\text{DCA}} \right]_{\mathbf{x}_i \mathbf{x}_j} = \frac{1}{N_c} \sum_{\mathbf{K}} e^{i\mathbf{K} \cdot (\mathbf{x}_i - \mathbf{x}_j)} \bar{\epsilon}_{\mathbf{K}}, \quad (2.23)$$

$$\left[ \delta \mathbf{t}(\tilde{\mathbf{k}}) \right]_{\mathbf{x}_i \mathbf{x}_j} = \frac{1}{N_c} \sum_{\mathbf{K}} e^{i\mathbf{K} \cdot (\mathbf{x}_i - \mathbf{x}_j)} \delta t(\mathbf{K} + \tilde{\mathbf{k}}) \quad (2.24)$$

with

$$\bar{\epsilon}_{\mathbf{K}} = \frac{N_c}{N} \sum_{\tilde{\mathbf{k}}} \epsilon_{\mathbf{K} + \tilde{\mathbf{k}}}, \quad (2.25)$$

$$\delta t(\mathbf{K} + \tilde{\mathbf{k}}) = \epsilon_{\mathbf{K} + \tilde{\mathbf{k}}} - \bar{\epsilon}_{\mathbf{K}}. \quad (2.26)$$

Since the hopping integrals are translationally invariant within the cluster, the cluster self-energy  $\Sigma_c$  retains translational invariance and becomes diagonal in cluster Fourier ( $\mathbf{K}$ ) space. The lattice Green's function can be written as

$$\begin{aligned} G(\mathbf{K} + \tilde{\mathbf{k}}, i\omega_n) &= \mathbf{g}(\mathbf{K}, i\omega_n) + \mathbf{g}(\mathbf{K}, i\omega_n) \delta t(\mathbf{K} + \tilde{\mathbf{k}}) G(\mathbf{K} + \tilde{\mathbf{k}}, i\omega_n) \\ &= \left[ \mathbf{g}^{-1}(\mathbf{K}, i\omega_n) - \delta t(\mathbf{K} + \tilde{\mathbf{k}}) \right]^{-1}, \end{aligned} \quad (2.27)$$

with  $\mathbf{g}$  the Green's function decoupled from the host,

$$\mathbf{g}(\mathbf{K}, i\omega_n) = [i\omega_n - \bar{\epsilon}_{\mathbf{K}} + \mu - \Sigma_c(\mathbf{K}, i\omega_n)]^{-1}. \quad (2.28)$$

We then construct the “coarse-grained” Green’s function by computing

$$\bar{G}(\mathbf{K}, i\omega_n) = \frac{N_c}{N} \sum_{\tilde{\mathbf{k}}} G(\mathbf{K} + \tilde{\mathbf{k}}, i\omega_n). \quad (2.29)$$

The DCA cluster self-energy  $\Sigma_c(\mathbf{K}, i\omega_n)$  is determined self-consistently analogous to that for cellular DMFT. We use the coarse-graining equation

$$\bar{G}(\mathbf{K}, i\omega_n) = \frac{N_c}{N} \sum_{\tilde{\mathbf{k}}} \left[ G_0^{-1}(\mathbf{K} + \tilde{\mathbf{k}}) - \Sigma_c(\mathbf{K}, i\omega_n) \right]^{-1} \quad (2.30)$$

with the bare Green’s function

$$G_0(\mathbf{K} + \tilde{\mathbf{k}}, i\omega_n) = [i\omega_n - \epsilon_{\mathbf{K}+\tilde{\mathbf{k}}} + \mu]^{-1}. \quad (2.31)$$

We represent the DCA effective cluster model in cluster  $\mathbf{K}$  space as

$$\begin{aligned} \mathcal{H}_c = & \sum_{\mathbf{K}, \sigma} (\bar{\epsilon}_{\mathbf{K}} - \mu) c_{\mathbf{K}\sigma}^\dagger c_{\mathbf{K}\sigma} + \sum_{\mathbf{k}, \sigma} \lambda_{\mathbf{k}} a_{\mathbf{k}\sigma}^\dagger a_{\mathbf{k}\sigma} \\ & + \sum_{\mathbf{K}, \tilde{\mathbf{k}}, \sigma} \left[ V_{\mathbf{K}}(\tilde{\mathbf{k}}) c_{\mathbf{K}\sigma}^\dagger a_{\mathbf{K}+\tilde{\mathbf{k}}\sigma} + \text{H.c.} \right] + \sum_{\mathbf{K}, \mathbf{K}', \mathbf{Q}} \sum_{\sigma\sigma'} \frac{U}{2N_c} c_{\mathbf{K}+\mathbf{Q}\sigma}^\dagger c_{\mathbf{K}'-\mathbf{Q}\sigma'}^\dagger c_{\mathbf{K}'\sigma'} c_{\mathbf{K}\sigma}. \end{aligned} \quad (2.32)$$

## 2.3 Exact Diagonalization

There are various methods to solve the quantum impurity problem, e.g. [Gull et al. \(2011a\)](#) reviews the recently developed continuous-time quantum Monte Carlo algorithms for quantum impurity models. In this section, we briefly discuss the exact diagonalization (ED) approach introduced by [Caffarel and Krauth \(1994\)](#). Besides the cheap computational cost, one advantage of ED solver is that the spectrum can be directly obtained on real frequency axis.

We consider the Hamiltonian of the effective quantum impurity model

$$H_{\text{QI}} = \sum_{\mu\nu\sigma} E_{\mu\nu} c_{\mu\sigma}^\dagger c_{\nu\sigma} + U \sum_{\mu} n_{\mu\uparrow} n_{\mu\downarrow} + \sum_{k\sigma} \varepsilon_k a_{k\sigma}^\dagger a_{k\sigma} + \sum_{k\mu\sigma} (V_{k\mu} a_{k\sigma}^\dagger c_{\mu\sigma} + \text{H.c.}), \quad (2.33)$$

where the indices  $\mu, \nu = 1, \dots, N_c$  label the cluster sites,  $E_{\mu\nu}$  contains the hopping matrix elements inside the cluster and the chemical potential term. The auxiliary fermionic degrees of freedom  $a_{k\sigma}$  describe the bath. The cluster is coupled to the bath via the hybridization  $V_{k\mu}$ .

The non-interacting Green's function  $\mathcal{G}_0$  which is given by the  $U = 0$  Green's function is obtained by integrating out the bath degrees of freedom  $a_{k\sigma}$

$$(\mathcal{G}_0)_{\mu\nu}^{-1}(i\omega_n) = i\omega_n \delta_{\mu\nu} - E_{\mu\nu} - \sum_k \frac{V_{k\mu}^* V_{k\nu}}{i\omega_n - \varepsilon_k}, \quad (2.34)$$

where  $\delta_{\mu\nu}$  denotes the Kronecker delta.

The strict self-consistency can only be obtained with a continuous bath of states. The idea of the exact diagonalization solver is to discretize the problem by parameterizing the hybridization function in terms of a finite number of poles,

$$\sum_{k=1}^{n_s} \frac{V_{k\mu}^* V_{k\nu}}{i\omega_n - \varepsilon_k}, \quad (2.35)$$

here the sum runs over a discrete set of  $k = 1, \dots, n_s$  (in practice total orbitals  $\sim 5-12$ ).

In practice we approximate  $\mathcal{G}_0(i\omega_n)$  by a function  $\mathcal{G}_0^{\text{ED}}(i\omega_n)$  with a finite number  $n_s$  bath states, which can be cast into a minimization problem in the parameters  $\varepsilon_k$  and  $V_{k\mu}$ . Different cost functions were reported in the literature, for example:

$$\chi^2 = \frac{1}{n_{\text{max}} + 1} \sum_{n=0}^{n_{\text{max}}} \sum_{\mu\nu} \Delta \quad (2.36)$$



with

$$\Delta^1 = \left| (\mathcal{G}_0)^{-1}(i\omega_n) - (\mathcal{G}_0^{\text{ED}})^{-1}(i\omega_n) \right|^2; \quad (2.37)$$

$$\Delta^2 = \left| (\mathcal{G}_0)_{\mu\nu}(i\omega_n) - (\mathcal{G}_0^{\text{ED}})_{\mu\nu}(i\omega_n) \right|^2; \quad (2.38)$$

$$\Delta^3 = \left| (\mathcal{G}_0)_{\mu\nu}(i\omega_n) - (\mathcal{G}_0^{\text{ED}})_{\mu\nu}(i\omega_n) \right| / \omega_n, \quad (2.39)$$

where  $n_{\text{max}}$  is a very large upper cutoff. Practically it makes little difference by fitting  $\mathcal{G}_0$  and  $\mathcal{G}_0^{\text{ED}}$ , their inverse or by putting in  $\omega$ -dependent factors. In our work, we choose to fit the sum of the square misfit of  $\mathcal{G}_0$  (Eq. 2.38). Different algorithms can carry out this task, and we performed the minimization based on the conjugate gradient code provided by [Georges et al. \(1996\)](#).

The Hamiltonian with small  $n_s$  corresponding to Eq. 2.33 can be diagonalized exactly for a complete set of eigenvectors and eigenvalues, from which the Green's function  $\mathbf{G}(i\omega_n)$  can be computed.

The new mean-field function  $\mathcal{G}_0$  is obtained by the self-consistency equations, which in turn determines a new set of  $\varepsilon_k$  and  $V_{k\mu}$ . The process is then iterated until convergence.

## 2.4 Analytic Continuation

Recent improvements on continuous-time quantum Monte Carlo methods have made it possible to obtain highly accurate solutions of the equations of dynamical mean-field theory at previously unreachable temperatures and coupling strengths. These methods are most conveniently formulated on imaginary time axis (or Matsubara frequencies). While the static expectation values, such as occupancy, are easily accessible in these methods, it remains challenging to obtain dynamical information,

such as spectral function and other physically relevant spectra. The analytic continuation of imaginary time data [Silver et al. (1990), Gubernatis et al. (1991), Jarrell and Gubernatis (1996)] is numerically ill-conditioned with a number of difficulties. The Exact Diagonalization (ED) method discussed in Sec. 2.3 provides direct access to real frequency information, but also involves other uncertainty as the number of states that contribute to a given response function is too small. In this section, we shall focus on the Maximum Entropy analytic continuation technique [Jarrell and Gubernatis (1996)] of  $F(i\omega_n)$ , the response function on Matsubara frequency axis.

In practice QMC methods provide measurements of a function defined on imaginary time  $\tau$  (or equivalently Matsubara frequencies  $i\omega_n$ ). For fermionic quantities (e.g. electron Green's function  $G$  and “normalized” self-energy  $\tilde{\Sigma}$ ),  $F$  is related to a spectral function  $A(\omega)$  by

$$F(i\omega_n) = \int_{-\infty}^{\infty} \frac{1}{i\omega_n - \omega} A(\omega) d\omega \quad (2.40)$$

with  $A$  positive definite and normalizable:

$$A(\omega) = -\frac{1}{\pi} \text{Im}F(\omega). \quad (2.41)$$

Separating the real and imaginary parts of  $F(i\omega_n)$ , we have

$$\text{Re}F(i\omega_n) = - \int_{-\infty}^{\infty} \frac{\omega}{\omega^2 + \omega_n^2} A(\omega) d\omega, \quad (2.42)$$

$$\text{Im}F(i\omega_n) = - \int_{-\infty}^{\infty} \frac{\omega_n}{\omega^2 + \omega_n^2} A(\omega) d\omega. \quad (2.43)$$

Analytic continuation is the inversion of Eq. 2.40 to obtain  $A$  given  $F$ . Unfortunately it is ill-posed because it requires inverting the operator  $1/(i\omega_n - \omega)$ , which may have many relatively small eigenvalues, so the inverse has many large eigenvalues leading to enormous amplification of numerical or measurement errors on inversion.

While various attempts have been made to solve the problem, Maximum Entropy (MaxEnt) method is one of the most widely used techniques, which is based on defining  $A$  as the function that maximizes the free energy function  $Q[A]$  defined as:

$$Q[A] = \alpha S[A] - L[A] \quad (2.44)$$

where  $S$  is the entropy-like term and  $L$  energy-like.  $\alpha$  is the temperature-like term that controls the competition between  $S$  and  $L$ . The energy-like term  $L$  measures the mean square misfit between the data computed from the proposed spectrum  $A(\omega)$  via Eq. 2.40 and the QMC data  $\bar{F}$ :

$$L = \frac{1}{2} \chi^2 = \frac{1}{2} (\bar{\mathbf{F}} - \mathbf{K}\mathbf{A})^T \mathbf{C}^{-1} (\bar{\mathbf{F}} - \mathbf{K}\mathbf{A}) \quad (2.45)$$

where  $\mathbf{C}$  is the covariance function which contains information of the statistical uncertainties in the computation:

$$C_{ij} = \langle \delta F_i \delta F_j \rangle. \quad (2.46)$$

The entropy-like term  $S$  is defined relative to a model function that brings in regularization:

$$S = \int d\omega \left[ A(\omega) - m(\omega) - A(\omega) \ln \frac{A(\omega)}{m(\omega)} \right]. \quad (2.47)$$

To perform the extremization, the algorithm discussed in [Jarrell and Gubernatis \(1996\)](#) can be implemented. In practice we generate the spectra using a broad range of  $\alpha$  and select  $\alpha$  by constructing a plot of the entropy term  $-S$  and the misfit term  $\chi^2$  on a log scale, which has a characteristic  $L$ -shape. The corner of the  $L$ -curve [[Lawson and Hanson \(1995\)](#); [Rabani et al. \(2002\)](#)], is the one that corresponds to the value of  $\alpha$  that best compromises the competition between the two terms.

Eq. 2.40 can be directly applied to analytic continue the electron Green's function

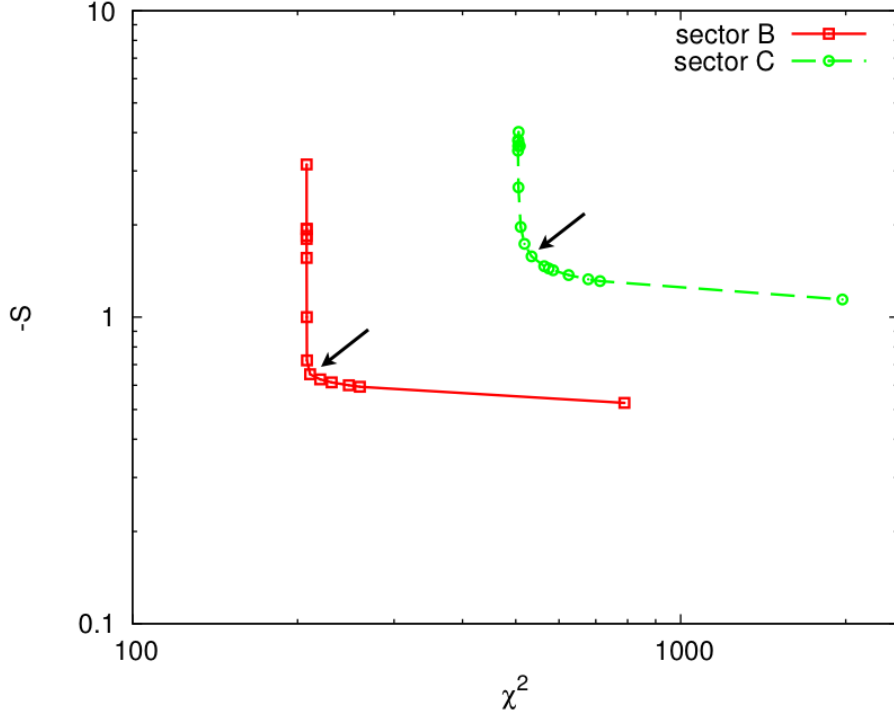


**Figure 2.3:** The constructed  $L$ -curve to select  $\alpha$  that best compromises the competition between  $S$  and  $\chi^2$ . The calculations are done for the sector  $B$  and  $C$  self-energies obtained from the 8-site DCA approximation to the half-filled two-dimensional Hubbard model for  $U = 7t$ ,  $\beta t = 20$  and  $t' = 0$ .

$G(i\omega_n)$ . The self-energy  $\Sigma(i\omega_n)$  is related to the full Green's function  $G(i\omega_n)$  and the bare Green's function  $G_0(i\omega_n)$  by

$$\Sigma(i\omega_n) = G_0^{-1}(i\omega_n) - G^{-1}(i\omega_n). \quad (2.48)$$

One can obtain the self-energy on real frequency axis by continuing  $G_0(i\omega_n)$  and  $G(i\omega_n)$  and taking the difference of their inverse. However, due to the error introduced by analytic continuation of  $G$  and  $G_0$ , the quantity  $G_0^{-1}(\omega) - G^{-1}(\omega)$  may have an unphysical sign change instead of negative definite. Wang et al. (2009) proposed an improvement on Maximum Entropy method to continue  $\Sigma(i\omega_n)$  directly. The spectral function can then be obtained by integrating.

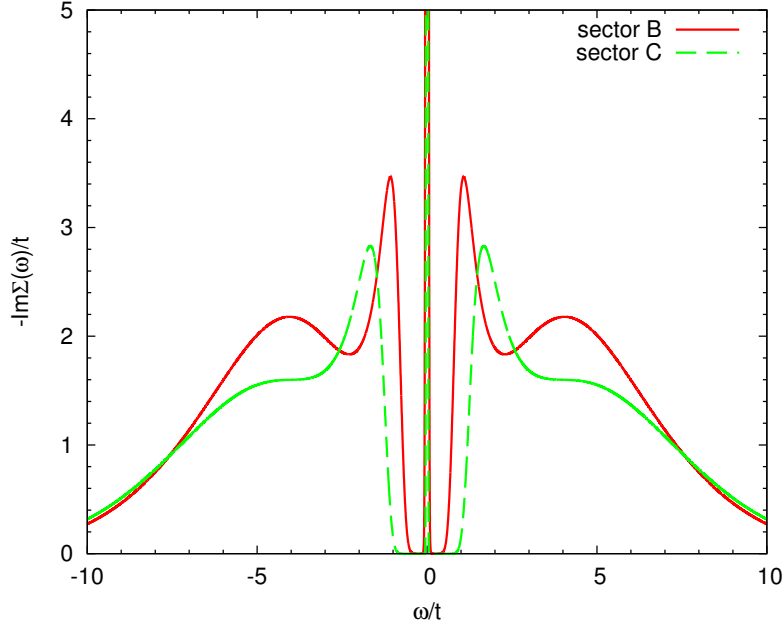


**Figure 2.4:** Imaginary part of the self-energies in sector  $B$  (red trace) and sector  $C$  (green trace) for  $U = 7t, \beta t = 20$  and  $t' = 0$  in the 8-site DCA approximation to the half-filled two-dimensional Hubbard model with the values of  $\alpha$  selected from the  $L$ -curve.

In the Hubbard model, the asymptotic behavior of the self-energy is [Potthoff et al. (1997)]:

$$\Sigma_{\sigma}(i\omega_n) = U \langle n_{-\sigma} \rangle + U^2 \langle n_{-\sigma} \rangle (1 - \langle n_{-\sigma} \rangle) \frac{1}{i\omega_n} + \mathcal{O}\left(\frac{1}{(i\omega_n)^2}\right). \quad (2.49)$$

We define the “normalized” self-energy:

$$\tilde{\Sigma}_{\sigma}(i\omega_n) = \frac{\Sigma_{\sigma}(i\omega_n) - U \langle n_{-\sigma} \rangle}{U^2 \langle n_{-\sigma} \rangle (1 - \langle n_{-\sigma} \rangle)}. \quad (2.50)$$

Apparently  $\tilde{\Sigma}$  is just like the Green’s function and can be easily continued by the Maximum Entropy method. More details can be found in Wang et al. (2009), such as the estimation of the covariance function  $\langle \delta\Sigma(i\omega_n) \delta\Sigma^*(i\omega_m) \rangle$ .

For illustration, we employ MaxEnt to analytic continue the self-energies obtained

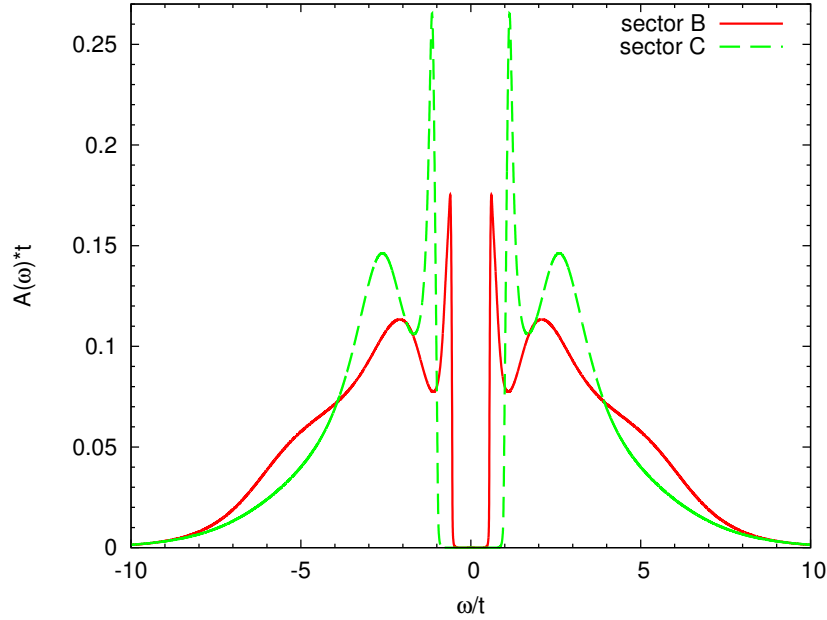


**Figure 2.5:** The spectral function in sector  $B$  (red trace) and sector  $C$  (green trace) for  $U = 7t$ ,  $\beta t = 20$  and  $t' = 0$  in the 8-site DCA approximation to the half-filled two-dimensional Hubbard model.

from the 8-site DCA approximation to the half-filled two-dimensional Hubbard model for  $U = 7t$ ,  $t' = 0$  and the inverse temperature  $\beta t = 20$ . The Brillouin zone partitioning is shown in Fig. 4.1. Fig. 2.3 presents the constructed  $L$ -curve for the self-energies in sector  $B$  and  $C$ . The self-energies corresponding to the corner of the  $L$ -curve (indicated by the arrow) are plotted in Fig. 2.4. We see that at half-filling the low frequency self-energies in the two sectors containing the Fermi surface are dominated by a pole located at  $\omega = 0$ . The real part of the self-energy can be evaluated from Kramers-Kronig relation:

$$\text{Re}\Sigma(\omega) = \frac{1}{\pi} \int_{-\infty}^{\infty} \frac{\text{Im}\Sigma(\omega')}{\omega' - \omega} d\omega', \quad (2.51)$$

and the sector-averaged electron spectral function is obtained by

$$A_K(\omega) = -\frac{N_c}{\pi} \int_K \frac{d^2k}{(2\pi)^2} \text{Im} \left[ \frac{1}{\omega + \mu - \epsilon_k - \Sigma_K(\omega)} \right] \quad (2.52)$$

where  $N_c = 8$  and  $\mu$  is the chemical potential. The spectral functions are shown in Fig. 2.5 which exhibit a wide energy gap in both sectors, indicating that the model is in the insulating state. More results are presented in Chap. 4.

We can apply similar procedure to analytic continue the two-particle response functions from Matsubara frequencies to real frequencies, but use a different kernel from Eq. 2.40 for those bosonic quantities (e.g. Raman intensity):

$$\chi(i\omega_n) = \int_{-\infty}^{\infty} \frac{w}{i\omega_n - \omega} A(\omega) d\omega \quad (2.53)$$

where  $A(\omega) = -\frac{1}{\pi} \text{Im}\chi(\omega)/\omega$ .  $\text{Im}\chi(\omega)$  is an odd function and  $A(\omega)$  is even and positive definite. The normalization of  $A(\omega)$  is given by  $-\chi(0)$ .

As discussed in Chap. 3, the two-particle response functions with vertex correction are measured on Matsubara frequency axis, therefore reliable analytic continuation is desired which provides insight into the physics of interest.

# Chapter 3

## Two-Particle Response Functions

### 3.1 Overview

This chapter presents a numerical study of the two-particle response functions in high- $T_c$  cuprate superconductors. Sec. 3.2 introduces the background. In Sec. 3.3 we present the model and the general formalism to calculate the two-particle response functions with vertex corrections. Sec. 3.4 presents our numerical results for the Raman scattering intensity. In Sec. 3.5 we present results for the optical conductivity. Finally we summarize in Sec. 3.6. Part of this chapter follows [Lin et al. \(2009\)](#).

### 3.2 Introduction

Understanding the motion of electrons in solids is one of the fundamental questions in condensed matter physics. Different spectroscopic techniques address this question from different points of view. Angle-resolved photoemission provides information about the propagation of one hole created in a solid, while optical conductivity and electronic Raman scattering measurements are two-particle spectroscopies involving creating particle-hole pairs in the material. Performing these experiments on layered copper-oxide materials such as  $\text{La}_{2-x}\text{Sr}_x\text{CuO}_4$  has revealed strikingly anomalous behavior which has challenged theoretical understanding for a quarter century since the



discovery of high-temperature superconductivity in these compounds. Optical spectroscopy [Basov and Timusk (2005)] is typically interpreted in terms of an optical mass which is strongly suppressed relative to density functional band theory predictions and has a strong doping dependence [Comanac et al. (2008)] indicating that the materials are strongly correlated doped Mott insulators, whereas angle-resolved photoemission experiments reveal a mass enhancement (difference of measured velocity from band values) which is not large and not strongly dependent on carrier concentration (suggesting weaker correlations), and also reveal a “pseudogap” (suppression of low energy density of states over some but not all of the Brillouin zone) which is not visible as a suppression of the density of states in the optical spectra. Finally, the electronic contribution to the Raman intensity, which in typical “weakly correlated” materials is related to the product of frequency and the conductivity, in high- $T_c$  materials is characterized by strong difference between scattering channels and by the appearance of a “two-magnon” component unrelated to the conductivity. These behaviors are believed to reflect fundamental aspects of the physics of strong electronic correlations in two dimensions and to be associated with the mechanism for high-temperature superconductivity but have not been understood in a unified way from a single model.

These properties have not been understood in a unified way in terms of controlled calculations from a well defined model. A key difficulty has been that while our ability to calculate photoemission spectra has been transformed by the development of dynamical mean-field theory, first in its single-site [Georges et al. (1996)], and then in “cluster” forms [Maier et al. (2005)], our understanding of physically relevant response functions has lagged because these computations require a “vertex correction” which has not been theoretically accessible except in special cases such as one dimensional models with linear dispersion, or the BCS theory of superconductivity [Schreiffer (1999)].

### 3.3 Model and Methods

We study the one-band Hubbard model, which is defined by the Hamiltonian

$$H_{\text{Hub}} = \sum_{k\sigma} \varepsilon_k c_{k\sigma}^\dagger c_{k\sigma} + U \sum_i n_{i\uparrow} n_{i\downarrow} - \mu \sum_{i\sigma} n_{i\sigma} \quad (3.1)$$

and whose two dimensional version has been argued [[Anderson \(1987\)](#)] to capture the essential physics of high-temperature copper-oxide superconductors. For definiteness we take  $\varepsilon_k = -2t(\cos k_x + \cos k_y) - 4t' \cos k_x \cos k_y$  with  $t' = -0.15t$  and  $U = 7t$ . For comparison to data,  $t \approx 0.35$  eV is generally accepted for high- $T_c$  superconductors [[Andersen et al. \(1995\)](#)].

In the rest of this section we demonstrate a new method for computing physically relevant response functions within cluster dynamical mean-field theory. The method builds on recent theoretical [[Lin et al. \(2009\)](#)] and computational [[Gull et al. \(2008a, 2011a,b\)](#)] developments of the cluster dynamical mean-field formalism. We use the formalism to calculate the  $B_{1g}$  and  $B_{2g}$  (non-resonant) electronic Raman scattering intensities and the optical conductivity for the two dimensional Hubbard model defined in Eq. 3.1. While this model has been proposed as the appropriate theoretical description of the physics of high-temperature copper-oxide superconductors on scales less than the bandwidth [[Anderson \(1987\)](#)], it has not been known whether the essential features of the data, as described in Sec. 3.2, are in fact contained in the model. We aim to investigate this issue, and generalize the formalism to provide the theory for a wide variety of other measurements. However, we do note that at this stage of the development of the field, the method requires supercomputer resources.

To introduce the method, we observe that from a formal point of view, most of the physically relevant electronic responses (for example the electrical current) may be determined from a knowledge of the electron Green's function  $\mathbf{G}$ , computed in the presence of an external perturbation or “probe” (such as applied electromag-

netic radiation). Denoting the probing field by  $P$  and the response by  $R$  we have, schematically,

$$R = \text{Tr} [\mathbf{R}\mathbf{G}(\{P\})] \quad (3.2)$$

with  $\mathbf{R}$  denoting the operator corresponding to the response which is to be measured (for example, the current operator) and  $\{P\}$  indicating that the Green's function is to be computed in the presence of the probing field  $P$ .

$\mathbf{G}$  is defined in terms of a reference band structure described by a free-fermion Hamiltonian  $\mathbf{H}_0$  and a “self-energy”  $\Sigma$  which parameterizes the difference between the actual electron propagation and the propagation implied by  $\mathbf{H}_0$ ; thus  $\mathbf{G}(\{P\}) = [i\partial_t - \mathbf{H}_0(\{P\}) - \Sigma(\{P\})]^{-1}$ . One is generally interested in situations in which  $R$  vanishes if  $P = 0$  but  $P$  is weak. Expanding to linear order in  $P$ , we have  $R = \chi_{RP}P + \mathcal{O}(P^2)$  with response function

$$\chi_{RP} = \text{Tr} \left[ \frac{\delta \mathbf{R}}{\delta P} \mathbf{G} \right] + \text{Tr} \left[ \mathbf{R} \mathbf{G} \frac{\delta \mathbf{H}_0}{\delta P} \mathbf{G} \right] + \text{Tr} \left[ \mathbf{R} \mathbf{G} \frac{\delta \Sigma}{\delta P} \mathbf{G} \right] \quad (3.3)$$

where the absence of an explicitly denoted ( $\{P\}$ ) indicates the quantity is computed at  $P = 0$ .

The terms in Eq. 3.3 may be represented diagrammatically as shown in Fig. 3.1. The first two terms, (a) and (b) in the figure, require knowledge of the full electron propagation at  $P = 0$  as well as the way the perturbation enters the operator corresponding to the response (denoted by the filled square) and the Hamiltonian itself (denoted by the filled circle). The third term (diagram (c)) requires knowledge of the dependence of the self-energy on the perturbation and is referred to as the “vertex correction” because it may be thought of as a change to the bare vertex  $\delta \mathbf{H}_0 / \delta P$  represented as a filled circle in Fig. 3.1(b).

A reasonable approximation to the electron propagator  $\mathbf{G}$  needed for diagrams (3.1a) and (3.1b) can now be obtained from cluster dynamical mean-field theory

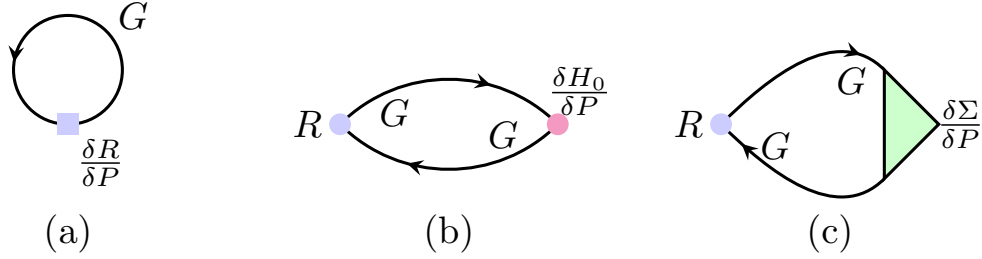


**Figure 3.1:** Feynman Diagrams corresponding to computation of response function as in Eq. 3.3. Heavy line with arrow: electron propagator  $\mathbf{G}$ . Square: dependence of response on perturbation (“diamagnetic term” in calculation of optical conductivity). Circle: response function (taken to be the same as the operator to which the perturbation couples). Shaded area in diagram (c) represents the vertex correction.

[Georges et al. (1996); Maier et al. (2005)]. This method, in combination with algorithmic improvements including continuous-time quantum Monte Carlo methods [Gull et al. (2011a)] and submatrix updates [Gull et al. (2011b)], enables calculations in wide parameter regimes previously inaccessible either to perturbation theory or to other numerical methods. The method is based on approximating the electron self-energy  $\Sigma_\sigma(X, \tau)$ , which depends on spatial coordinates (here denoted in a general way by  $X$ ) and temporal coordinates (here denoted in a general way by  $\tau$ ) as (see Maier et al. (2005) and Fuhrmann et al. (2007) for details)

$$\Sigma_\sigma(X, \tau) = \sum_{a=1}^N \phi_a(X) \Sigma_{a\sigma}(\tau). \quad (3.4)$$

The functions  $\phi_a(X)$  which carry the spatial dependence must be such that in the limit  $N \rightarrow \infty$  the full spatial dependence is recovered. Different choices of  $\phi_a$  correspond to different “flavors” of dynamical mean-field approximation [Hettler et al. (1998, 2000); Kotliar et al. (2001); Maier et al. (2005); Fuhrmann et al. (2007)].

We use the “DCA” version of dynamical mean-field theory [Hettler et al. (1998, 2000)] in which one tiles the Brillouin zone into equal area tiles (see Fig. 3.2 for example) and chooses the functions  $\phi_a(k)$  such that  $\phi_a(k) = 1$  if  $k$  is contained in tile

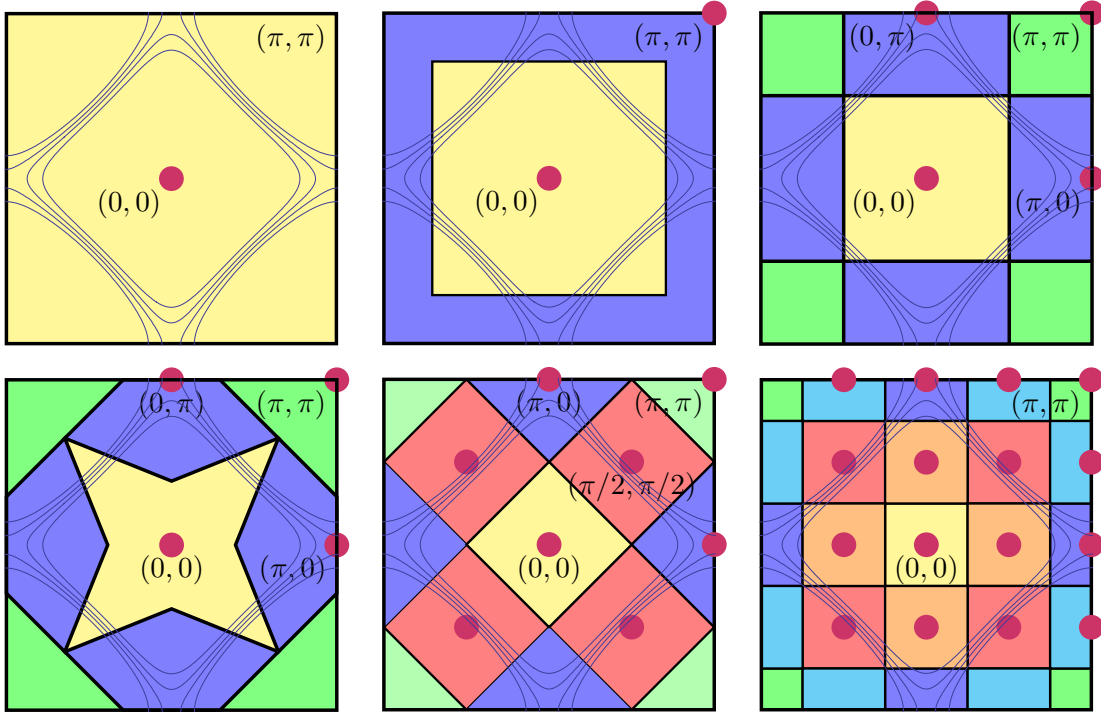


**Figure 3.2:** Brillouin-zone partitioning associated with the single-site, two-site, four-site, eight-site and sixteen-site clusters. Reproduced from [Gull et al. \(2010\)](#).

$a$  and  $\phi_a(k) = 0$  otherwise. This approach preserves translational invariance.

The functions  $\Sigma_{a\sigma}(\tau)$  are defined as the self-energies of an auxiliary  $N$ -site quantum impurity model ( $0 + 1$  dimensional quantum field theory with  $a = 1 \dots N$  internal indices for the sites as well as the additional indices  $\sigma$  required for spin degrees of freedom). It is convenient to write the action of the theory in the Grassmann variable representation as

$$S_{\text{eff}} = - \int_0^\beta d\tau \int_0^\beta d\tau' \sum_{a,\sigma} c_{a\sigma}^\dagger(\tau) (\mathcal{G}_0^{-1})_{a\sigma}(\tau, \tau') c_{a\sigma}(\tau') + S_{\text{int}} \quad (3.5)$$

involving an interaction term  $S_{\text{int}}$  determined by the interactions of the starting model and a Weiss-like effective field  $\mathcal{G}_0^{-1}$ , a matrix in the space of “sites”  $a$  and spin  $\sigma$ .  $\mathcal{G}_0^{-1}$  is determined by a self-consistency condition relating the Green’s function

$\mathbf{G}^{\text{QI}} = (\mathcal{G}_0^{-1} - \Sigma)^{-1}$  of the quantum impurity model to an appropriate average over momentum degrees of freedom of the full Green's function (evaluated with approximate self-energy):

$$\mathbf{G}_{a\sigma}^{\text{QI}} \equiv [(\mathcal{G}_0^{-1})_{a\sigma} - \Sigma_{a\sigma}]^{-1} = \int \frac{d^2k}{(2\pi)^2/N_c} \left[ \phi_a(k) \left( i\partial_t + \mu - \varepsilon_k - \sum_{b=1}^N \phi_b(k) \Sigma_{b\sigma} \right)^{-1} \right]. \quad (3.6)$$

Given  $\mathcal{G}_0^{-1}$  and the interactions, the Green's function  $\mathbf{G}^{\text{QI}}$  can be determined (for example, via a quantum Monte Carlo calculation), the self-energy extracted, and Eq. 3.6 solved (the solution is normally reached by iteration from an initial guess).

The description to this point is standard [Georges et al. (1996); Maier et al. (2005)]. To extend the formalism to the vertex functions needed to evaluate physical response functions we observe that Eq. 3.6 holds also in the presence of a perturbing field  $P$  but with  $\varepsilon_k$ ,  $\mathcal{G}_0^{-1}$  and  $\Sigma$  all depending on  $P$ . Linearizing these quantities and Eqs. 3.5 and 3.6 in the perturbing field then leads to equations which may be solved for the first order corrections to  $\mathcal{G}_0^{-1}$  and  $\Sigma$ . We denote the first order corrections to  $\mathbf{G}$ ,  $\mathcal{G}_0^{-1}$  and  $\Sigma$  by  $\mathbf{G}^1$ ,  $(\mathcal{G}_0^{-1})^1$  and  $\Sigma^1$  respectively:

$$\mathbf{G} = \mathbf{G}^{\text{eq}} + \mathbf{G}^1 P + \mathcal{O}(P^2); \quad (3.7)$$

$$\mathcal{G}_0^{-1} = (\mathcal{G}_0^{-1})^{\text{eq}} + (\mathcal{G}_0^{-1})^1 P + \mathcal{O}(P^2); \quad (3.8)$$

$$\Sigma = \Sigma^{\text{eq}} + \Sigma^1 P + \mathcal{O}(P^2). \quad (3.9)$$

To construct a closed set of equations in  $\mathbf{G}^1$ ,  $(\mathcal{G}_0^{-1})^1$  and  $\Sigma^1$ , we start from the basic DMFT self-consistency equation in DCA:

$$G_{a\sigma}^{\text{QI}}(\omega, \omega') = \int^a \frac{d^2k}{(2\pi)^2/N_c} [(i\omega + \mu - \varepsilon_k) \delta_{\omega, \omega'} - M_k P(\omega, \omega') - \Sigma_{a\sigma}(\omega, \omega')]^{-1} \quad (3.10)$$

where  $\int^a$  denotes an integral over momenta lying in sector  $a$  in the impurity model

and lattice Green's functions are computed in the presence of the time dependent perturbation  $P$ ,  $M_k$  is the matrix element to which the perturbation couples. If the perturbation is monochromatic with frequency  $\Omega$  [ $P(\omega, \omega') = P\delta_{\omega-\Omega, \omega'}$ ] and small we may linearize Eq. 3.10 obtaining

$$G_{a\sigma}^1(\omega + \Omega, \omega) = \Lambda_{a\sigma}^\Omega(\omega)\Sigma_{a\sigma}^1(\omega + \Omega, \omega) + P_{a\sigma}^\Omega(\omega) \quad (3.11)$$

with

$$\Lambda_{a\sigma}^\Omega(\omega) = \int \frac{d^2k}{(2\pi)^2/N_c} G_{\text{lattice}}^{\text{eq}}(k, \omega + \Omega) G_{\text{lattice}}^{\text{eq}}(k, \omega), \quad (3.12)$$

$$P_{a\sigma}^\Omega(\omega) = \int \frac{d^2k}{(2\pi)^2/N_c} G_{\text{lattice}}^{\text{eq}}(k, \omega + \Omega) M_k G_{\text{lattice}}^{\text{eq}}(k, \omega). \quad (3.13)$$

The source term  $\mathbf{P}$  depends on the symmetry of the perturbation, and  $G_{\text{lattice}}^{\text{eq}}$  is the lattice Green's function evaluated at equilibrium:

$$G_{\text{lattice}}^{\text{eq}}(k, \omega) = [i\omega + \mu - \varepsilon_k - \Sigma_{a\sigma}^{\text{eq}}(\omega)]^{-1}. \quad (3.14)$$

The self-energy  $\Sigma^{\text{eq}}$  is obtained from the ‘‘DCA’’ solution of the equilibrium quantum impurity model.

On the other hand by linearizing the relation

$$G_{a\sigma}^{\text{QI}}(\omega, \omega') \equiv [(\mathcal{G}_0^{-1})_{a\sigma}(\omega, \omega') - \Sigma_{a\sigma}(\omega, \omega')]^{-1}, \quad (3.15)$$

we obtain:

$$G_{a\sigma}^1(\omega, \omega') = -G_{a\sigma}^{\text{QI,eq}}(\omega) \left[ (\mathcal{G}_0^{-1})_{a\sigma}^1(\omega, \omega') - \Sigma_{a\sigma}^1(\omega, \omega') \right] G_{a\sigma}^{\text{QI,eq}}(\omega'). \quad (3.16)$$

Rearranging Eq. 3.16 leads to

$$\Sigma_{a\sigma}^1(\omega, \omega') = (\mathcal{G}_0^{-1})_{a\sigma}^1(\omega, \omega') + [G_{a\sigma}^{\text{QI,eq}}(\omega)]^{-1} G_{a\sigma}^1(\omega, \omega') [G_{a\sigma}^{\text{QI,eq}}(\omega')]^{-1}. \quad (3.17)$$

Substituting Eq. 3.17 in Eq. 3.11 gives

$$\begin{aligned} P_{a\sigma}^\Omega(\omega) &= -\Lambda_{a\sigma}^\Omega(\omega) (\mathcal{G}_0^{-1})_{a\sigma}^1(\omega + \Omega, \omega) \\ &+ \left(1 - \Lambda_{a\sigma}^\Omega(\omega) [G_{a\sigma}^{\text{QI,eq}}(\omega + \Omega)]^{-1} [G_{a\sigma}^{\text{QI,eq}}(\omega)]^{-1}\right) G_{a\sigma}^1(\omega + \Omega, \omega). \end{aligned} \quad (3.18)$$

To find the equation relating  $\mathbf{G}^1$  to  $(\mathcal{G}_0^{-1})^1$ , we consider the solution of the quantum impurity model. The impurity Green's function is calculated from the effective action  $S_{\text{eff}}$  defined in Eq. 3.5:

$$\begin{aligned} G_{a\sigma}(\tau, \tau') &\equiv -\langle T c_{a\sigma}(\tau) c_{a\sigma}^\dagger(\tau') \rangle_{S_{\text{eff}}} \\ &= -\frac{1}{Z} \text{Tr} [T c_{a\sigma}(\tau) c_{a\sigma}^\dagger(\tau') e^{-S_{\text{eff}}}], \end{aligned} \quad (3.19)$$

where  $Z = \text{Tr} [e^{-S_{\text{eff}}}]$  is the partition function. To formulate the problem in the frequency domain, we define

$$c_{a\sigma}(\omega) = \int_0^\beta d\tau e^{i\omega\tau} c_{a\sigma}(\tau); \quad (3.20)$$

$$c_{a\sigma}^\dagger(\omega) = \int_0^\beta d\tau e^{-i\omega\tau} c_{a\sigma}^\dagger(\tau), \quad (3.21)$$

and Fourier transform the Green's function to get

$$\begin{aligned} G_{a\sigma}(\omega, \omega') &= \int_0^\beta d\tau \int_0^\beta d\tau' e^{i\omega\tau - i\omega'\tau'} G_{a\sigma}(\tau, \tau') \\ &= -\frac{1}{Z} \text{Tr} [c_{a\sigma}(\omega) c_{a\sigma}^\dagger(\omega') e^{-S_{\text{eff}}}], \end{aligned} \quad (3.22)$$



Decomposing the mean-field function into equilibrium and non-equilibrium parts

$$(\mathcal{G}_0^{-1})_{a\sigma} = (\mathcal{G}_0^{-1})_{a\sigma}^{\text{eq}}(\omega, \omega') + (\mathcal{G}_0^{-1})_{a\sigma}^1(\omega, \omega')P, \quad (3.23)$$

we have

$$S_{\text{eff}} = S_{\text{eff}}^{\text{eq}} - T^2 \sum_{\omega_1 \omega_2, a, \sigma} c_{a\sigma}^\dagger(\omega_1) (\mathcal{G}_0^{-1})_{a\sigma}^1(\omega_1, \omega_2) c_{a\sigma}(\omega_2) P. \quad (3.24)$$

Finally by linearizing the effective action  $S_{\text{eff}}$  in Eq. 3.22 we obtain an expression for  $\mathbf{G}^1$  in terms of  $(\mathcal{G}_0^{-1})^1$  and four-point function measured at equilibrium

$$\Gamma_{a\sigma, b\sigma'}^\Omega(\omega, \omega') = \left\langle c_{a\sigma}(\omega + \Omega) c_{a\sigma}^\dagger(\omega) c_{b\sigma'}(\omega') c_{b\sigma'}^\dagger(\omega' + \Omega) \right\rangle_{S_{\text{eff}}^{\text{eq}}} \quad (3.25)$$

as

$$\begin{aligned} G_{a\sigma}^1(\omega + \Omega, \omega) &= T^2 \sum_{\omega_1, b, \sigma'} \Gamma_{a\sigma, b\sigma'}^\Omega(\omega, \omega_1) (\mathcal{G}_0^{-1})_{b\sigma'}^1(\omega_1 + \Omega, \omega_1) \\ &\quad - \delta_{\Omega, 0} G_{a\sigma}^{\text{eq}}(\omega) \sum_{\omega_1, b, \sigma'} G_{b\sigma'}^{\text{eq}}(\omega_1) (\mathcal{G}_0^{-1})_{b\sigma'}^1(\omega_1, \omega_1). \end{aligned} \quad (3.26)$$

Combining these results (Eq. 3.18 and Eq. 3.26) leads to an equation which for each  $\Omega$  relates the source term  $\mathbf{P}$  (Eq. 3.13) to a linear operator (determined by a measurement of the four-point function  $\Gamma$ ) acting on  $(\mathcal{G}_0^{-1})^1$ . We find that this equation can be stably inverted; once  $(\mathcal{G}_0^{-1})^1$  is determined we obtain  $\mathbf{G}^1$  from Eq. 3.26 and  $\Sigma^1$  from Eq. 3.17.

The two particle response function can be calculated as a sum of the bubble and vertex terms:

$$\chi_{\text{bubble}}(\Omega) = T \sum_a \int^a \frac{d^2k}{(2\pi)^2} \sum_{\omega, \sigma} M_k G_{a\sigma}(k, \omega + \Omega) M_k G_{a\sigma}(k, \omega), \quad (3.27)$$

$$\chi_{\text{vertex}}(\Omega) = T \sum_a \int^a \frac{d^2k}{(2\pi)^2} \sum_{\omega, \sigma} M_k G_{a\sigma}(k, \omega + \Omega) \Sigma_{a\sigma}^1(\omega + \Omega, \omega) G_{a\sigma}(k, \omega) \quad (3.28)$$

In solving the equations for a particular response function it is convenient to

make use of the symmetries of the problem to combine terms reducing the number of components of  $\Gamma$  which need to be measured. More technical details can be found in Appendix A.

We use the numerically exact continuous-time auxiliary field (CT-AUX) impurity solver [Gull et al. (2008a)] to solve the impurity problem. Because the model is solved on the imaginary axis, an analytic continuation is required to obtain real frequency information. The quantity  $\Sigma^1(\omega, \omega')$  is a function of two frequencies, the analytic continuation of which is difficult at current stage. We therefore measure the two-particle response functions on Matsubara frequencies which is then analytic continued to real frequencies by the Maximum Entropy technique [Jarrell and Gubernatis (1996)]. One should note that the two-particle response functions are bosonic quantities, therefore the kernel for bosons (Eq. 2.53) should be used. The Kramers-Kronig relation implies the normalization of the desired function.

There are more complications for the computation of the optical conductivity. For the optical response the perturbation is a frequency dependent electric field, which enters the Hamiltonian via  $\vec{k} \rightarrow \vec{k} - \vec{A}$ . The momentum space discontinuities lead to technical complications in the formalism as discussed in Lin et al. (2009).

The conductivity  $\sigma(t)$  is a linear response function that relates a spatially uniform, time dependent (therefore transverse) electric field  $\vec{E}$  to the current  $\vec{j}$  it creates. For a system described by a Hamiltonian  $\mathbf{H} = \mathbf{H}_0 + \mathbf{U}$  with interactions  $\mathbf{U}$  which depend only on particle and spin densities (not on particle or spin currents) we have  $\vec{j}(t) = \text{Tr} [\vec{\mathbf{J}}(A)\mathbf{G}(t; \vec{A})]$ . The current operator  $\vec{\mathbf{J}}$  is obtained from the derivative of the single-particle terms  $\mathbf{H}_0$  with respect to vector potential:  $\vec{\mathbf{J}} = \delta\mathbf{H}_0/\delta\vec{A}$  while the electron Green's function  $\mathbf{G}[t; (\vec{A})] = [i\partial_t - \mathbf{H}_0[(\vec{A})] - \Sigma[(\vec{A})]]^{-1}$  is to be computed in the presence of the time dependent vector potential  $\vec{A}$ . Here bold face quantities denote matrices in the space of states of the system (including the spatial indices). Expanding to linear order in  $\vec{A}$  and introducing the diamagnetic operator  $\mathbf{K} = \delta^2\mathbf{H}_0/\delta\vec{A}^2$  and

vector operator  $\vec{\Gamma} = \delta\Sigma/\delta\vec{A}$  we obtain the current-current response function  $\chi_{jj} = \chi_{\text{dia}} + \chi_{\text{bubble}} + \chi_{\text{vertex}}$  with

$$\chi_{\text{dia}}(t-t') = \text{Tr} [\mathbf{K}G(t=0)] \delta(t-t'), \quad (3.29)$$

$$\chi_{\text{bubble}}(t-t') = \text{Tr} \left[ \vec{\mathbf{J}}\mathbf{G}(t-t')\vec{\mathbf{J}}\mathbf{G}(t-t') \right], \quad (3.30)$$

$$\chi_{\text{vertex}}(t-t') = \text{Tr} \left[ \vec{\mathbf{J}}\mathbf{G}(t-t_1)\vec{\Gamma}(t_1-t', t'-t_2)\mathbf{G}(t_2-t) \right], \quad (3.31)$$

(convolution of the internal time indices is implicit). Note that the quantity  $\mathbf{K}$  is commonly referred to as the “kinetic energy”. It is of the same order of magnitude as the expectation value of the hopping operator, and becomes identical to it in the limit of nearest-neighbor hopping. Combining the Kramers-Kronig relation between real and imaginary parts of  $\sigma$  with the gauge-invariance condition that for a non-superconducting material  $\chi_{jj}(\Omega=0) = 0$  implies

$$\chi_{\text{dia}} = \int \frac{d\omega}{\pi} \frac{\chi''_{jj}(\omega)}{\omega} = \int \frac{d\omega}{\pi} \sigma'(\omega), \quad (3.32)$$

which is the usual  $f$ -sum rule.

For the optical conductivity we require the vertex function  $\vec{\Gamma}(\omega + \Omega, \omega) \equiv \delta\Sigma/\delta\vec{A}$ , which has two sources: the explicit dependence on  $k$  arising from the momentum-space discontinuities and any additional dependence of  $\Sigma$  on  $\vec{A}$ . The additional  $\vec{A}$ -dependence arises via the impurity model from a dependence of  $\mathcal{G}_0^{-1}$  on  $\vec{A}$  as discussed earlier in this section.

The explicit momentum dependence provides a non-vanishing vertex correction arising from the momentum-space discontinuities which occur along the lines  $\vec{k}^{ab}$  separating tile  $b$  (on the larger  $k$  side) from tile  $a$  (on the smaller  $k$  side). We define  $\vec{n}^{ab}$  to be normal to this line. In the  $\Omega = 0$  limit the vertex correction is directly given by  $\delta\Sigma/\delta\vec{k}$ . To determine the vertex correction for  $\Omega \neq 0$  we consider the Ward

identity

$$\Sigma\Gamma_\rho - \vec{q} \cdot \vec{\Gamma}_J = G^{-1}(k+q, \omega+\Omega) - G^{-1}(k, \omega) \quad (3.33)$$

relating the charge  $\Gamma_\rho$  and current  $\vec{\Gamma}_J$  vertices to the inverse Green's functions. Within the DCA approximation  $\Gamma_\rho$  arises from the functional derivative of  $\Sigma$  with respect to a time dependent chemical potential. Because this perturbation is a scalar it has no contribution from the functions  $\phi_k$  and therefore cannot have any term proportional to a delta function of  $k$ . Thus we may identify the current vertex from the contributions in the Ward identity proportional to delta functions in  $k$  space, yielding

$$\vec{\Gamma}^k(\omega+\Omega, \omega) = \vec{n}^{ab} [\Sigma_b(\omega+\Omega) - \Sigma_a(\omega)] \delta \left[ (\vec{k} - \vec{k}^{ab}) \cdot \vec{n}^{ab} \right]. \quad (3.34)$$

### 3.4 Raman Scattering

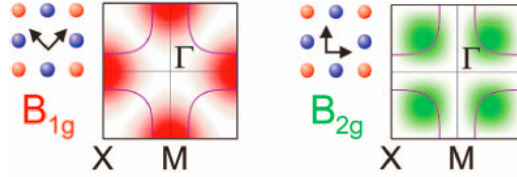


**Figure 3.3:** Polarization orientations for Raman  $B_{1g}$  and  $B_{2g}$  scattering channels. Reproduced from [Devereaux and Hackl \(2007\)](#).

Discovered independently by [Raman and Krishnan \(1928\)](#) in liquids and by [Landsberg and Mandelstam \(1928\)](#) in crystals, Raman scattering is a photon-in photon-out process, and the polarizations of the electric field vectors of the incident and emitted photons may be adjusted to highlight transitions in different regions of momentum space. We consider two scattering geometries as demonstrated in Fig. 3.3:  $B_{1g}$  for which light couples to charge excitations along the Brillouin zone axes ( $k_x$  or  $k_y = 0$ ) highlighting the antinodal region, and  $B_{2g}$  for which light couples to charge excita-

tions along the Brillouin zone diagonals ( $k_x = \pm k_y$ ) highlighting the nodal region. The perturbing terms corresponding to the  $B_{1g}$  and  $B_{2g}$  scattering channels are

$$H_{\text{Raman}}^{B_{1g}} = P \left[ \frac{1}{2} \left( \frac{\partial^2 H_0}{\partial k_x^2} - \frac{\partial^2 H_0}{\partial k_y^2} \right) \right], \quad (3.35)$$

$$H_{\text{Raman}}^{B_{2g}} = P \frac{\partial H_0^2}{\partial k_x \partial k_y}. \quad (3.36)$$

### 3.4.1 Isolated Cluster

To see the performance of the formalism discussed in Sec. 3.3, we observe that if we turn off the self-consistency condition and decouple the impurities from the bath in the DCA effective cluster model (Eq. 2.32), then our procedure reduces to the solution of an isolated cluster, which can also be solved by direct diagonalization. Specifically we consider the isolated eight-site cluster defined by the Hamiltonian:

$$H = \sum_{\mathbf{K}, \sigma} (\varepsilon_{\mathbf{K}} - \mu) c_{\mathbf{K}\sigma}^\dagger c_{\mathbf{K}\sigma} + \frac{1}{2} \sum_{\mathbf{K}, \mathbf{K}', \mathbf{Q}} \sum_{\sigma\sigma'} \frac{U}{N_c} c_{\mathbf{K}+\mathbf{Q}\sigma}^\dagger c_{\mathbf{K}'-\mathbf{Q}\sigma'}^\dagger c_{\mathbf{K}'\sigma'} c_{\mathbf{K}\sigma} \quad (3.37)$$

where  $\mathbf{K}, \mathbf{K}', \mathbf{Q} \in \{(0, 0), (\pm\pi/2, \pm\pi/2), (0, \pi), (\pi, 0), (\pi, \pi)\}$ ,  $N_c = 8$  and

$$\varepsilon_{\mathbf{k}} = -2t(\cos k_x + \cos k_y). \quad (3.38)$$

The response function for Raman scattering in  $B_{1g}$  channel is given by

$$\chi(t) = -i\Theta(t) \langle [\gamma(t), \gamma(0)] \rangle \quad (3.39)$$

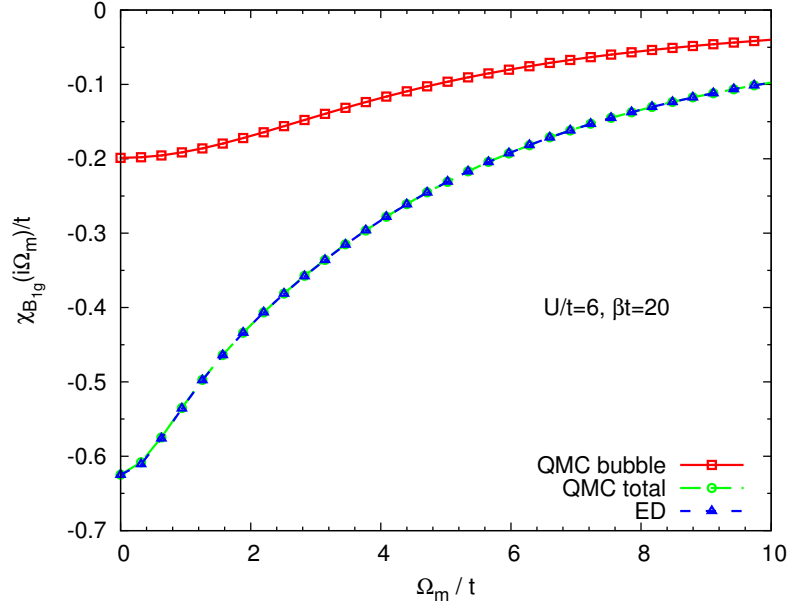


**Figure 3.4:** The comparison of Raman  $B_{1g}$  scattering intensity in isolated 8-site cluster calculated from Exact Diagonalization and quantum Monte Carlo as a function of Matsubara frequencies. The parameters are  $U/t = 6$ ,  $\beta t = 20$  as indicated.

where  $\gamma = 2t \sum_{\sigma} (n_{\sigma,(0,\pi)} - n_{\sigma,(\pi,0)})$ . For  $t > 0$ ,

$$\chi(t) = -\frac{i}{Z} \sum_n \langle n | e^{-\beta H} (e^{iHt} \gamma e^{-iHt} \gamma - \gamma e^{iHt} \gamma e^{-iHt}) | n \rangle \quad (3.40)$$

$$= -\frac{i}{Z} \sum_{nm} e^{-\beta E_n} \langle n | \gamma | m \rangle \langle m | \gamma | n \rangle (e^{i(E_n - E_m)t} - e^{i(E_m - E_n)t}). \quad (3.41)$$

The Fourier transform gives

$$\chi(\omega) = \int_0^{\infty} e^{i\omega t} \chi(t) dt \quad (3.42)$$

$$= \frac{1}{Z} \sum_{nm} \frac{|\langle m | \gamma | n \rangle|^2}{\omega + E_n - E_m} (e^{-\beta E_n} - e^{-\beta E_m}). \quad (3.43)$$

Fig. 3.4 compares the Raman  $B_{1g}$  response function on Matsubara frequencies resulting from our procedure (as outlined in Sec. 3.3) applied to the isolated eight-

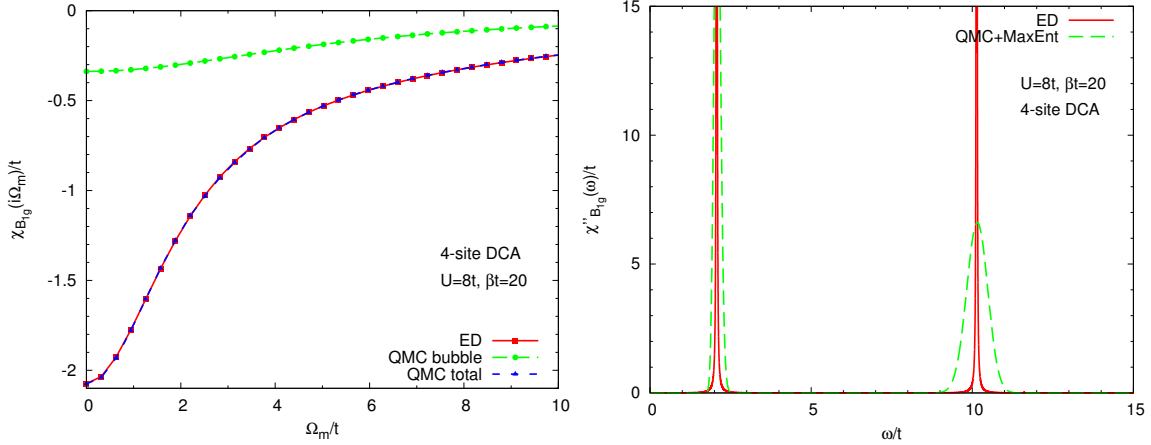


**Figure 3.5:** The comparison of Raman  $B_{1g}$  scattering intensity in isolated 4-site cluster calculated from Exact Diagonalization and quantum Monte Carlo as a function of Matsubara (left panel) and real (right panel) frequencies. The parameters are  $U/t = 8, \beta t = 20$  as indicated.

site cluster to that obtained from a direct diagonalization of the same cluster via Eq. 3.43. The parameters are  $U = 6t$  and the temperature  $T = t/20$ . The vertex corrections are seen to have significant contributions to the response function, and are well estimated by our formalism.

Fig. 3.5 compares the calculated Raman  $B_{1g}$  scattering intensity in an isolated 4-site cluster defined by Eq. 3.37 with  $\mathbf{K}, \mathbf{K}', \mathbf{Q} \in \{(0, 0), (0, \pi), (\pi, 0), (\pi, \pi)\}$  and  $N_c = 4$ . The left panel displays the Raman response on Matsubara frequencies which shows nice agreement between the ED and QMC approximations including the vertex correction. To demonstrate the reliability of the Maximum Entropy analytic continuation method, in the right panel of Fig. 3.5 we compare the real axis spectrum obtained by analytic continuation of the QMC data to that obtained directly from the exact solution. Apart from a broadening which may be an artifact of Maximum Entropy method, the two procedures give very similar results; in particular we have verified that the areas of the peaks are the same in the two methods.

### 3.4.2 Two Dimensional Square Lattice

We apply our methodology to determine the Raman response of the one-band Hubbard model on two dimensional square lattice. The matrix element is  $\gamma_{ab} = \frac{1}{2}(\partial^2 \varepsilon_k / \partial k_x^2 - \partial^2 \varepsilon_k / \partial k_y^2)$  in  $B_{1g}$  channel and  $\gamma_{ab} = \partial^2 \varepsilon_k / \partial k_x \partial k_y$  in  $B_{2g}$  channel.

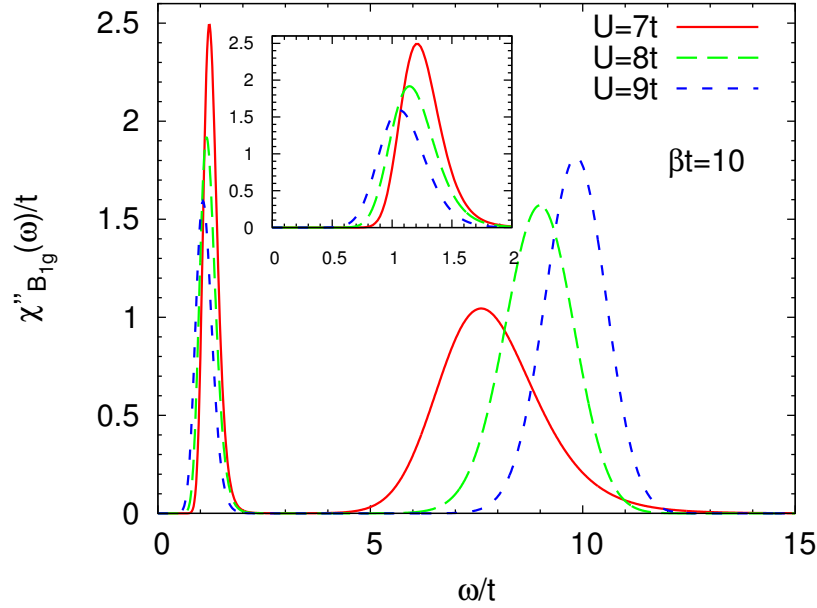


**Figure 3.6:** Raman  $B_{1g}$  scattering intensity calculated from the 4-site DCA approximation to the two dimensional Hubbard model for  $U = 7t, 8t, 9t$ ,  $t' = -0.15t$  and  $\beta t = 10$  at half-filling.

Fig. 3.6 shows the calculated Raman  $B_{1g}$  response in the 4-site DCA approximation to the half-filled two-dimensional Hubbard model for the interaction strength  $U = 7t, 8t, 9t$ . In the 4-site DCA approximation a metal-insulator transition is evident as  $U$  is increased through  $U_{\text{MIT}} \approx 4.2t$  [Gull et al. (2008b)]. The insulating gap is visible for  $U > U_{\text{MIT}}$ . In the Raman  $B_{1g}$  spectra, besides the above gap absorption which can be understood by the excitation from the filled lower Hubbard band to the empty upper Hubbard band, we also see a clear peak inside the insulating gap. As the interaction strength  $U$  increases, the maximum of the low frequency peak decreases. These excitations at an energy of about  $t \sim 350$  meV are similar to the



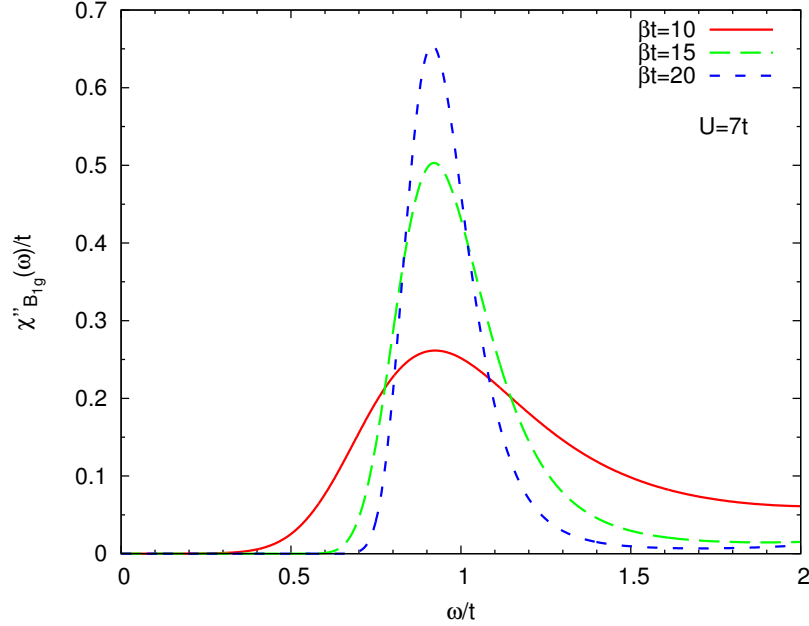


**Figure 3.7:** Raman  $B_{1g}$  scattering intensity calculated from the 8-site DCA approximation to the two dimensional Hubbard model for parameters  $U = 7t$ ,  $t' = -0.15t$  at half-filling and the temperatures indicated.

“two-magnon” excitations reported in the thoroughly studied insulating parent compounds of the cuprates [Devereaux and Hackl (2007)]. The “two-magnon” excitations are driven by superexchange between two nearest-neighbor spins in an antiferromagnetic environment [Blumberg et al. (1994)], and the position of the “two-magnon” peak is approximately proportional to the short-range exchange coupling  $J \sim t^2/U$ . This is in qualitative agreement with our finding shown in Fig. 3.6.

Fig. 3.7 shows the Raman  $B_{1g}$  scattering intensity calculated for  $U = 7t$  at half-filling using the 8-site DCA approximation. The “two-magnon” peak is observed at roughly  $0.92t \sim 320$  meV which softens and broadens as the temperature is increased from  $T = t/20$  to  $T = t/10$ . The position of the “two-magnon” peak is approximately independent of the temperature. We compare the Raman  $B_{1g}$  spectra obtained from the 4-site and 8-site DCA calculation in a wide frequency range in Fig. 3.8. The parameters are the same, i.e.  $U = 7t, t' = -0.15t$  and  $\beta t = 10$ . We see that the

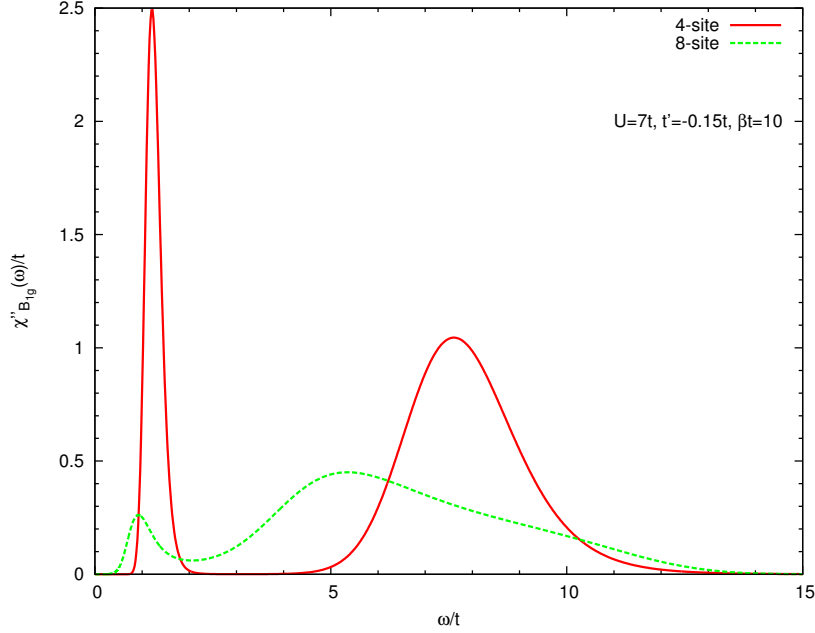


**Figure 3.8:** Raman  $B_{1g}$  scattering intensity calculated from the 4-site and 8-site DCA approximations to the half-filled two dimensional Hubbard model for parameters  $U = 7t$ ,  $t' = -0.15t$  and  $\beta t = 10$ .

total spectral weight in the Raman  $B_{1g}$  spectra decreases as the cluster size increases from 4-site to 8-site. Further, the frequency and the relative intensity of the “two-magnon” peaks strongly depend on the cluster size, suggesting that the calculation of the Raman  $B_{1g}$  scattering intensity has not yet converged with respect to the cluster size. In the 8-site DCA, the position of the “two-magnon” peak is at a lower frequency and is much weaker. The comparison suggests the difference in the physics present in the 4-site and 8-site DCA approximations.

We present the evolution of the “two-magnon” peak with doping in the 8-site DCA calculations in Fig. 3.9. When the insulator is doped away from half-filling, a quasiparticle feature (evidenced by the linear increase in scattering intensity at low frequency) appears, while the “two-magnon” peak broadens, shifts down in frequency, and eventually merges with the quasiparticle peak. The “two-magnon” peak in Raman  $B_{1g}$  scattering persists for a wide doping range but the position of the maximum

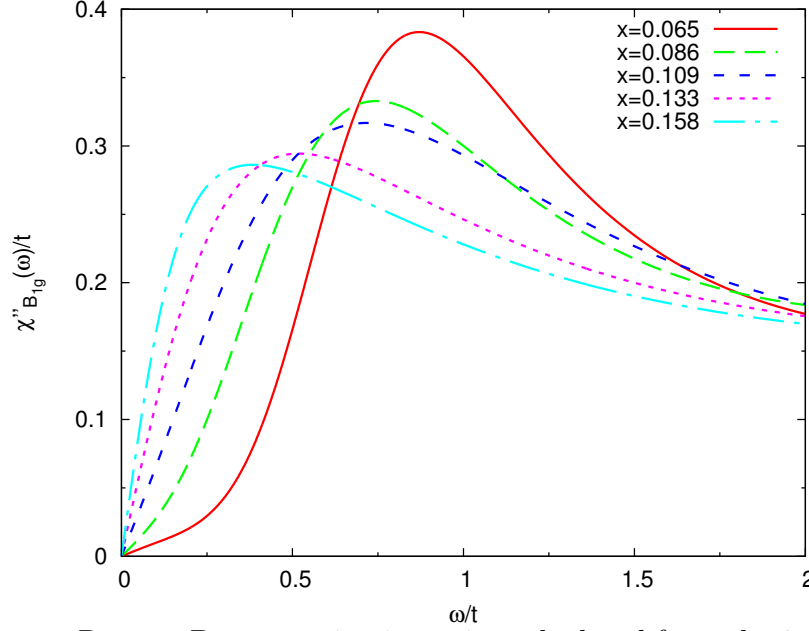


**Figure 3.9:** Raman  $B_{1g}$  scattering intensity calculated from the 8-site DCA approximation to the two dimensional Hubbard model for parameters  $U = 7t$ ,  $t' = -0.15t$  and  $\beta t = 20$  at various dopings as indicated.

and the peak intensity decrease as doping is increased, which implies the existence of the short-range antiferromagnetic correlations even at high doping levels. A rapid steepening of the initial slope with doping is evident. For dopings  $x = 0.065$  and  $x = 0.086$  the pseudogap is visible as a change in slope from the very low frequency regime (dominated by quasiparticles) to an intermediate energy regime where much of the scattering comes from the “two-magnon” feature. This is further demonstrated by Fig. 3.10 which shows the decomposition of the spectrum at half-filling and doping level  $x = 0.086$ . The vertex correction (i.e. difference between total and bubble spectrum), which in the insulating state gives rise to the “two-magnon” excitation, makes a significant contribution to the scattering intensity away from the very low frequency regime at  $x = 0.086$ . As the doping is increased the vertex correction decreases in importance and becomes completely negligible at very high dopings.

Fig. 3.11 shows the temperature dependence of the calculated Raman scattering intensity in  $B_{1g}$  channel at doping level  $x = 0.065$  (upper panel) and  $x = 0.16$  (lower

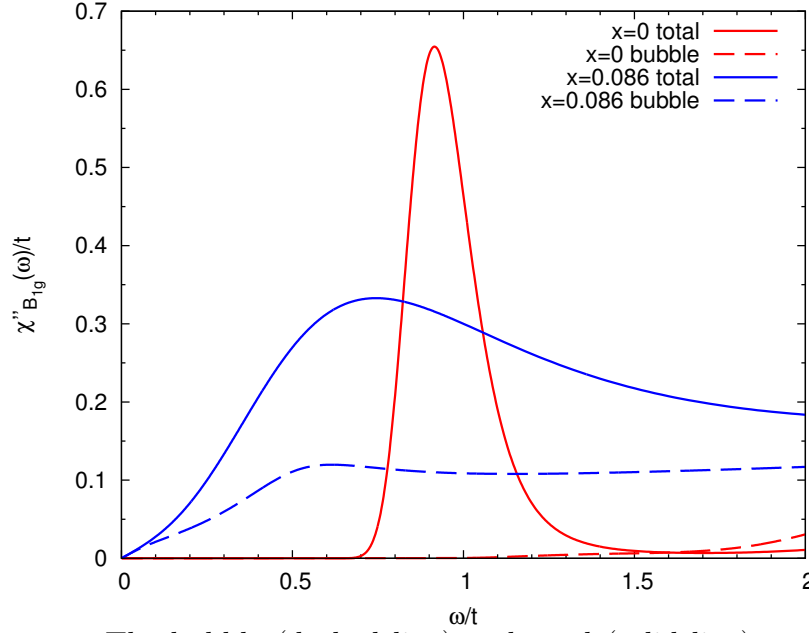


**Figure 3.10:** The bubble (dashed line) and total (solid line) contribution to the Raman  $B_{1g}$  scattering intensity calculated from the 8-site DCA approximation to the two dimensional Hubbard model for parameters  $U = 7t$ ,  $t' = -0.15t$  and  $\beta t = 20$ .

panel). We see a change in sign of the temperature dependence of the Raman  $B_{1g}$  scattering intensity. At the lower doping the low-frequency Raman  $B_{1g}$  intensity is suppressed as the temperature decreases, whereas at the higher doping the initial slope is seen to increase as the temperature decreases.

The broadening of the “two-magnon” peak with temperature and doping is qualitatively consistent with the  $B_{1g}$  Raman scattering experiments on the hole doped side [Reznik et al. (1993); Blumberg et al. (1994); Rübhausen et al. (1999); Sugai et al. (2003)] of the phase diagram, which has been studied theoretically on clusters for the  $t - J$  model [Prelovšek and Jaklič (1996)] and by QMC techniques [Sandvik et al. (1998)].

We next turn to the Raman scattering in  $B_{2g}$  channel. The 8-site cluster is the smallest size for which the Raman  $B_{2g}$  response function has a non-trivial  $\delta\Sigma/\delta P$  vertex correction. We present the doping dependence of the Raman  $B_{2g}$  spectra in

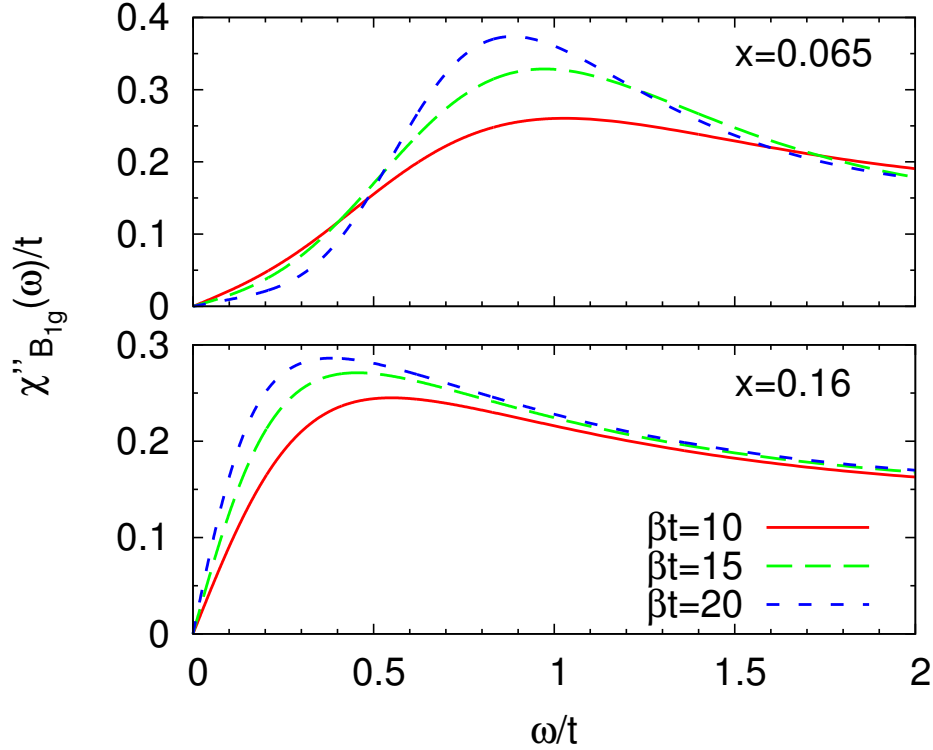


**Figure 3.11:** Temperature dependence of the Raman  $B_{1g}$  scattering intensity calculated from the 8-site DCA approximation to the two dimensional Hubbard model for parameters  $U = 7t$ ,  $t' = -0.15t$  at hole doping 0.065 (upper panel) and 0.16 (lower panel).

8-site DCA approximation in Fig. 3.12. We see qualitative differences in  $B_{2g}$  spectra, in particular there is no “two-magnon” feature observed in  $B_{2g}$  scattering. The overall  $B_{2g}$  scattering intensity is 1-2 orders of magnitude smaller than  $B_{1g}$  intensity. The vertex correction produces a peak at  $\sim 0.18t$  away from half-filling which is roughly doping independent. This feature has not been reported in experiments, and is not fully understood yet.

Raman  $B_{2g}$  scattering highlights the nodal region (sector  $B$  in 8-site cluster) which is not affected by the pseudogap and the quasiparticle velocity is high. This region may therefore also be expected to dominate the optical conductivity. In metals the Raman spectra are related to the product of the frequency and the optical conductivity as  $\omega\sigma'(\omega) \propto \chi''_{\gamma\gamma}(\omega)$ . The main panel of Fig. 3.13 shows the Raman  $B_{2g}$  spectra

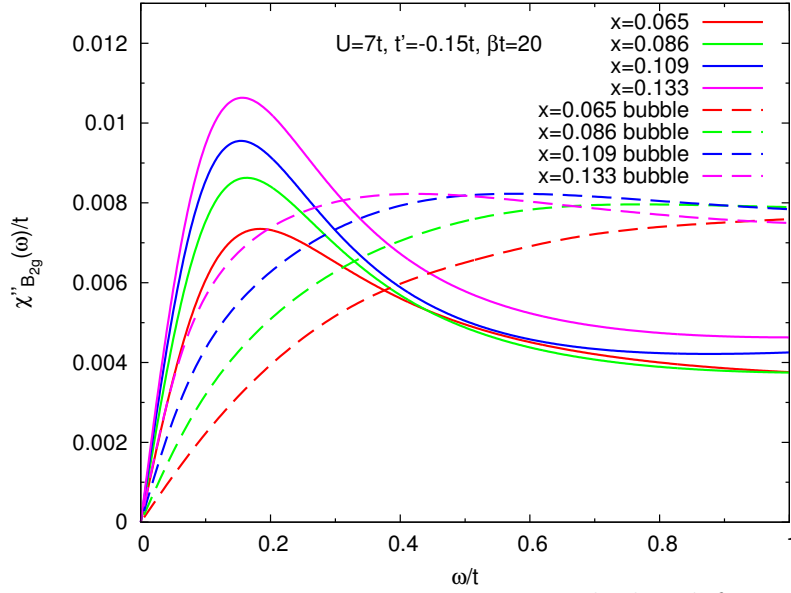


**Figure 3.12:** Raman  $B_{2g}$  scattering intensity calculated from the 8-site DCA approximation to the two dimensional Hubbard model for parameters  $U = 7t$ ,  $t' = -0.15t$  and  $\beta t = 20$  at various hole dopings as indicated.

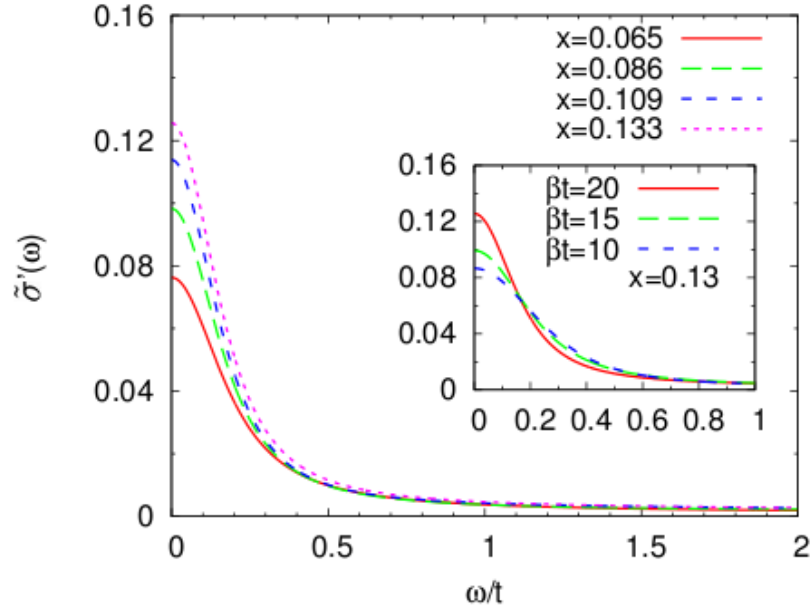


**Figure 3.13:** Main panel: The "reinterpreted" optical conductivity defined as  $\text{Re}\tilde{\sigma}(\omega) = \text{Im}\chi_{B_{2g}}(\omega)/\omega$  at  $U = 7t$  and inverse temperature  $\beta = 20/t \approx 200$  K for hole dopings indicated. Inset: temperature dependence of the low frequency "reinterpreted" optical conductivity for hole doping  $x = 0.16$ .

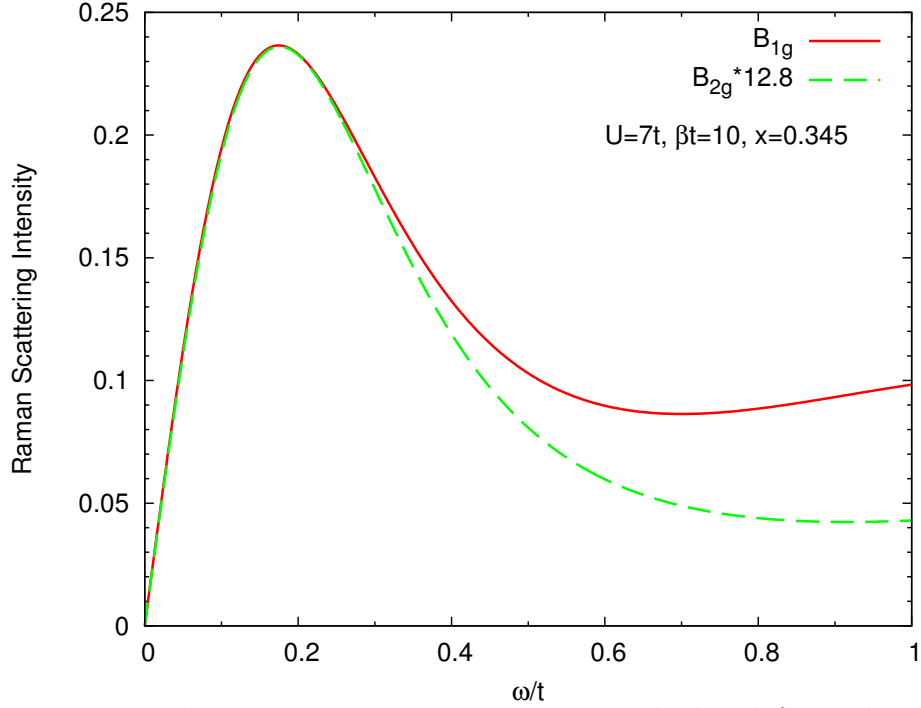


**Figure 3.14:** The Raman scattering intensity calculated from the 8-site DCA approximations to the two dimensional Hubbard model in the high doping “isotropic Fermi liquid” region in the  $B_{1g}$  and  $B_{2g}$  channels for doping  $x = 0.345$ . Note that the a scaling factor of 12.8 was applied to the Raman  $B_{2g}$  spectra to make the magnitude comparable to the Raman  $B_{1g}$  spectra.

“reinterpreted” as an optical conductivity. We see a “Drude” peak centered at zero frequency which grows noticeably and sharpens as doping is increased, and a broad higher-frequency continuum which is only weakly doping dependent. The inset shows a growth of the “Drude” peak with decreasing temperature at higher dopings. These features bear a qualitative resemblance to the optical conductivity data taken in the high- $T_c$  cuprate superconductors.

Gull *et al.* (2010) presents a systematic analysis of the doping-driven metal-insulator transition in the two-dimensional Hubbard model using cluster dynamical mean-field theory. A high-doping “isotropic Fermi liquid” region was reported, where the momentum dependence of the self-energy is very weak and the properties are those of a Fermi liquid with moderate renormalization and are well described by the

single-site DMFT. The calculations at the high hole doping level inside the “isotropic Fermi liquid” region shows that the vertex corrections make negligible contribution to the Raman scattering intensity in both  $B_{1g}$  and  $B_{2g}$  channels. Furthermore, as shown in Fig. 3.14, the functional forms are similar in the two scattering channels, up to a scaling factor, at low frequencies which is expected due to the isotropic scattering properties along Fermi surface in this region.

## 3.5 Optical Conductivity

In this section we apply the formalism to calculate the optical conductivity in two-dimensional Hubbard model defined in Eq. 3.1 that is solved by the DCA implementation of the cluster dynamical mean-field theory, using the 4-site cluster in which the vertex correction arising from the additional dependence of the self-energy on the vector potential  $\vec{A}$  vanishes as discussed in Sec. 3.5.1, and the 8-site cluster in which the two sources of the dependence of the self-energy on  $\vec{A}$  both contribute to the vertex correction as discussed in Sec. 3.5.2.

The current operator for the  $x$  direction is

$$j_x = 2t \sin k_x + 4t' \sin k_x \cos k_y \quad (3.44)$$

and the kinetic-energy operator  $K = 2t \cos k_x + 4t' \cos k_x \cos k_y$ .

### 3.5.1 4-site DCA

The canonical tiling for the 4-site cluster (top right in Fig. 3.2) produces momentum sectors with symmetry such that the optical conductivity source term (Eq. 3.13) vanishes, thus as noted by Jarrell et al. (1995) and Haule and Kotliar (2007) there



is no explicit dependence of  $\Sigma_a$  on  $A$ . [Haule and Kotliar \(2007\)](#) further argued that for the 4-site cluster all vertex corrections vanished. This is incorrect, although the vertex corrections turn out to be unimportant for the situation of interest to [Haule and Kotliar \(2007\)](#).

Therefore in the 4-site DCA Eq. 3.34 is the appropriate vertex correction. We restrict attention to the paramagnetic phase. Parameters relevant to high-temperature copper-oxide superconductors are  $t \approx 0.35$  eV,  $t' \approx -0.3t$  [[Andersen et al. \(1995\)](#)] and  $U \sim 9t$  [[Comanac et al. \(2008\)](#)]. The precision of calculations for  $t' \neq 0$  or  $n \neq 1$  is limited by a fermion sign problem; we therefore present results for  $U = 6t$  and  $t' = 0$  where higher precision data can be obtained.

The analytic continuation of the optical conductivity to real frequencies may be done in two ways: either by continuing the self-energies [[Wang et al. \(2009\)](#)] and then computing the conductivity or by continuing directly the Matsubara-axis conductivity using the Kramers-Kronig relation:

$$\sigma(i\omega_n) = \int_{-\infty}^{\infty} \frac{d\omega}{\pi} \frac{\text{Re}\sigma(\omega)}{i\omega_n - \omega}. \quad (3.45)$$

The continuations are tested by comparing the directly computed Matsubara axis  $\sigma(i\Omega_n)$  to the same quantity “back-computed” from the continuation. Significant differences in real-axis conductivity correspond to variations of a few times  $10^{-4}$  in  $\sigma(i\Omega_n)$ , setting a stringent requirement on the quality of the data. The inset of Fig. 3.15 presents highly precise data obtained at the sign-problem-free parameters  $U = 6t$  and  $t' = 0$ ; we see that the two continuation methods yield similar results; differences between them are a measure of the best-case uncertainties in the continued  $\sigma$ . At  $U = 9t$  and  $t' = -0.3t$  the differences between the methods are larger; in particular the gap edges are much broader in the traces obtained by continuing the Matsubara axis response functions; we believe this broadening is unphysical for the reasons given in [Wang et al. \(2009\)](#). The conductivity obtained from continuing  $\sigma(i\Omega_n)$  is found

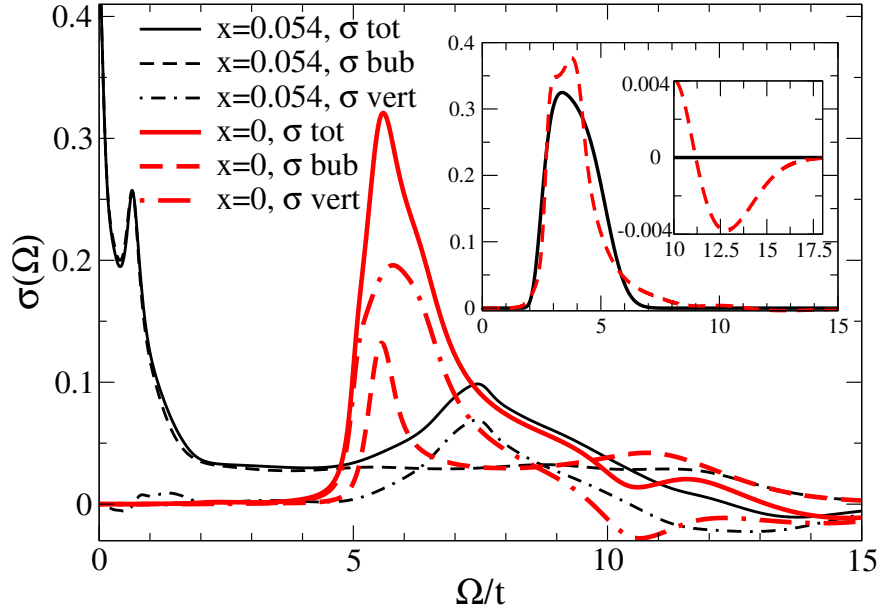


**Figure 3.15:** Main panel: conductivity calculated from 4-site DCA approximation to one-band Hubbard model for  $U = 9t$ ,  $t' = -0.3t$  and dopings  $x = 0$  (heavy lines, red on-line) and 0.054 (light lines, black on-line) by continuing self-energy. Full lines: conductivity; dashed lines: contribution to conductivity from convolution of bubble diagrams Eq. 3.30; dash dotted lines: contribution from vertex corrections, Eq. 3.31. Larger Inset: comparison of conductivity computed by continuing self-energy (dashed line, red on-line) and continuing Matsubara response function (solid line, black on-line) at  $U = 6t$  and  $t' = 0$ . Smaller inset: expansion of high frequency negative conductivity region for  $U = 6t$  and  $t' = 0$ .

in general to produce a back-continued  $\sigma$  in worse agreement with original data than the conductivity obtained by continuing the self-energy; we therefore present results obtained from the latter method. One difficulty must be noted. As can be seen from Fig. 3.15, in the high frequency regime (frequencies well above the gap) the vertex correction acts to cut off the high frequency tail found in  $\chi_{\text{bubble}}$ , adding a negative contribution to the positive-definite  $\chi_{\text{bubble}}$  so that the total contribution nearly vanishes. In calculations based on continuing the self-energy first, the vertex correction in fact overcompensates, leading to an unphysical negative conductivity for some high frequencies (if  $\sigma(i\Omega_n)$  is directly continued the  $\sigma'(\omega)$  is by construction positive). We

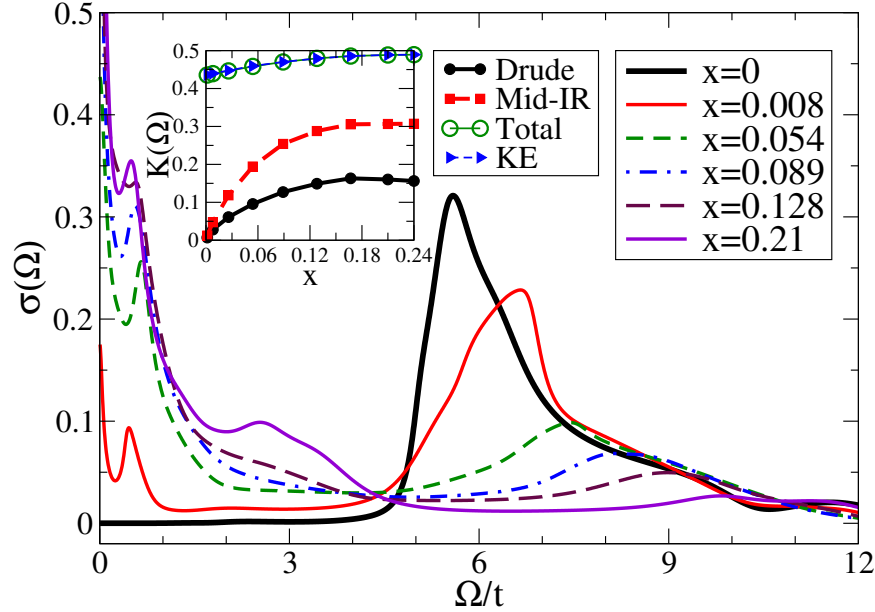


**Figure 3.16:** Optical conductivity calculated for indicated dopings using 4-site DCA approximation to the paramagnetic phase of the two-dimensional one-band Hubbard model at parameters corresponding to high-temperature superconductors at temperature  $T \approx 400K$  and other parameters described in the text. Inset:  $2/\pi$  times integral of optical conductivity over low frequency  $\Omega < 0.6t$  (“Drude”, solid line, black on-line), intermediate frequency  $\Omega = 2t$  (“Mid-IR”, long-dashed line, red on-line), and all frequencies (“Total”, light solid line, green on-line), along with independently computed kinetic energy (“KE”, light dashed line, blue on-line).

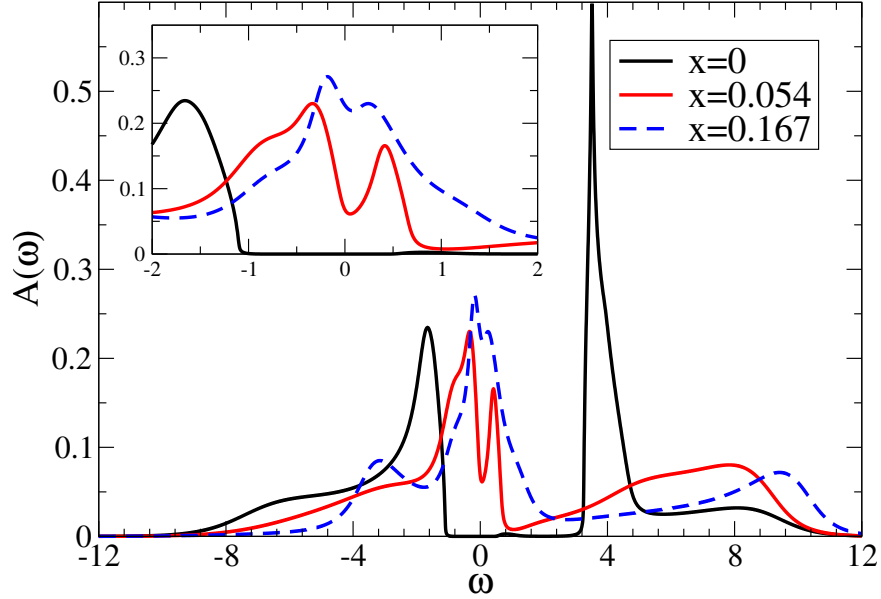
believe that the overcompensation is a numerical artifact. Our numerical uncertainties, both from the QMC measurement and the analytic continuation, are largest in this regime. The magnitude of the unphysical negative contribution is small: for our  $U = 9t$  calculations the spectral weight in the negative region ranges from 5% of the total spectral weight at  $x = 0$  to 0.4% at our highest doping. Further, the overshoot is found to decrease as the numerical accuracy of our computation is improved and as seen from the second inset to Fig. 3.15 can be made smaller than 2% of the total spectral weight in our best case. However, to date we have been unable to eliminate the negative region entirely.

Fig. 3.16 shows the doping dependence of the calculated optical conductivity. The

curves bear a striking similarity to the conductivity of hole-doped high-temperature superconductors [Uchida et al. (1991); Basov and Timusk (2005)]. The conductivity calculated for the undoped system displays a characteristic insulating spectrum with a gap  $\sim 5t \approx 1.8eV$  similar in magnitude to that observed in  $\text{La}_2\text{CuO}_4$  and an above-gap absorption strength corresponding to  $\sim 1300\Omega^{-1}\text{cm}^{-1}$  about 30% larger than observed. On doping, this gap is rapidly destabilized, again in a manner consistent with measurements. Absorption in the near-gap region is suppressed, while substantial absorption strength appears at low frequencies. As the doping is increased the optical response may be described in terms of a “Drude” peak indicating coherent quasiparticle motion, an additional “mid-IR” feature ( $\omega \sim 0.5t$ ) and a high frequency tail. By the highest doping the conductivity has evolved to the “Drude peak” plus weak high frequency tail characteristic of Fermi-liquid metals.

To further characterize the evolution of the conductivity we present in the inset of Fig. 3.16 the partial optical integrals  $K(\Omega) = \frac{2}{\pi} \int_0^\Omega d\omega \sigma(\omega)$  for a low frequency ( $\Omega = 0.6t$  encompassing the Drude peak), an intermediate frequency  $\Omega = 2t$ , somewhat less than half of the gap value and the total integral  $\Omega \rightarrow \infty$  (which is seen to agree with the independently calculated kinetic energy). The shift of spectral weight, first into a mid-IR band and then into a Drude peak is very similar to observations in high- $T_c$  cuprates, although the calculated mid-IR spectral weight is higher than values inferred from data (see e.g. Fig. 1 in Uchida et al. (1991); Comanac et al. (2008)).

The main panel of Fig. 3.15 presents the conductivity for  $t' = -0.3t$  and  $U = 9t$  as well as its decomposition into “bubble” (Eq. 3.30) and “vertex” (Eq. 3.31) contributions for dopings  $x = 0$  and  $x = 0.054$ . The vertex correction is seen to make a non-negligible contribution to the conductivity and to be essential to fulfilling the  $f$ -sum rule. It decreases in importance as doping increases, as expected because with increased doping the self-energy becomes more isotropic in momentum space.



**Figure 3.17:** Main panel: Density of states calculated for the sector containing the Fermi surface from 4-site DCA approximation at  $U = 9t$  and  $t' = -0.3t$  at dopings indicated. Inset: expansion of the near-Fermi-surface region.

This aspect of our result disagrees with [Chakraborty et al. \(2008\)](#) which stated (on the basis of a comparison of a 4-site CDMFT conductivity computed without vertex corrections to the f-sum rule) that vertex corrections were unimportant near half filling and increased in importance as the doping increased; on the other hand at lower frequencies and higher dopings where vertex corrections are of less importance our result is similar to that of [Chakraborty et al. \(2008\)](#). The origin of the difference is not clear.

At  $x = 0$  the vertex corrections bring two effects: they increase the magnitude of the conductivity in the above-gap region and they steepen the rate at which the conductivity rises above the gap edge. We believe that these two effects are consequences of the short ranged order captured by the DCA approximation. Inspection of the Green function (not shown here) indicates that on the single-particle level the state is an indirect-gap insulator with the highest energy filled states at a different

momentum from the lowest energy empty states. As shown e.g. in [Comanac et al. \(2008\)](#) and [Wang et al. \(2009\)](#), the backfolding associated with long-ranged order converts the indirect gap to a direct one, dramatically steepening the conductivity onset. The vertex correction provides a similar effect. The vertex correction also expresses the “coherence factor” physics associated with strong two-sublattice spatial correlations. To see this, consider a mean-field model of a material with two-sublattice order, for which the electron propagator has “normal” ( $G \sim \langle c_k c_k^\dagger \rangle$ ) and “anomalous” ( $F \sim \langle c_k c_{k+Q}^\dagger \rangle$ ) parts given by  $G(k, \omega) = (\omega - \varepsilon_{k+Q}) / ((\omega - \varepsilon_k)(\omega - \varepsilon_{k+Q}) - \Delta^2) = 1 / (\omega - \varepsilon_k - \Delta^2 / (\omega - \varepsilon_{k+Q}))$  and  $F(k, \omega) = \Delta^2 / ((\omega - \varepsilon_k)(\omega - \varepsilon_{k+Q}) - \Delta^2)$  respectively. The conductivity in the ordered state is computed from the sum of a “ $G - G$ ” and an “ $F - F$ ” bubble which give equal contributions to the conductivity for frequencies near the gap edge. The state uncovered in the 4-site DCA calculation has no long ranged order, so the anomalous ( $F$ ) part vanishes and convolution of bubble diagrams would capture only the  $G - G$  contribution. The vertex corrections in effect add back the  $F - F$  term.

The conductivity is related to the electron spectral function, shown in [Fig. 3.17](#). The initial doping moves the chemical potential into the lower Hubbard band and rapidly broadens the sharp peak at the edge of the upper Hubbard band; we see also from [Fig. 3.16](#) that the form of the near-gap-edge conductivity changes substantially. Interestingly, in the doped materials the remains of the above-gap absorption is entirely expressed by the vertex correction. At intermediate dopings  $x = 0.054$  and  $0.089$  the many-body density of states exhibits a “pseudogap”, a small gap at the Fermi level previously noted [[Civelli et al. \(2005\)](#); [Gull et al. \(2008b\)](#); [Ferrero et al. \(2009b\)](#)]. Excitations across the pseudogap have the correct energy to account for the mid-IR feature observed in the data and in high- $T_c$  materials (a similar connection was made in [Choy et al. \(2008\)](#); [Chakraborty et al. \(2008\)](#)).

### 3.5.2 8-site DCA

It is apparent that in the 8-site DCA approximation the vertex correction due to the additional dependence of the self-energy on the perturbation makes non-trivial contributions to the optical conductivity. However the situation is more involved for the optics vertex than that is discussed in Sec. 3.3 for a general two-particle response function. For the optics vertex, there is a contribution from the momentum space discontinuities, which must be taken into account both in the construction of the vertex (similar in the 4-site DCA) and in the determination of the changes to the self-energy  $\Sigma_a$ . However it remains to be investigated how the vector potential  $\vec{A}$  enters the  $k$ -discontinuities in determining the additional contribution to the source term (Eq. 3.13).

We revisit the DMFT self-consistency equation in DCA:

$$G_{a\sigma}^{\text{QI}}(\omega) = \int \frac{d^2k}{(2\pi)^2/N_c} \phi_a(k) \left[ \omega + \mu - \varepsilon_k - \sum_b \phi_b(k) \Sigma_{b\sigma} \phi_b(k) \right]^{-1} \phi_a(k). \quad (3.46)$$

Our present understanding is to put  $\vec{A}$  everywhere in Eq. 3.46. Linearizing Eq. 3.46 in the vector potential  $\vec{A}$  we have

$$\begin{aligned} \frac{\delta G_{a\sigma}^{\text{QI}}}{\delta A} = & \int \frac{d^2k}{(2\pi)^2/N_c} \left\{ \left[ \phi'_a G_{a\sigma}(k, \omega) \phi_a + \phi_a G_{a\sigma}(k, \omega + \Omega) \phi'_a \Sigma_{a\sigma}(\omega) \phi_a G_{a\sigma}(k, \omega) \right] \right. \\ & + \left[ \phi_a G_{a\sigma}(k, \omega + \Omega) \phi_a \Sigma_{a\sigma}(\omega + \Omega) \phi'_a G_{a\sigma}(k, \omega) + \phi_a G_{a\sigma}(k, \omega + \Omega) \phi'_a \right] \\ & \left. + \left[ \phi_a G_{a\sigma}(k, \omega + \Omega) \left( -\frac{\partial \varepsilon_k}{\partial k} + \Sigma_{a\sigma}^1(\omega + \Omega, \omega) \right) G_{a\sigma}(k, \omega) \phi_a \right] \right\}. \end{aligned} \quad (3.47)$$

Use the relation  $\Sigma_{a\sigma} = (\mathcal{G}_0^{-1})_{a\sigma} - G_{a\sigma}^{-1}$  and drop redundant  $\phi_a$ , we obtain

$$\begin{aligned}
\frac{\delta G_{a\sigma}^{\text{QI}}}{\delta A} &= \int \frac{d^2k}{(2\pi)^2/N_c} \left\{ \left[ \phi'_a G_{a\sigma}(k, \omega) \phi_a + \phi_a G_{a\sigma}(k, \omega + \Omega) \phi'_a \right] \right. \\
&\quad + \left[ \phi_a G_{a\sigma}(k, \omega + \Omega) (\omega + \mu - \varepsilon_k) G_{a\sigma}(k, \omega) \phi'_a - \phi_a G_{a\sigma}(k, \omega + \Omega) \phi'_a \right] \\
&\quad + \left[ \phi_a G_{a\sigma}(k, \omega + \Omega) (\omega + \Omega + \mu - \varepsilon_k) G_{a\sigma}(k, \omega) \phi'_a - \phi'_a G_{a\sigma}(k, \omega) \phi_a \right] \\
&\quad \left. + \left[ \phi_a G_{a\sigma}(k, \omega + \Omega) \left( -\frac{\partial \varepsilon_k}{\partial k} + \Sigma_{a\sigma}^1(\omega + \Omega, \omega) \right) G_{a\sigma}(k, \omega) \phi_a \right] \right\} \quad (3.48) \\
&= \int \frac{d^2k}{(2\pi)^2/N_c} \phi_a G_{a\sigma}(k, \omega + \Omega) [2\omega + \Omega + 2(\mu - \varepsilon_k)] G_{a\sigma}(k, \omega) \phi'_a \\
&\quad + \int \frac{d^2k}{(2\pi)^2/N_c} \phi_a G_{a\sigma}(k, \omega + \Omega) \left( -\frac{\partial \varepsilon_k}{\partial k} \right) G_{a\sigma}(k, \omega) \phi_a \\
&\quad + \int \frac{d^2k}{(2\pi)^2/N_c} G_{a\sigma}(k, \omega + \Omega) \Sigma_{a\sigma}^1(\omega + \Omega, \omega) G_{a\sigma}(k, \omega).
\end{aligned}$$

If  $\vec{A}$  is positive, the first term in the last equality of Eq. 3.48 is to be evaluated at the boundary separating sectors  $a$  and  $a_+$  (the immediately adjacent sector to  $a$  in the “+” direction), and with a “−” sign at the boundary which separates sectors  $a$  and  $a_-$  (the immediately adjacent sector to  $a$  in the “−” direction).

For consistence we define the source term for the optics vertex as:

$$\begin{aligned}
P_{a\sigma}^\Omega(\omega) &= \int \frac{d^2k}{(2\pi)^2/N_c} \phi_a G_{a\sigma}(k, \omega + \Omega) [2\omega + \Omega + 2(\mu - \varepsilon_k)] G_{a\sigma}(k, \omega) \phi'_a \\
&\quad + \int \frac{d^2k}{(2\pi)^2/N_c} \phi_a G_{a\sigma}(k, \omega + \Omega) \left( -\frac{\partial \varepsilon_k}{\partial k} \right) G_{a\sigma}(k, \omega) \phi_a. \quad (3.49)
\end{aligned}$$

Compared to the source term for a general two-particle response function as in Eq. 3.13, the  $k$ -discontinuity introduces an additional boundary term shown as the first term in Eq. 3.49.

The current-current response function can be evaluated from the sum of the quasiparticle contribution (Eq. 3.27), the vertex correction constructed from the  $k$ -discontinuity of the self-energy (Eq. 3.34), and the vertex correction due to the change



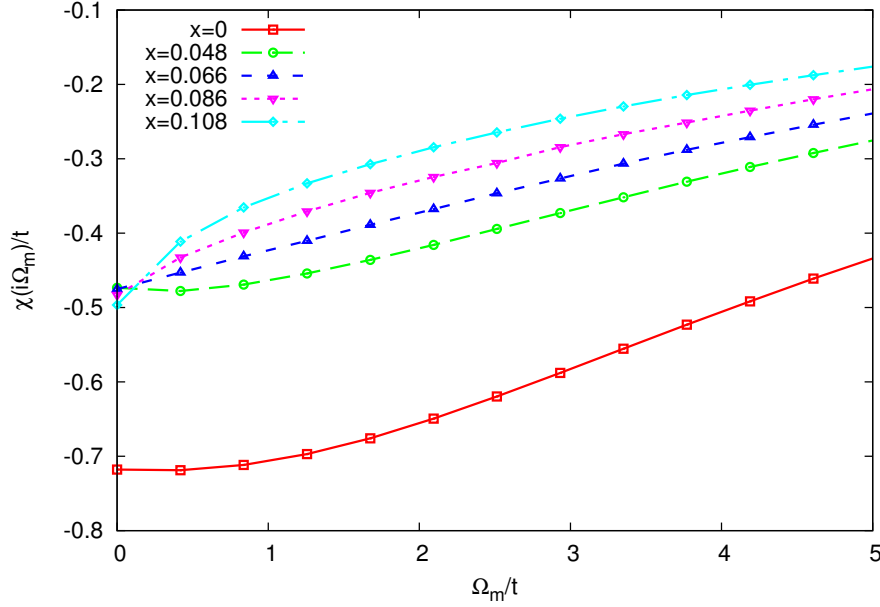


**Figure 3.18:** The calculated current-current response function  $\chi(i\Omega_m)$  at various doping levels in the 8-site DCA approximation which includes the vertex correction from Eq. 3.34 and 3.49. The parameters are  $U = 7t$ ,  $t' = -0.15t$  and  $\beta t = 15$ .

to the self-energy when the external electric field is applied (Eq. 3.28).

However, the formalism derived above is problematic as can be seen from the calculated current-current response function  $\chi(i\Omega_m)$  on the Matsubara frequency axis in the 8-site DCA approximation shown in Fig. 3.18. The parameters used in the calculation are  $U = 7t$ ,  $t' = -0.15t$  and  $\beta t = 15$ . We see that the kinetic energy which can be estimated from  $-\chi(0)$  has a weak doping dependence away from half-filling, with a suspicious value at half-filling that is substantially greater in magnitude than the values in doped samples and is also greater than the kinetic energy one would expect from the familiar f-sum rule ( $\sim 0.432$ ) [Millis (2004)]:

$$K = 2 \sum_a \int_{-\infty}^{\infty} \frac{d\omega}{\pi} \int^a \frac{d^2k}{(2\pi)^2} f(\omega) \frac{\partial^2 \varepsilon_k}{\partial k_x^2} \text{Im} G_a(k, \omega). \quad (3.50)$$

The violation of the f-sum rule was due to the formulation of the source term as in

Eq. 3.49 which leads to a non-zero value at  $\Omega = 0$ . And our analysis shows that the substantial difference between the doped and undoped cases can be traced back to the fact that at half-filling the magnitude of the changes to the self-energy  $\Sigma^1$  is much larger than that when doped, which requires more thought. We also note that the low frequency current-current response function  $\chi(i\Omega_m)$  at the lightly doped case ( $x = 0.048$ ) is non-monotonic and deviates from the linear form expected in the conductivity for a metallic system. We believe that these are due to the defects in the formalism, which is still under investigation.

### 3.6 Summary

To summarize, we have developed a new method for treating the vertex corrections which are essential to obtain physically reasonable results in interacting electron systems, creating new opportunities for a broad understanding of the physics of correlated electron compounds. The theory reproduces the “two-magnon” peak characteristic of the Raman  $B_{1g}$  response of high- $T_c$  copper oxide superconductors. The persistence of the “two-magnon” peak on doped compounds implies the presence of short-range antiferromagnetic correlations over a wide range of doping levels. The vertex correction produces an abnormal low frequency peak in Raman  $B_{2g}$  scattering calculation which requires more investigation. The isotropic scattering properties in the high doping “isotropic Fermi liquid” region leads to similar structure in the Raman  $B_{1g}$  and  $B_{2g}$  scattering spectra. We also presented theoretically consistent calculations of the optical conductivity in the 4-site DCA implementation of cluster dynamical mean-field theory. The calculated results bear a great similarity to the conductivity observed in the cuprates.

The complications due to the momentum space discontinuity make the calculation of the vertex correction for the optics more difficult, which may lead to an additional

source term as in Eq. 3.13 for a general two-particle response function. Investigation in this direction is in progress. The 16-site cluster was studied in Gull et al. (2010) for the doping-driving metal-insulator transition, which provides a finer resolution for the self-energy in the momentum space. A more careful consideration of the cluster dependence of the “two-magnon” peak in Raman  $B_{1g}$  scattering is also of great interest. The recent algorithmic improvements enable the numerical study of the two dimensional Hubbard model at extremely low temperatures. An important direction of the future work is the calculation of the Raman scattering spectra in the superconducting state.

# Chapter 4

## Pseudogap in Cuprates

### 4.1 Overview

In this chapter we consider the pseudogap observed in cuprate superconductors above superconducting temperature. We shall start with a brief discussion on background in Sec. 4.2. In Sec. 4.3 we present the model and the dynamical mean-field and analytic continuation methods we use to solve it. In Sec. 4.4 we show results for the electron spectral function and in Sec. 4.5 the interplane conductivity. Sec. 4.6 presents our results for the Raman scattering intensity and Sec. 4.7 the in-plane conductivity. Sec. 4.8 shows the electron self-energy in the different momentum sectors, confirming the conjecture that the gap arises from an orbitally selective Mott transition and demonstrating that the model reproduces key aspects of the momentum selectivity in the approach to the Mott transition. Sec. 4.9 is a summary and conclusion. This chapter follows [Lin et al. \(2010\)](#).

### 4.2 Introduction

The “pseudogap”, a temperature and carrier concentration dependent suppression of the many-body density of states of hole-doped high temperature copper-oxide superconductors which is visible at temperatures well above the superconducting

transition temperature, is one of the enduring mysteries of the field. The pseudogap was first inferred from measurements of spin-lattice relaxation times [Warren et al. (1989)] and Knight shifts [Alloul et al. (1989)]; additional evidence rapidly accumulated from measurements of in-plane resistivity [Ito et al. (1993)], photoemission spectra [Loeser et al. (1996); Ding et al. (1996)], the interplane (c-axis) conductivity [Homes et al. (1993); Tajima et al. (1997)], Raman scattering [Nemetschek et al. (1997); Chen et al. (1997)] and tunneling [Renner et al. (1998)] and measurements of the electronic density of states. On the other hand, the pseudogap does not lead to a significant suppression of low frequency spectral weight in the in-plane conductivity [Orenstein et al. (1990)], although structure in the conductivity and in scattering rates inferred from the conductivity has been attributed to the pseudogap [Basov and Timusk (2005)]. The gap is most pronounced at low temperatures and low dopings. The data suggest that the gap magnitude decreases as doping increases, whereas with increasing temperature the gap magnitude does not decrease. Rather, the gap “fills in” as more and more states appear in the mid-gap region.

Photoemission measurements [Loeser et al. (1996); Ding et al. (1996); Damascelli et al. (2003)] indicate that the pseudogap is largest near the zone corner  $(0, \pi)/(\pi, 0)$  regions and vanishes at the zone-diagonal  $(\pm\pi/2, \pm\pi/2)$  regions. This momentum-space structure of the pseudogap is one aspect of the more general phenomenon of momentum-space differentiation that characterizes the doping-dependent metal insulator transition in the high- $T_c$  materials.

Schmalian, Pines and Stokjovic [Schmalian et al. (1998)] argued that one should distinguish between a “weak” and “strong” pseudogap. The weak pseudogap terminology refers to relatively low energy phenomena affecting states within a few tens of meV of the Fermi surface while the “strong” pseudogap is a suppression of density of states which may exist over a relatively wide energy range.

The physical interpretation of the pseudogap remains controversial. One possibil-

ity is that it is associated with an actual thermodynamic transition to a phase with a definite long ranged order. Possibilities which have been proposed include magnetic order, perhaps of “stripe” or “nematic” density wave form [Kivelson et al. (1998)] and an orbital current phase [Varma (2006)]. Experimental evidence has appeared supporting each of these possibilities [Tranquada et al. (1995); Fauqué et al. (2006)] but the interpretations remain controversial [Sonier et al. (2009)].

An alternative possibility is that the pseudogap is a consequence of long but not infinite ranged order of spin density wave [Millis and Monien (1993); Vilk and Tremblay (1997); Schmalian et al. (1998); Aranov et al. (2001)], superconducting [Emery and Kivelson (1995); Wang et al. (2002)] or RVB [Kotliar and Liu (1988); Lee and Nagaosa (1992); Altshuler et al. (1996)] type. One loop [Lee et al. (1973)] and more sophisticated [Vilk and Tremblay (1997); Schmalian et al. (1998); Aranov et al. (2001)] calculations provide a relation between quasi-long-ranged order and pseudogaps, while slave-boson-based mean-field methods [Kotliar and Liu (1988); Lee and Nagaosa (1992); Altshuler et al. (1996)] provide a different mechanism for (pseudo)gap formation. However, these methods are based on uncontrolled analytical approximations. Models of quasi one dimensional “ladder” compounds can be studied in a controlled manner and are known to exhibit gapped phases with no long ranged order [Elbio Dagotto (1996)], however despite intriguing qualitative similarities the relation of “ladder” calculations to the two dimensional physics relevant to the cuprates remains unclear. There is a clear need for studies based on methods which are applicable in two dimensions and at intermediate to strong couplings and which are not based on a particular assumption about the type of relevant correlations.

One such approach is provided by “cluster” dynamical mean-field methods [Maier et al. (2005)]. These techniques are based on a coarse discretization of the momentum dependence of the electron self-energy but permit a numerically unbiased solution of the resulting model. Important early work showed that the cluster dynamical

mean-field approximation produced features reminiscent of the pseudogap including suppression of the density of states in the  $(0, \pi)$  region of the zone [Huscroft et al. (2001)] and “Fermi arcs” which are at least qualitatively consistent with photoemission experiments [Parcollet et al. (2004); Civelli et al. (2005); Kyung et al. (2006); Stanescu and Kotliar (2006)]. Subsequently many cluster dynamical mean-field theory (DMFT) studies of the pseudogap have appeared [Macridin et al. (2006); Zhang and Imada (2007); Civelli et al. (2008); Gull et al. (2008b); Park et al. (2008); Ferrero et al. (2009b,a); Civelli (2009); Liebsch and Tong (2009); Sakai et al. (2009); Sordi et al. (2010); Sakai et al. (2010)].

Studies to date are mainly of two sorts: large-cluster studies of one doping and temperature and more comprehensive studies of smaller (two and four site) clusters. An important large cluster study is the work of Macridin et al. (2006), which considered a 16 site cluster at  $U = 8t$  at a doping of 5% and an inverse temperature  $\beta = 8/t$  and showed from analytical continuation of the electron spectral function that a  $(0, \pi)$  pseudogap existed at this doping. The smaller-cluster studies have been based on two and four site clusters for which the computational burden is much less, permitting systematic examinations of a wider range of parameter space [Civelli et al. (2005); Kyung et al. (2006); Gull et al. (2008b); Park et al. (2008); Ferrero et al. (2009b); Civelli (2009); Zhang and Imada (2007); Liebsch and Tong (2009); Sakai et al. (2009); Sordi et al. (2010); Sakai et al. (2010)]. However these smaller clusters do not allow direct comparison of zone-diagonal and zone-face regions of momentum space. In addition, many of the more systematic small cluster based analyses employed interpolation schemes to construct a representation of the electron self-energy throughout the Brillouin zone. The reconstructions are based on data corresponding to the  $(0, 0)$ ,  $(\pi, \pi)$  and, for the four-site clusters,  $(0, \pi)/(\pi, 0)$  momentum points [Civelli et al. (2005); Kyung et al. (2006); Stanescu and Kotliar (2006)] and the physical interpretation is problematic especially because information related to the physically

important  $(\pm\pi/2, \pm\pi/2)$  momentum space regions is inferred from measurements at  $(0, 0)$ ,  $(\pi, \pi)$  and  $(0, \pi)/(\pi, 0)$  where the physics is presumably different. However, an interesting recent paper by Ferrero *et al.* [Ferrero *et al.* (2009a, 2010)] introduced a two-site cluster with a new momentum space partitioning which clearly separated nodal and antinodal regions.

The work reported here builds on recent studies of the 8-site cluster [Werner *et al.* (2009); Gull *et al.* (2009)] shown in Fig. 4.1. The larger size of this cluster provides a more refined momentum resolution and in particular gives independent access to the zone-face and zone-diagonal regions of the Fermi surface. However the size is small enough that studies of wide regions of parameter space are computationally feasible. Previous work has revealed that the doping-driven Mott transition is momentum-space-selective, with a gap opening first in the zone corner  $(0, \pi)/(\pi, 0)$  regions of the Brillouin zone while the zone-diagonal  $(\pm\pi/2, \pm\pi/2)$  regions remain ungapped until the carrier concentration reaches half filling. The previous work focused on quantities defined directly on the Matsubara axis. In this chapter we use analytical continuation techniques to examine the consequences of the momentum-space-selective transitions for observables including the electron spectral function and self-energy, the interplane and in-plane conductivity, and the Raman scattering intensity. Our results strongly suggest that even in the absence of long ranged or quasi-long-ranged order, the Hubbard model at intermediate couplings contains the essential physics of the “strong” pseudogap.

### 4.3 Model and Methods

We study the Hubbard model on a two dimensional lattice. The model is conveniently written in a mixed momentum-space/position-space representation as



$$H = \sum_{k\sigma} \varepsilon_k c_{k\sigma}^\dagger c_{k\sigma} + U \sum_i n_{i\uparrow} n_{i\downarrow} - \mu \sum_{i\sigma} n_{i\sigma}. \quad (4.1)$$

We take, as a reasonable representation of the band structure of high temperature superconductors,

$$\varepsilon_k = -2t (\cos k_x + \cos k_y) - 4t' \cos k_x \cos k_y \quad (4.2)$$

with  $t' = -0.15t$ . For comparison to data we note that a value generally accepted for high- $T_c$  superconductors is  $t \approx 0.35$  eV [Andersen et al. (1995)] while values of  $t'/t$  from  $-0.05$  to  $-0.3$  have been reported for different materials.

To solve the model we use the “dynamical cluster approximation” (DCA) [Hettler et al. (1998); Maier et al. (2005)]. The method is based on tiling the Brillouin zone into  $N$  equal-area non-overlapping tiles and approximating the electron self-energy  $\Sigma(k, \omega)$  as a piecewise constant function which may take different values in the different tiles. Labeling the tiles by center momentum  $K$  we have

$$\Sigma(k, \omega) = \Sigma_K(\omega); \quad k \in K. \quad (4.3)$$

The results we present were obtained using the 8-site momentum space partitioning shown in Fig. 4.1 and the “continuous-time auxiliary field” (CT-AUX) numerical method [Gull et al. (2008a)] as discussed in more detail in Werner et al. (2009) and Gull et al. (2009). Because the model is solved on the imaginary axis, an analytic continuation procedure is required to obtain real frequency information. Following Wang et al. (2009) we continue the electron self-energies using the Maximum Entropy technique [Jarrell and Gubernatis (1996)] and the “L-curve” method [Rabani et al. (2002)]. The covariance matrix of the self-energies is approximately diagonal and the continuation of the obtained real frequency spectra back to the imaginary axis is in

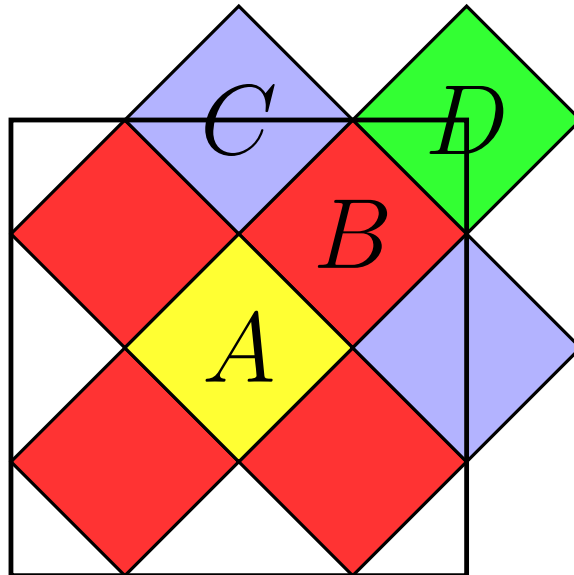


**Figure 4.1:** Brillouin zone partitioning associated with the 8-site cluster.

good agreement with the original data. Although uncertainties exist in the analytic continuation, our experience is that the near Fermi-surface structures are reliable.

The 8-site computation suffers from a fermionic sign problem which becomes worse with decreasing temperature and increasing doping and interaction strength. The need to scan a range of dopings and to obtain data of the precision required for reliable analytic continuations limited us to temperatures  $\geq t/20$  (corresponding roughly to 200 K for  $t = 0.35$  eV) and  $U = 7t$ . The  $U$ -value is smaller than the values  $U \sim 9t$  believed [Comanac et al. (2008)] to describe high temperature superconductors, but is large enough that (within the approximation we use) the half-filled state is a Mott insulator and hole-doping leads to a momentum-space-selective Mott transition.

Dynamical mean-field methods involve a drastic simplification of the momentum dependence of the electron self-energy. As Eq. (4.3) shows, the DCA method produces a piecewise constant self-energy which may be viewed as a discretization of the continuous momentum dependence of the exact solution. In many previous dynamical mean-field studies of the pseudogap an interpolation process [Civelli et al. (2005); Stanescu and Kotliar (2006)] was used to construct a self-energy with a continuous

momentum dependence, which was then used to produce figures to be compared to experiment. We prefer to avoid interpolations and instead work with analytic continuations of directly calculated quantities. We present results for

1. Sector-averaged electron spectral function

$$A_K(\omega) = -\frac{N_c}{\pi} \int_K \frac{d^2k}{(2\pi)^2} \text{Im} \left[ \frac{1}{\omega - \varepsilon_k + \mu - \Sigma_K(\omega)} \right] \quad (4.4)$$

with  $N_c = 8$  in our 8-site cluster.

2. Interplane or c-axis conductivity

$$\begin{aligned} \sigma_c(\Omega) = & 2 \sum_K \int_K \frac{d^2k}{(2\pi)^2} \int \frac{d\omega}{\pi} \frac{f(\omega) - f(\omega + \Omega)}{\Omega} \times \\ & t_\perp(k) \text{Im} G_K(k, \omega + \Omega) t_\perp(k) \text{Im} G_K(k, \omega) \end{aligned} \quad (4.5)$$

with  $t_\perp(k) = t_0(\cos k_x - \cos k_y)^2$ ,  $G_K(k, \omega) = [\omega - \varepsilon_k + \mu - \Sigma_K(\omega)]^{-1}$  and  $f(\omega)$  the Fermi-Dirac distribution. We used  $t_0 = 0.15$  eV  $\approx 0.43t$  [Andersen et al. (1995)] in the calculation.

3. Quasiparticle contribution to Raman scattering intensity

$$\begin{aligned} \chi''(\Omega) = & 2 \sum_K \int_K \frac{d^2k}{(2\pi)^2} \int \frac{d\omega}{\pi} [f(\omega) - f(\omega + \Omega)] \times \\ & \gamma_{ab} \text{Im} G_K(k, \omega + \Omega) \gamma_{ab} \text{Im} G_K(k, \omega). \end{aligned} \quad (4.6)$$

Two geometries are of interest:  $B_{1g}$ , where the matrix element is given by  $\gamma_{ab} = 1/2(\partial^2 \varepsilon_k / \partial k_x^2 - \partial^2 \varepsilon_k / \partial k_y^2)$  and  $B_{2g}$  where  $\gamma_{ab} = \partial^2 \varepsilon_k / \partial k_x \partial k_y$ . The  $B_{1g}$  geometry highlights the zone-face  $(0, \pi)/(\pi, 0)$  regions while the  $B_{2g}$  geometry highlights the zone-diagonals  $(\pm\pi/2, \pm\pi/2)$ . This matrix element is appropriate for non-resonant Raman scattering and is the simplest one which is consistent with the symmetry. In practice incident laser frequencies are often chosen to

take advantage of resonant enhancements arising from other degrees of freedom in the solid. These will change the absolute and relative magnitudes but not the symmetries of the vertices.

#### 4. Quasiparticle contribution to in-plane optical conductivity

$$\sigma(\Omega) = 2 \sum_K \int_K \frac{d^2k}{(2\pi)^2} \int \frac{d\omega}{\pi} \frac{f(\omega) - f(\omega + \Omega)}{\Omega} \times v_x \text{Im}G_K(k, \omega + \Omega) v_x \text{Im}G_K(k, \omega) \quad (4.7)$$

where  $v_x = \partial\varepsilon_k/\partial k_x$ . An approximate vertex correction [Lin et al. (2009)] was also incorporated.

#### 5. Real and imaginary parts of sector-dependent electron self-energy $\Sigma_K(\omega)$ .

Here  $\int_K$  denotes an integral over momenta lying in sector  $K$ . Note that for the Raman scattering and in-plane optical conductivities (unlike for the other quantities we have considered) a vertex correction contribution (which we have only partially calculated) is present. The full vertex correction calculation is currently in progress using methods outlined in our previous work [Lin et al. (2009)] but based on these results we expect the low frequency conductivity of primary interest here to have only a small vertex correction.

## 4.4 Electron Spectral Function

Fig. 4.2 shows the electron spectral function for the sector containing the  $(0, \pi)$  momentum (labeled  $C$  in Fig. 4.1) calculated at 0.05 hole doping for several temperatures. A “pseudogap” (reduction in density of states) is visible in the low energy region.

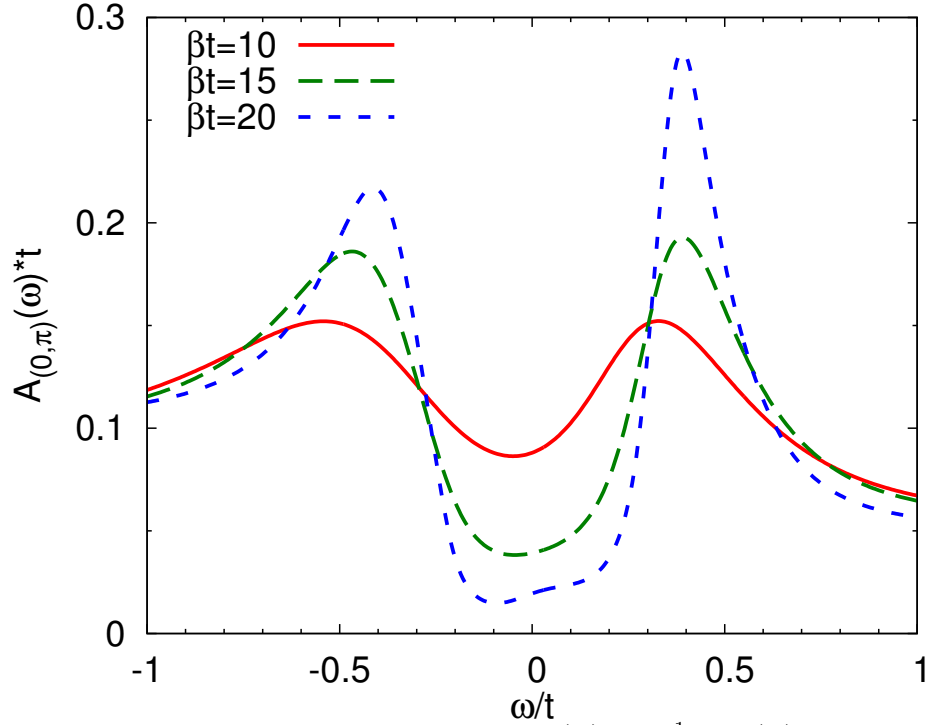


**Figure 4.2:** Many-body density of states  $A(\omega) = -\frac{1}{\pi}\text{Im}G(\omega)$  averaged over sector  $C$  containing the  $(0, \pi)$  point, calculated using 8-site DCA approximation at hole doping  $x = 0.05$  with  $U = 7t$  and inverse temperatures  $\beta = 1/T$  indicated.

We define the pseudogap magnitude  $E_{PG} = 2\Delta_{PG}$  as the peak to peak separation (for the  $x = 0.05$  case shown in Fig. 4.2  $E_{PG} \approx 0.8t \approx 0.3$  eV). The reduction in density of states is largest at the lowest temperature and for frequencies near  $\omega = 0$ . It appears that at this doping the low frequency density of states vanishes as  $T \rightarrow 0$ . As temperature is raised the gap “fills in”: the density of states inside the gap increases but the gap magnitude does not change appreciably. For temperatures greater than about  $0.2t$  the gap is no longer visible at this doping.

The upper panel of Fig. 4.3 shows the  $(0, \pi)$ -sector spectral function calculated at several different dopings. A decrease in gap magnitude with increasing doping is evident. For dopings larger than  $x = 0.11$  a gap is not visible at the temperatures  $T \geq t/20$  accessible to us although a weak feature in the  $x = 0.13$  curve suggests that

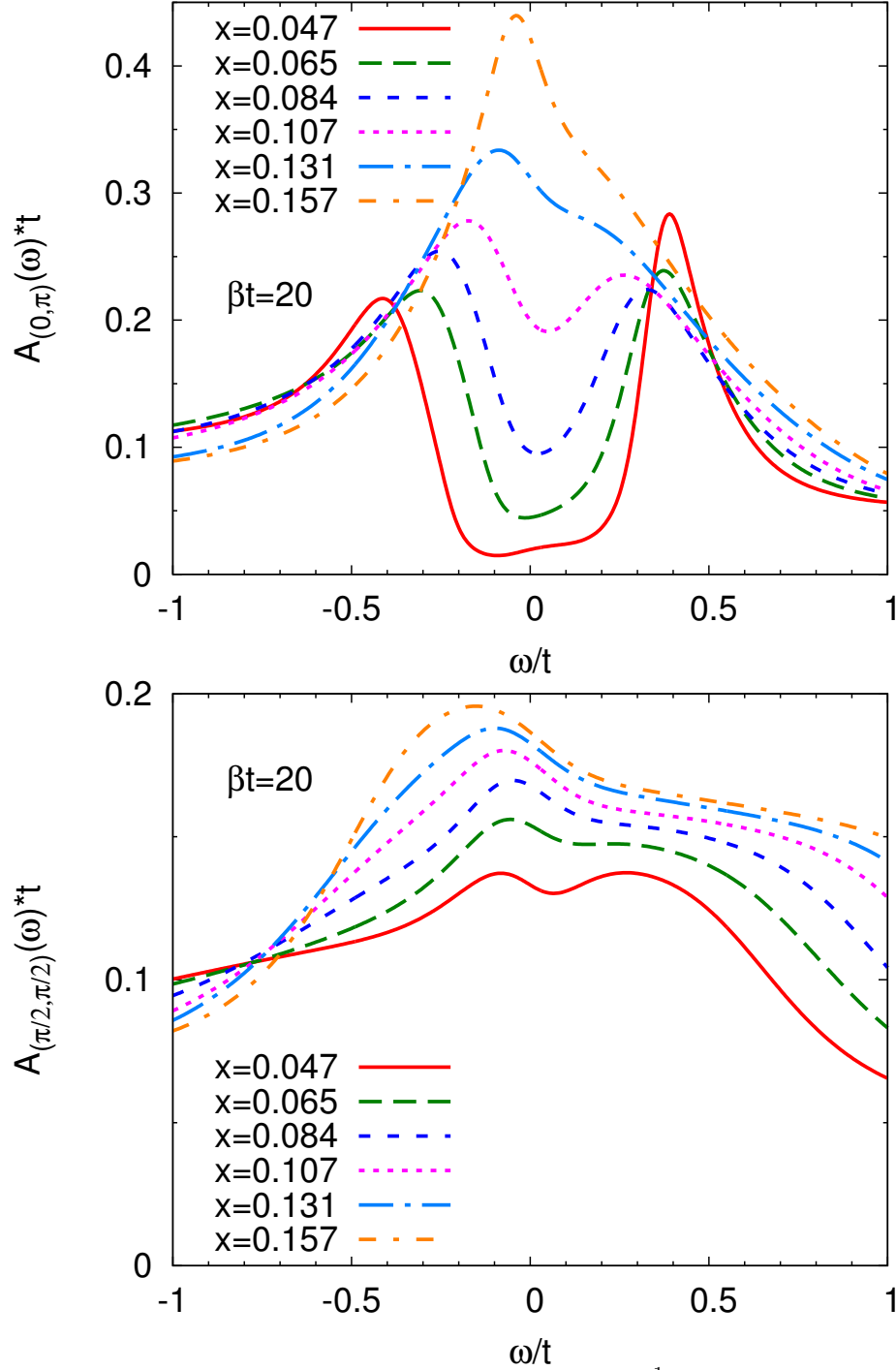


**Figure 4.3:** Many-body density of states  $A(\omega) = -\frac{1}{\pi}\text{Im}G(\omega)$  averaged over sector  $C$  containing the  $(0, \pi)$  point (upper panel) and sector  $B$  containing the  $(\pi/2, \pi/2)$  point (lower panel), calculated using the 8-site DCA approximation at hole dopings indicated with  $U = 7t$  and inverse temperature  $\beta = 20/t \approx 200$  K.

the gap is still present. However, certainly at  $x = 0.11$  and perhaps at  $x = 0.13$  the gap magnitude (as defined by the peak-to-peak distance in the spectral function) is not small. We therefore suspect that at least a reduction of density of states would be observed at higher dopings if we were able to perform the calculations at lower temperatures.

The lower panel of Fig. 4.3 shows the  $(\pi/2, \pi/2)$ -sector spectral function at the same dopings. At the smallest doping a weak suppression of low frequency density of states is evident but for most dopings this sector remains ungapped.

## 4.5 Interplane Conductivity

An important early indication of the presence of a charge-pseudogap was provided by measurements of the frequency dependence of the interplane conductivity [Homes et al. (1993)]. As can be seen from Eq. (4.5), in high- $T_c$  materials the matrix elements relevant to the interplane conductivity highlight the zone-face regions where the electron spectral function exhibits a gap (see upper panel in Fig. 4.3).

Fig. 4.4 shows the calculated temperature and doping dependence of the interplane conductivity. The pseudogap is visible as a temperature and doping dependent suppression of the low frequency interplane conductivity. The interplane conductivity is suppressed over a relatively wide frequency range; the suppression increases as the doping or temperature decreases, and the gap fills in but does not close as temperature is increased. The calculations also reveal a weak maximum in the conductivity at an energy just above the pseudogap. A somewhat broader version of this feature was observed by Yu et al. (2008). It is possible that the relative sharpness of the feature is an artifact related to our coarse-graining of momentum space, which might arise because the DCA approximation necessarily produces a gap that is piecewise continuous; and as is known from the familiar case of s-wave BCS superconductivity

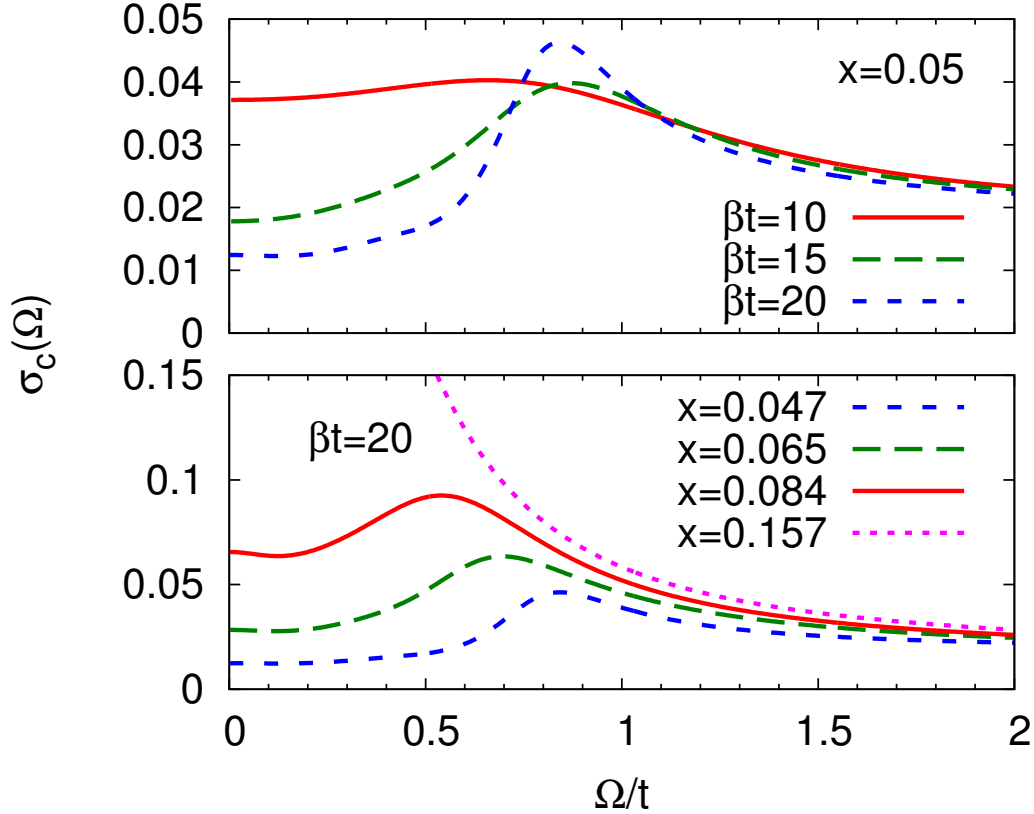


**Figure 4.4:** Upper panel: temperature dependence of interplane conductivity  $\sigma_c(\Omega)$  calculated from Eq. (4.5) for hole doping  $x = 0.05$  at inverse temperatures  $\beta = 1/T$  indicated. Lower panel (note change of vertical scale): doping dependence of interplane conductivity calculated at inverse temperature  $\beta = 20/t \approx 200$  K. At hole doping  $x = 0.16$ , the low frequency interplane conductivity is found to be approximately of Lorentzian form with dc value 0.65.

a momentum independent gap produces a peak. The results are reasonably consistent with experiment [Homes et al. (1993); Tajima et al. (1997); Basov and Timusk (2005); Yu et al. (2008)]. Yu et al. (2008) reports a high energy pseudogap of a magnitude consistent with what is found here. It is important to note that in the widely studied  $\text{YBa}_2\text{Cu}_3\text{O}_{6+x}$  material the interplay of strong local field effects (arising from the bilayer structure) and phonon effects produce complicated structures in the low frequency conductivity which are not represented in the present calculation [Dulić et al. (2001); Shah and Millis (2001); Yu et al. (2008)].



Conductivities may be characterized by “spectral weight”, the integrated area in some frequency range. The total spectral weight obeys an “f-sum” rule, which for the model studied here is

$$\int_0^\infty \frac{2d\omega}{\pi} \sigma_c(\omega) = 2 \sum_K \int_K \frac{d^2k}{(2\pi)^2} \int_{-\infty}^\infty \frac{d\omega}{\pi} f(\omega) t_\perp^2(k) \text{Im}[G^2(k, \omega)]. \quad (4.8)$$

We have verified that the spectral weight obtained from integration of the conductivity equals the spectral weight obtained from an evaluation of Eq. (4.8). The curves shown in Fig. 4.4 imply a temperature and doping-dependent decrease in low frequency spectral weight. We find that in the lower doping regions where the pseudogap is present, the spectral weight which is lost at low frequencies due to the formation of the gap is not fully restored at higher frequencies; thus the conductivity spectral weight decreases as the temperature or doping is decreased, whereas at higher doping the c-axis conductivity spectral weight increases as temperature is decreased. The calculated interplane conductivity is spread over a wide frequency range so the pseudogap-induced decrease of spectral weight is small relative to the total weight. The doping and temperature dependence of the c-axis spectral weight is given in Table 4.1.

**Table 4.1:** Integrated spectral weight of interplane optical conductivity obtained from Eq. (4.8) at different temperatures for several hole dopings.

x	$\beta t = 10$	$\beta t = 15$	$\beta t = 20$
0.05	0.111	0.105	0.102
0.07	0.125	0.119	0.116
0.08	0.142	0.138	0.134
0.16	0.207	0.223	0.231

Ferrero et al. (2010) reports interplane conductivity results obtained using a two-site cluster, a particular choice of self-energy periodization and a Padé continuation to compute  $\sigma_c$  for  $U/t = 10$  and  $t'/t = -0.3$ . The results are very similar to those

shown here but with slightly larger gaps and a much greater suppression of  $\sigma_c$  at sub-gap frequencies. Note that a factor of  $\pi t_0^2/(8t^2)$  is required to convert the results of Ferrero et al. (2010) to our units.

To conclude this section we note that the pseudogap effects are enhanced by the structure of the matrix element (which is the one widely used in the theoretical literature) which enhances the contribution of sector  $C$  relative to sector  $B$ . If a  $k$ -independent matrix element was used, the pseudogap effects would be less pronounced.

## 4.6 Raman Scattering Intensity

Raman scattering has provided important information about the cuprates [Devreux and Hackl (2007)]. It is a photon-in/photon-out process, and the polarizations of the electric field vectors of the incident and emitted photons may be adjusted to highlight transitions in different regions of momentum space. We consider here two scattering geometries:  $B_{1g}$  which highlights the anti-nodal region, and  $B_{2g}$  where the matrix element highlights the nodal region. The computation of the Raman intensity includes the quasiparticle contribution and the vertex correction as discussed in Chap. 3.

Fig. 4.5 shows the temperature dependence of the calculated Raman spectra in the two scattering geometries at one low doping and one high doping. At the higher doping the Raman response in each channel rises linearly to a weak maximum and then approximately saturates; the initial slope increases as  $T$  decreases in both channels. It is also interesting to note that the calculation reproduces the roughly frequency-independent high frequency behavior, which had previously been argued to be evidence for novel “marginal Fermi liquid” physics not contained in the Hubbard model [Varma et al. (1989)]. However, at the lower dopings the low frequency  $B_{1g}$  response

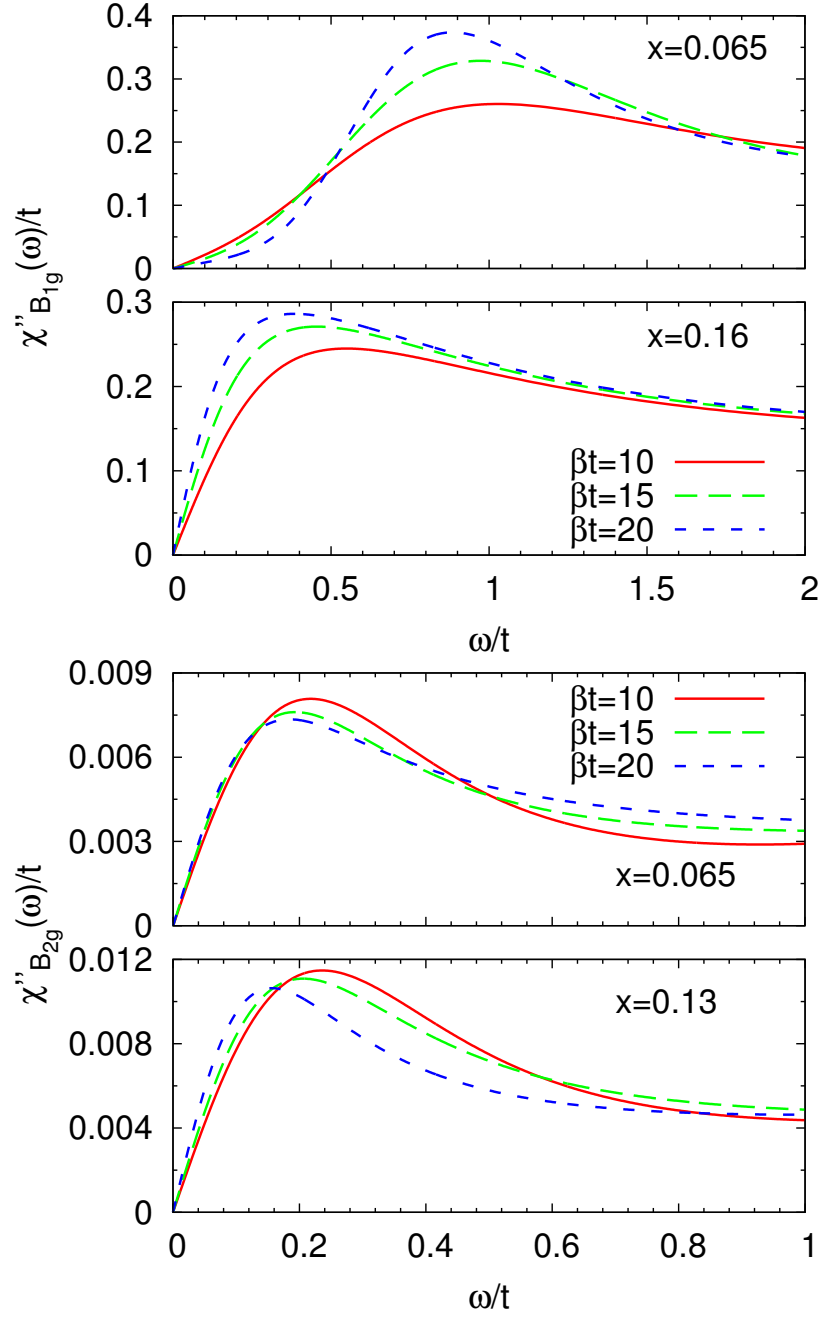


**Figure 4.5:** Temperature dependence of Raman scattering intensity  $\chi''(\Omega)$  calculated from Eq. (4.6) and the vertex correction for  $B_{1g}$  (upper panel) and  $B_{2g}$  (lower panel) scattering channels in 8-site DCA at hole doping at  $U = 7t$  and two different doping levels.

is progressively suppressed as  $T$  decreases, whereas the  $B_{2g}$  response has only weak  $T$  dependence.

The key features of the results presented in Fig. 4.5, namely an increase with increasing doping in the temperature dependence of the low frequency  $B_{2g}$  scattering intensity and a change in sign of the  $T$  dependence for the  $B_{1g}$  intensity along with the presence of a weak maximum at an energy which decreases with increasing doping are qualitatively consistent with data (see e.g. Fig. 42 and 43 of [Devereaux and Hackl \(2007\)](#)).

However, there are important quantitative differences. The calculated ratio of  $B_{1g}$  to  $B_{2g}$  is much greater than one which is very close to the reported experimental ratio. This difference presumably arises because the experiments employ a resonantly enhanced matrix element. Further, observed  $B_{2g}$  Raman spectra at low dopings have more  $T$  dependence than is found in our calculations. The onset coincides in temperature with other measures of the pseudogap, so we associate the phenomenon to the pseudogap.

Figs. 4.6 and 4.7 show the doping dependence of the Raman intensity at inverse temperature  $\beta t = 20$  corresponding to  $T \approx 200$  K. A strong increase in initial slope is evident in both channels. The rapid steepening of the initial slope in the  $B_{2g}$  channel is a consequence of the emergence of coherent quasiparticles in the zone-diagonal sector (see Sec. 4.8). The change in the  $B_{1g}$  channel arises from the doping dependence of the pseudogap which is mixed up with the effect of the “two-magnon” peak discussed in Chap. 3. The calculated behavior of the Raman intensity, including the difference in doping and temperature dependence between the two sectors and in particular the doping dependent suppression of the  $B_{1g}$  Raman spectra over a wide frequency range, is in reasonable agreement with measurements [[Katsufuji et al. \(1993\)](#); [Venturini et al. \(2002\)](#); [Hackl et al. \(2005\)](#); [Devereaux and Hackl \(2007\)](#)]. However, our calculated  $B_{2g}$  spectra exhibit a strong doping dependence which is not

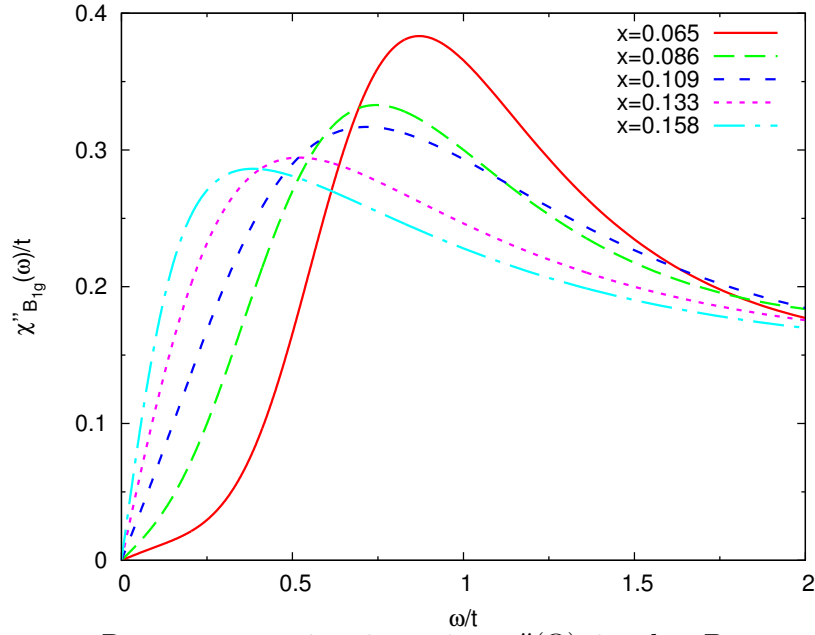


**Figure 4.6:** Raman scattering intensity  $\chi''(\Omega)$  in the  $B_{1g}$  geometry at different hole dopings as indicated with  $U = 7t$  and inverse temperature  $\beta = 20/t \approx 200$  K.

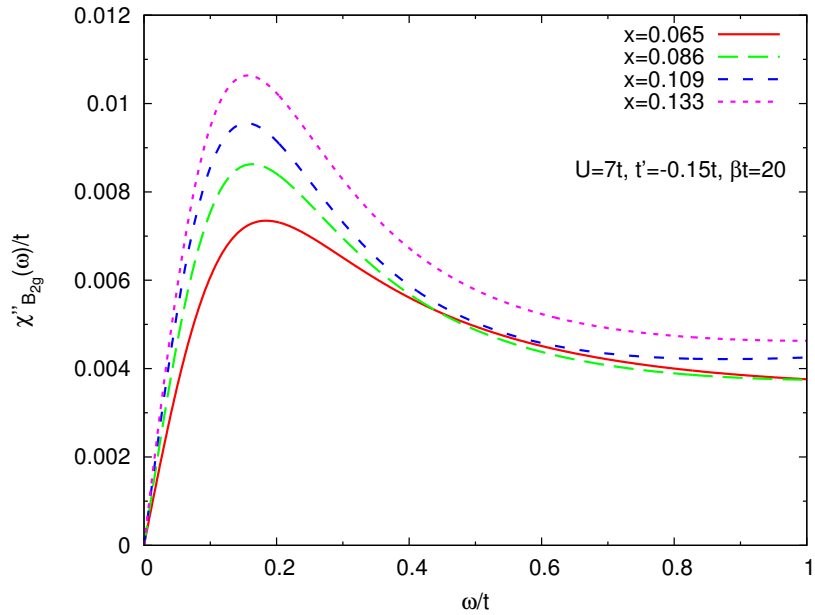


**Figure 4.7:** Raman scattering intensity  $\chi''(\Omega)$  in the  $B_{2g}$  geometry at different hole dopings as indicated with  $U = 7t$  and inverse temperature  $\beta = 20/t \approx 200$  K.

observed in recent experiments [Blanc et al. (2009)].

## 4.7 In-plane Conductivity

The optical conductivity  $\sigma(\Omega)$  of the high- $T_c$  cuprates has been an enduring mystery. The salient features of the data are a “Drude” peak centered at zero frequency, with a strongly temperature dependent spectral weight and half width, and a broad higher frequency continuum [Orenstein et al. (1990); Rotter et al. (1991); Basov and Timusk (2005)]. The strong doping dependence of the “Drude” peak has been taken as evidence of strong “Mott” correlations, while the broad higher frequency continuum has been interpreted in terms of scattering from spin fluctuations [Varma et al. (1989); Jaklič and Prelovšek (2000); Abanov et al. (2001); Schachinger et al. (2003)].

The computation of the in-plane conductivity involves a vertex correction [Lin et al. (2009)] which has not been fully calculated due to the difficulty discussed in Sec. 3.5.2. Here we only include the vertex correction arising from the self-energy discontinuities in momentum-space, while the contribution of additional dependence of the self-energy on the vector potential  $\vec{A}$  which arises from the change in mean-field function is neglected. The accuracy of this approximation is unknown, but we hope that the calculation would provide some qualitative insight into the physics of interest.

The main panel of Fig. 4.8 presents the calculated doping dependence of the real part of the in-plane conductivity. Our results exhibit strong similarities to experimental data, including, at low frequencies, a growth of the “Drude” peak with doping, and a weakly frequency and doping-dependent “mid-infrared” conductivity with a magnitude comparable to the measured value  $\sim 5 - 700 \Omega^{-1}\text{cm}^{-1}$  (note that to convert to the unit of  $\Omega^{-1}\text{cm}^{-1}$  commonly used in experiments, our results have to be

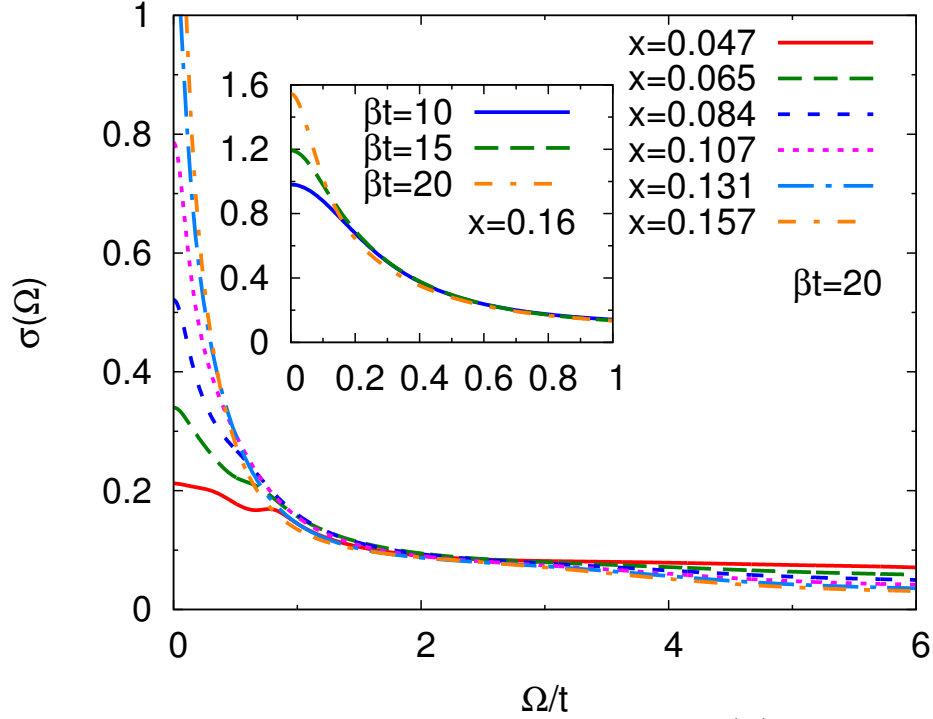


**Figure 4.8:** Main panel: in-plane optical conductivity  $\sigma(\Omega)$  calculated from Eq. (4.7) at  $U = 7t$  and inverse temperature  $\beta = 20/t \approx 200$  K for hole dopings indicated. Inset: temperature dependence of the low frequency in-plane optical conductivity for hole doping  $x = 0.16$ .

multiplied by a factor of about  $5 \times 10^3$ ). The inset shows that at higher dopings the “Drude” peak grows noticeably and sharpens slightly as temperature is decreased.

A particularly interesting issue is the lack of a clearcut effect of the pseudogap on the conductivity. A natural conjecture is that the conductivity is dominated by states near the zone-diagonal, which are not sensitive to the pseudogap. Fig. 4.9 presents a decomposition of the contributions of the different sectors to the measured conductivity which supports this conjecture. A pseudogap (the feature at  $\omega \sim t$ ) is present in the contribution of sector  $C$ , but the contribution of this sector to the measured conductivity is relatively small, so the feature is not evident in the full conductivity. The pseudogap feature is more pronounced in 4-site cluster calculations [Haule and Kotliar (2007); Chakraborty et al. (2008); Lin et al. (2009)] because the geometry of the 4-

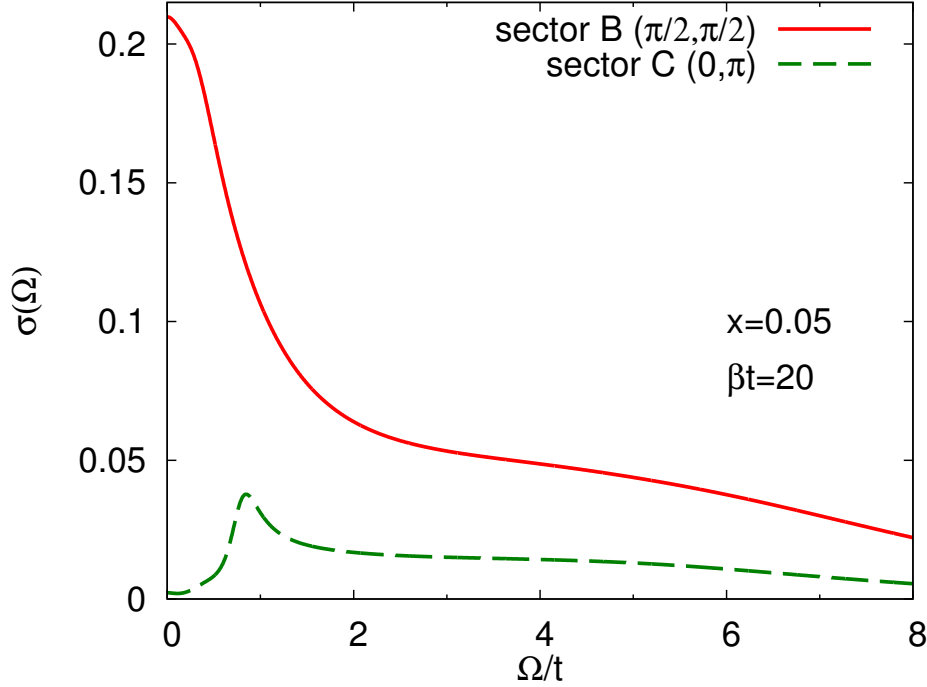


**Figure 4.9:** Contribution of different momentum sectors to calculated in-plane optical conductivity for  $U = 7t$  at doping  $x = 0.05$  and inverse temperature  $\beta = 20/t \approx 200$  K.

site cluster is such that the low frequency behavior is dominated by the  $(0, \pi)/(\pi, 0)$  sectors so that it does not capture the physics of the nodal quasi-particles. In the present 8-site calculation the nodal quasiparticle physics is represented by sector  $B$ , which is seen to give the dominant contribution to the conductivity.

**Table 4.2:** Integrated spectral weight of in-plane optical conductivity obtained by integrating calculated curves multiplied by a factor of  $2/\pi$  up to  $\Omega = 3t \approx 1$  eV at different temperatures for several hole dopings.

$x$	$\beta t = 10$	$\beta t = 15$	$\beta t = 20$
0.05	0.252	0.244	0.240
0.08	0.3141	0.3145	0.313
0.11	0.328	0.343	0.345
0.16	0.383	0.390	0.392

The doping [Uchida et al. (1991); Orenstein et al. (1990); Rotter et al. (1991); Comanac et al. (2008)] and temperature [Santander-Syro et al. (2003); Carbone et al.



(2006)] dependence of the optical spectral weight  $K = \int \frac{2d\omega}{\pi} \sigma(\omega)$  has been the subject of discussion in the literature. One ambiguity is the range over which the conductivity is to be integrated: setting the range too high leads to the inclusion of interband transitions which are believed to be irrelevant to the physics of high- $T_c$  materials while setting the range too low may mean that changes in the width of a low frequency peak may be mistaken for changes in area. Recent papers suggest that an upper cutoff of  $\sim 1$  eV is a reasonable compromise value [Millis et al. (2005); Carbone et al. (2006)]. A marked increase of spectral weight occurs as doping is increased (see Co-manac et al. (2008) for a summary of the data). The experimental consensus is that at all dopings the spectral weight increases weakly as temperature is decreased, and that the temperature dependence changes markedly as the temperature is decreased below the superconducting transition temperature. The doping dependence of the calculated spectral weight over the range  $\Omega < 3t \sim 1$  eV (shown in Table 4.2) is reasonably consistent with the data although we find that at lower dopings  $x = 0.08, 0.05$  the temperature dependence flattens. A weak temperature dependence is seen in the spectral weights integrated up to  $3t \approx 1$  eV. The sign of the temperature dependence changes with doping: increasing as  $T$  is decreased at high doping and decreasing as  $T$  decreases at low doping. It is tempting to relate this change in temperature dependence to a change in physics from Fermi-liquid-like at high doping to pseudogapped at low doping but the small magnitude of the effect and the possibility of temperature dependent changes in the functional form of the conductivity make an interpretation unclear. Calculations of a 4-site cluster approximation to the  $t - J$  model [Carbone et al. (2006)] (which is believed to reflect the low energy physics of the Hubbard model for  $U \geq 12t$ , larger than what we studied here) found a similar doping and temperature dependence.

The conductivity is sometimes expressed in terms of a frequency-dependent optical

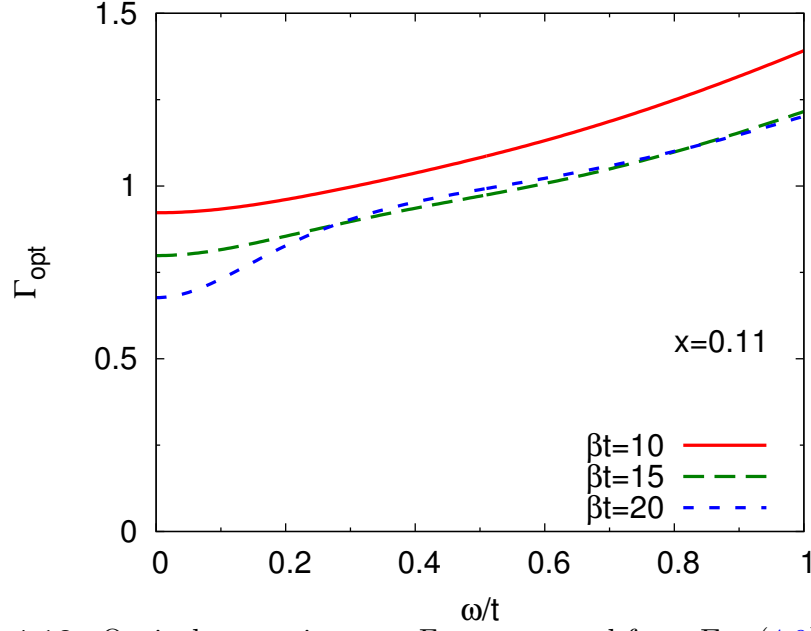


**Figure 4.10:** Optical scattering rate  $\Gamma_{\text{opt}}$  computed from Eq. (4.9) for hole doping  $x = 0.11$  and inverse temperatures  $\beta = 1/T$  indicated.

scattering rate  $\Gamma_{\text{opt}}$  related to the complex conductivity  $\tilde{\sigma} = \sigma_1(\omega) + i\sigma_2(\omega)$  via

$$\Gamma_{\text{opt}} = K \text{Re} \frac{1}{\tilde{\sigma}} \quad (4.9)$$

where  $\sigma_1$  is calculated from Eq. (4.7) and  $\sigma_2$  is obtained by the Kramers-Kronig transformation of  $\sigma_1$ . In underdoped cuprates at high temperature,  $\Gamma_{\text{opt}}$  is large and temperature dependent over a wide frequency range. As the temperature is decreased to the pseudogap scale the high frequency part loses its temperature dependence while at lower frequencies a temperature dependent suppression of  $\Gamma_{\text{opt}}$  appears [Timusk et al. (1995)]. Fig. 4.10 shows that this behavior is also found in our calculations.

We note that all the results presented in this section are obtained without the vertex correction arising from additional dependence of the self-energy on the vector potential  $\vec{A}$ .

## 4.8 Electron Self-Energy

Fig. 4.11 and 4.12 compare the temperature dependence of the imaginary part of the electron self-energy computed at doping  $x = 0.08$  and  $x = 0.16$  for the two momentum sectors containing the Fermi surface. At doping  $x = 0.08$  (see Fig. 4.11), we see that the  $(0, \pi)$  sector self-energy is characterized by a pole located near  $\omega = 0$  whereas no pole appears in the self-energy of the sector containing the zone-diagonal part. A near zero-energy pole in the self-energy is a characteristic of a Mott insulating state, confirming that the gap opening transition is indeed a sector selective Mott transition. As the temperature is decreased the pole grows in strength. The pole position at  $\omega \approx 0$  leads to the approximate particle-hole symmetry of the spectra. We also observe that at this doping the sector  $B$  (zone-diagonal) self-energy has only a weak temperature dependence at the temperatures accessible to us.

At doping  $x = 0.16$  (see Fig. 4.12), the self-energies in both sectors decrease with temperature and have a minimum centered at  $\omega \approx 0$ . In sector  $B$ , the self-energy has Fermi-liquid-like behavior which decreases rapidly and roughly linear in  $T$ . In sector  $C$ , the self-energy decreases more slowly. The difference in magnitude and doping dependence indicates that this doping regime is characterized by a large variation in scattering rate around the Fermi surface.

The lower panel of 4.14 shows the doping dependence of the sector  $C$  self-energy. A pole, gaining in strength as doping is decreased and centered at approximately zero frequency, is clearly visible for  $x \leq 0.11$ , while for  $x = 0.13$  and  $0.16$  there is no pole, only a weak modulation indicating a non-Fermi-liquid scattering rate. Whether this modulation would evolve into a pole as  $T \rightarrow 0$  is an interesting open question. [Liebsch and Tong \(2009\)](#) analyzed the self-energy pole structure in the  $(0, \pi)$  sector of a 4-site CDMFT study, finding a similar doping dependence of the pole strength. They reported a strong dependence of the pole position on doping; this variation is not found in the 8-site cluster studied here. For completeness we show in the upper

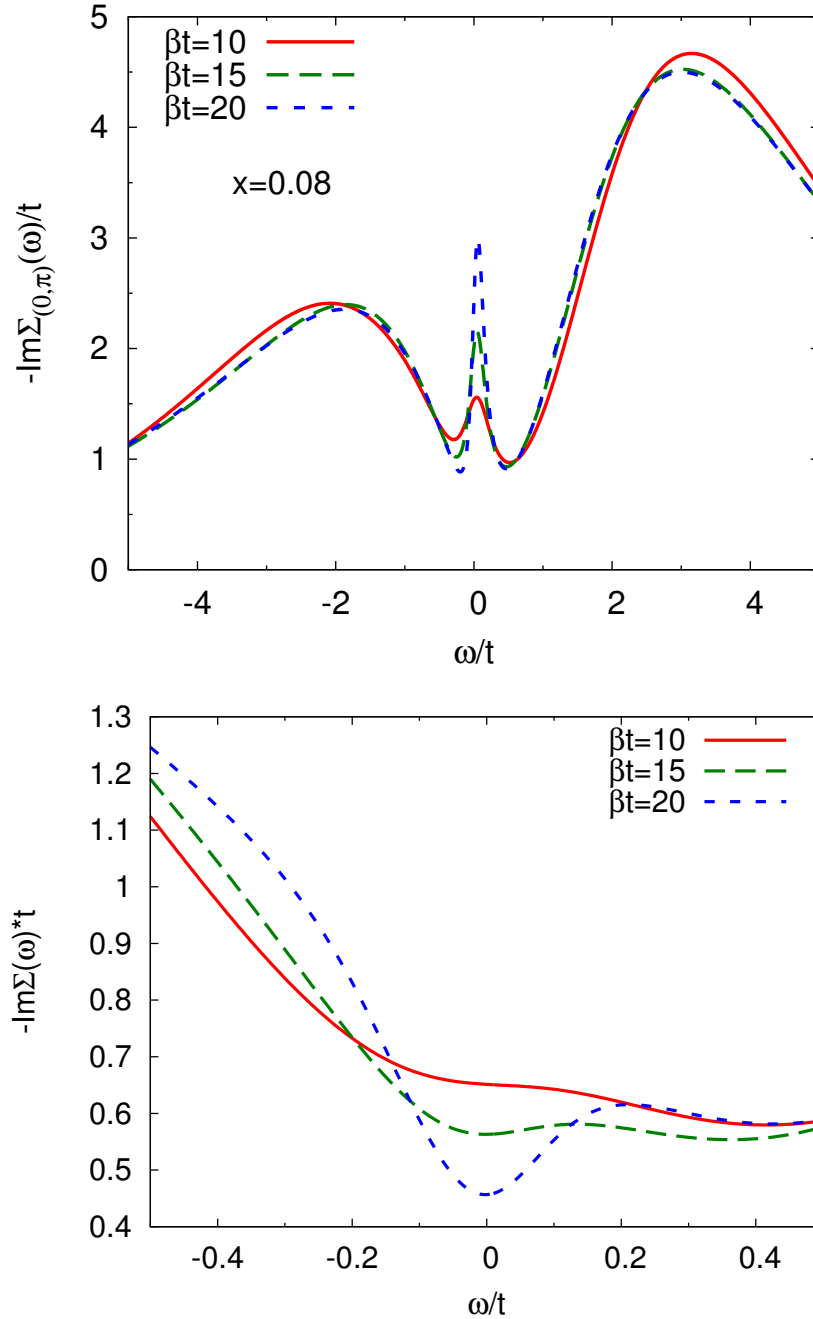


**Figure 4.11:** Imaginary part of electron self-energy computed at different temperatures for hole doping  $x = 0.08$  in  $(0, \pi)$ -sector (upper panel) and  $(\pi/2, \pi/2)$ -sector (lower panel).

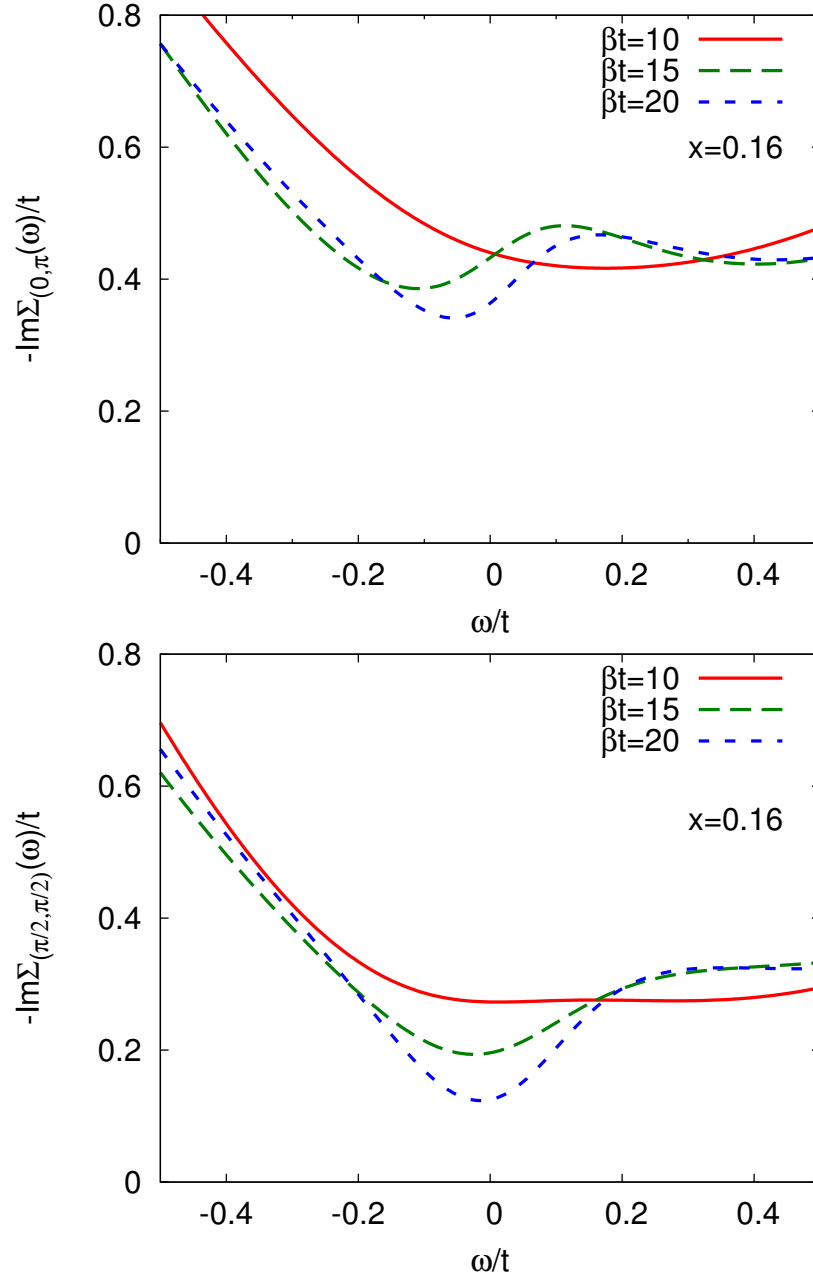


**Figure 4.12:** Imaginary part of electron self-energy computed at different temperatures for hole doping around 0.16 in  $(0, \pi)$ -sector (upper panel) and  $(\pi/2, \pi/2)$ -sector (lower panel).

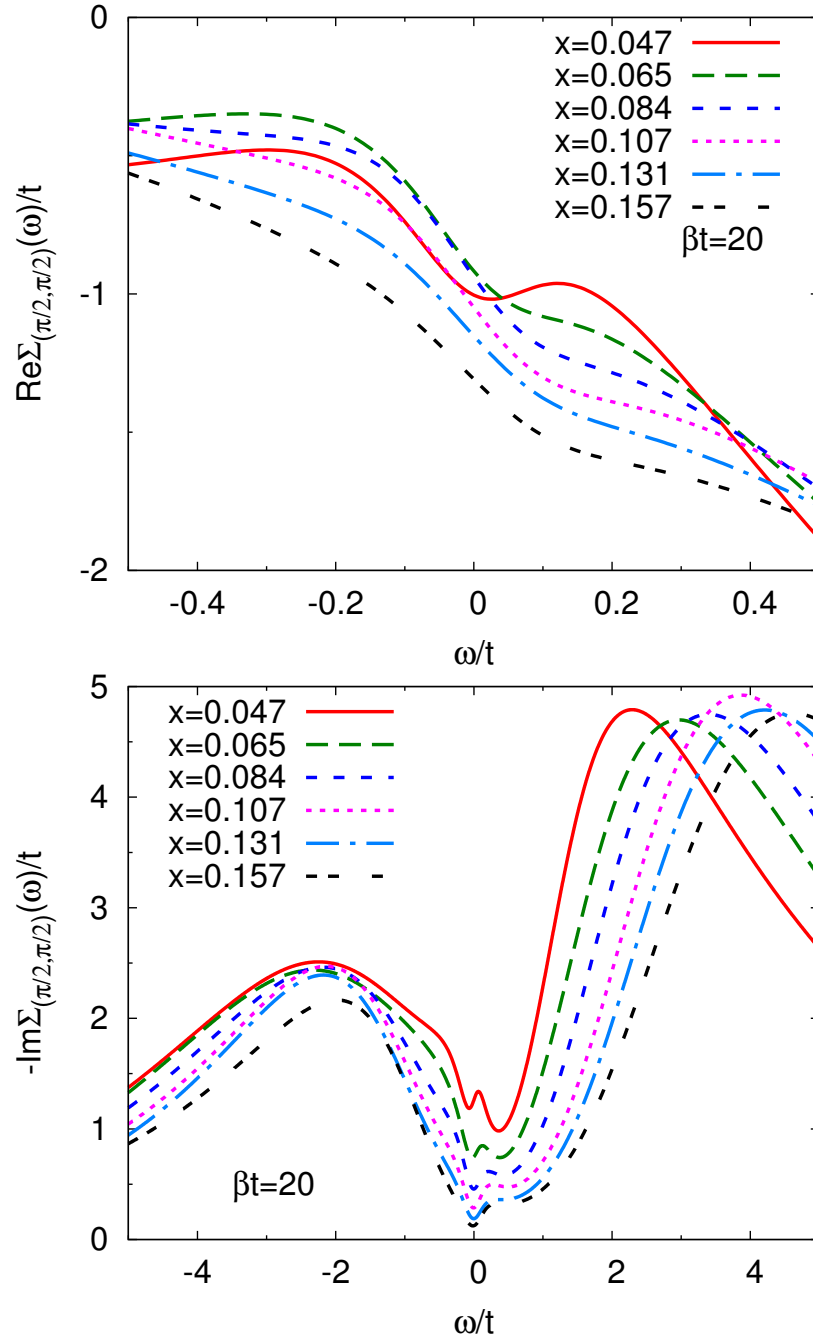


**Figure 4.13:** Real (upper panel) and imaginary (lower panel) part of the self-energy in sector  $B$  as a function of frequency, for dopings indicated.

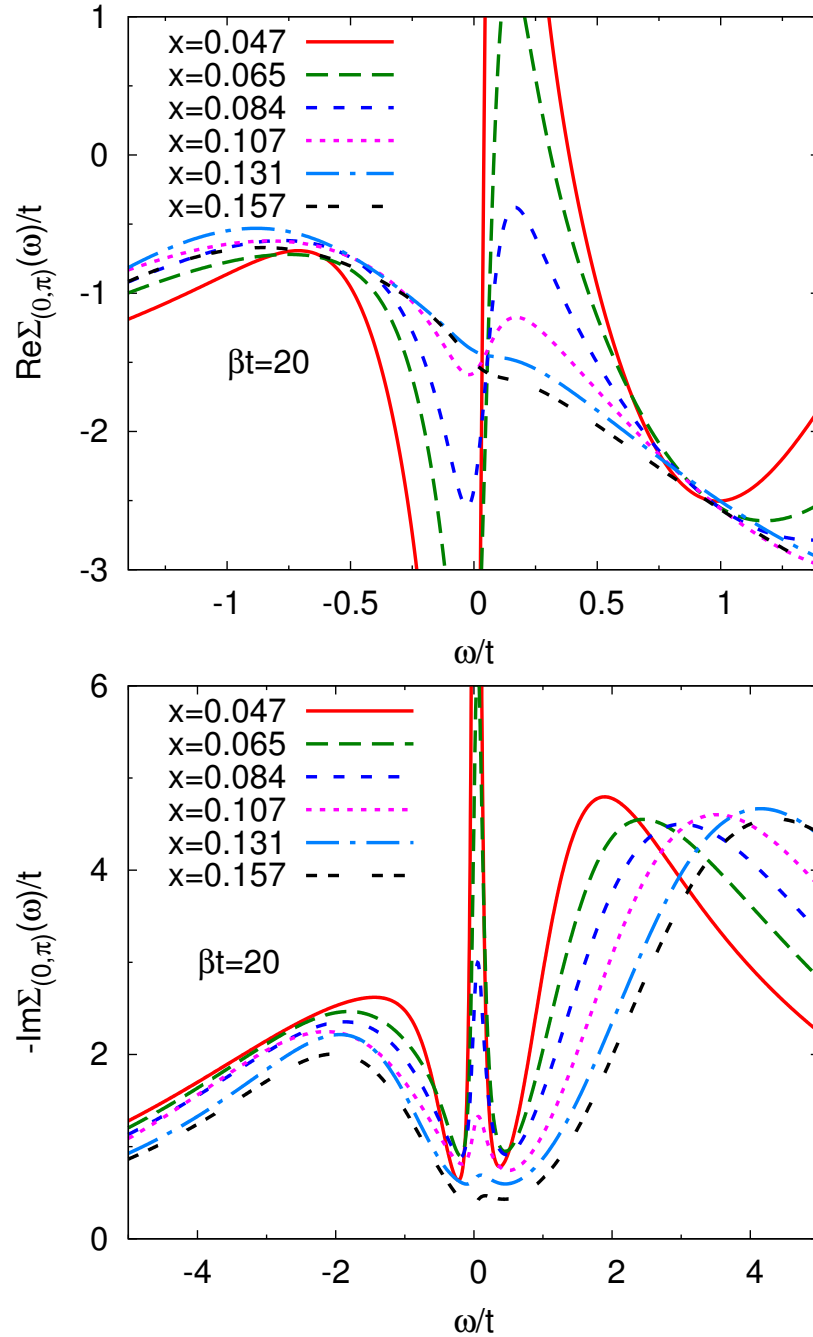


**Figure 4.14:** Real (upper panel) and imaginary (lower panel) part of electron self-energy computed for sector  $C$  containing the  $(0, \pi)$  point at inverse temperature  $\beta = 20/t \approx 200$  K for dopings indicated.

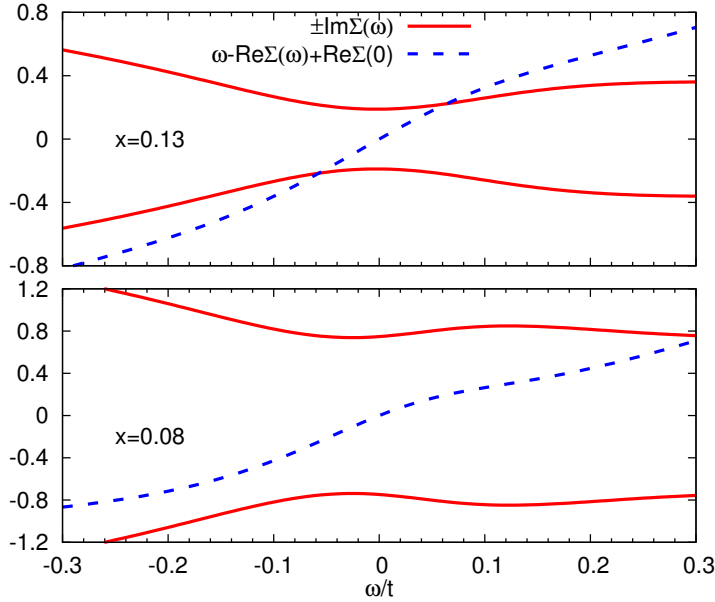


**Figure 4.15:** Imaginary part of the  $B$ -sector self-energy (solid line, red on-line) and real part of the  $B$ -sector self-energy (dashed line, blue on-line) at dopings  $x = 0.13$  (upper panel) and  $x = 0.08$  (lower panel), as a function of frequency. Note the different  $y$  axis scales.

panel of Fig. 4.14 the real part of the sector  $C$  self-energy. Fig. 4.13 presents the self-energy in sector  $B$  containing the  $(\pm\pi/2, \pm\pi/2)$  point.

An alternative characterization of electronic behavior is the quasiparticle residue  $Z = \left[1 - \frac{\partial \text{Re}\Sigma(\omega)}{\partial \omega} \Big|_{\omega=0}\right]^{-1}$ . Because within each sector the self-energy is momentum-independent,  $Z$  gives the renormalization of the Fermi velocity as  $v^* = Zv$ . This renormalization has physical significance if the self-energy is Fermi-liquid-like, meaning that the imaginary part is not too large and the real part is linear in frequency over a reasonable range about  $\omega = 0$ . We determine the boundaries of the Fermi-liquid regime by first observing that the real part of the self-energy  $\text{Re}\Sigma$  is linear in frequency over the range  $-\omega_L \leq \omega \leq \omega_H$ , and then comparing the magnitude of the imaginary part of the self-energy at zero frequency to the change of  $\omega - (\text{Re}\Sigma(\omega) - \text{Re}\Sigma(0))$  over the linear range. If the change  $(\omega_H - \text{Re}\Sigma(\omega_H)) - (\omega_L - \text{Re}\Sigma(\omega_L))$  is larger than



$-2\text{Im}\Sigma(\omega = 0)$  we identify the regime as Fermi-liquid-like.

We illustrate the determination of Fermi-liquid behavior as follows. Representative results for  $\text{Re}\Sigma(\omega)$  and  $\text{Im}\Sigma(\omega)$  are shown in Fig. 4.15. In a Fermi-liquid, the real part of the self-energy is linear in frequency (at low frequency), and the imaginary part is not too big. To formulate a quantitative criterion we first determine the range around  $\omega = 0$  over which  $\text{Re}\Sigma(\omega)$  is linear. This range is bounded at the lower end by a frequency  $\omega_L$  and at the higher end by  $\omega_H$ . For the  $x = 0.13$  data we have  $\omega_L = -0.08$ ,  $\omega_H = 0.08$ , for  $x = 0.08$  we have  $\omega_L = -0.08$ ,  $\omega_H = 0.02$ . Then we compute the change in quasiparticle energy  $(\omega_H - \Sigma(\omega_H)) - (\omega_L - \Sigma(\omega_L))$  (finding 0.56596 for  $x = 0.13$  and 0.42048 for  $x = 0.08$ ). Finally we compare the result to  $-2\text{Im}\Sigma(\omega = 0)$  which changes considerably between dopings. From this comparison we see that sector  $B$  at  $x = 0.13$  is well within the Fermi-liquid region while  $x = 0.08$  is on the border.

This condition is reasonably well satisfied for sector  $B$  for dopings  $x > 0.08$  (and marginally satisfied for  $x = 0.08$ ). Similarly sector  $C$  is found to be Fermi-liquid-like for dopings  $x = 0.18$  and greater, but for  $x = 0.06$  the self-energy in both sectors is far from Fermi-liquid-like and the quantity  $Z$  cannot be interpreted as a “quasiparticle weight”.

The solid points in the upper panel of Fig. 4.16 show the value of  $Z$  for the sector  $B$  containing the zone-diagonal point  $(\pi/2, \pi/2)$  and the sector  $C$  containing the zone-face point  $(0, \pi)$  for dopings for which the sectors are Fermi-liquid-like. The open symbols show the mathematically defined values of  $Z$  in the regime where it has no physical meaning because the regime is not Fermi-liquid-like. For dopings in the Fermi-liquid regime the  $Z$  in sector  $B$  is linear in  $x$  but extrapolates to a small non-zero value at  $x = 0$ . This is approximately but not exactly the behavior  $Z \sim x$  expected in a doped Mott insulator. The lower panel of Fig. 4.16 shows that the doping dependence of the low frequency optical conductivity weight is essentially the

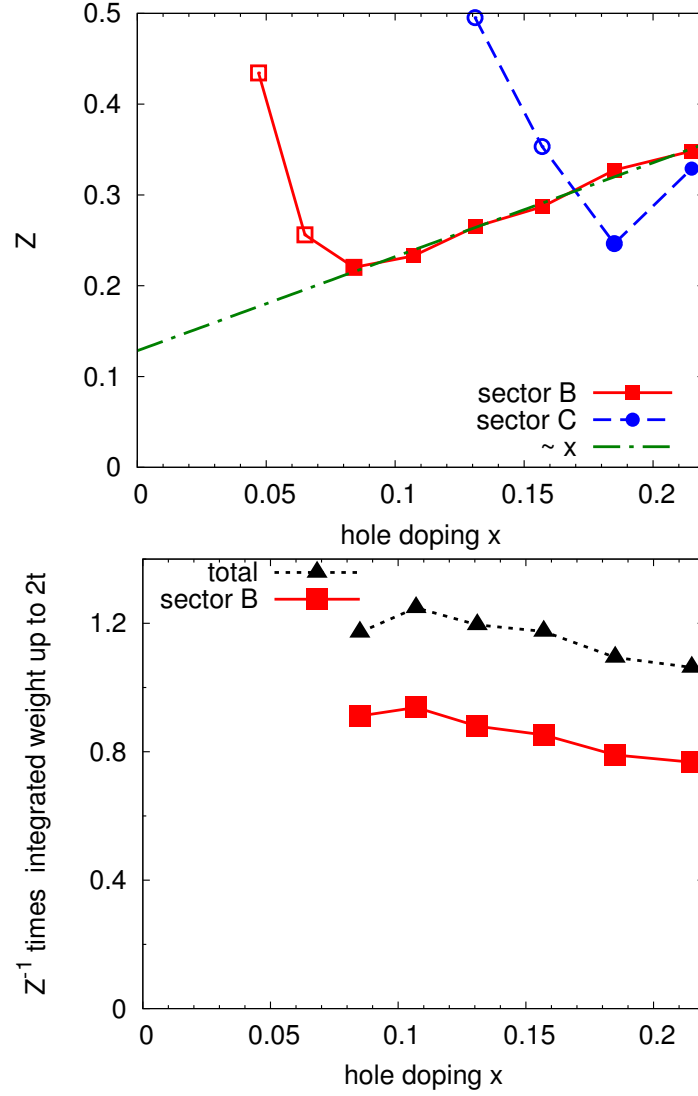


**Figure 4.16:** Upper panel: doping dependence of the quasiparticle residue  $Z$  calculated for sector  $B$  and sector  $C$  from analytically continued self-energies at inverse temperature  $\beta = 20/t \approx 200$  K. The filled symbols represent dopings  $x \geq 0.08$  for sector  $B$  and  $x \geq 0.18$  for sector  $C$  where the self-energy is Fermi-liquid-like as defined in the text. Open symbols are mathematically defined from our data but we believe are not physically meaningful because the scattering rate is too large. Lower panel: approximate proportionality of optical spectral weight and  $Z$ . Triangles (Squares): integral from 0 to  $\omega = 2t$  of calculated optical conductivities (sector  $B$  contribution to conductivity), divided by renormalization factor  $Z$  of sector  $B$ , plotted against doping  $x$ .

same as that of the nodal-sector  $Z$ .

## 4.9 Discussion

In the 8-site DCA approximation to the solution of the two dimensional Hubbard model, the doping-driven Mott transition occurs in an orbitally selective manner. As doping is reduced a pseudogap opens in the region of momentum space centered at  $(0, \pi)$  (and  $(\pi, 0)$ ) while the sector containing the zone-diagonal remains ungapped down to much lower dopings. In this paper we have explored some of the implications of this pseudogap for observables. We find that the gap is apparently tied to the Fermi level, fills in rather than closes with increasing temperature, and produces many of the qualitative features observed in experiment.

Fig. 4.17 plots the doping dependence of the pseudogap magnitude as defined from the peak to peak separation in the electron spectral function. As is seen in experiment [Hüfner et al. (2008)] the pseudogap magnitude is approximately linear in doping. The extrapolation to  $x = 0$  (see Fig. 4.17) gives  $\lim_{x \rightarrow 0} 2\Delta_{PG}(x) = 1.1t$  rather smaller than the  $x = 0$  sector  $C$  gap  $\sim 2.6t$  characteristic of the half filled insulator. The pseudogap is thus a new phenomenon, not a remnant of the gap occurring at half filling.

For  $x > 0.11$ , a gap is not visible in our calculated spectral functions; however, the linear extrapolation of the points in Fig. 4.17 indicates that for  $U = 7t$  studied here the critical value at which the gap would close is  $x \sim 0.17$ . One possible inference is that the temperatures  $T \geq t/20$  accessible to us are too high to enable the gap to be seen, and that calculations at lower temperatures would reveal a gap in the range  $0.11 < x < 0.17$ . Indeed, in experiment pseudogap effects are visible at dopings  $> 0.11$  but only at temperatures  $< 200$  K (see e.g. Damascelli et al. (2003), Fig. 63 or Yu et al. (2008)), i.e. less than the lowest temperature accessed in this study. Extending

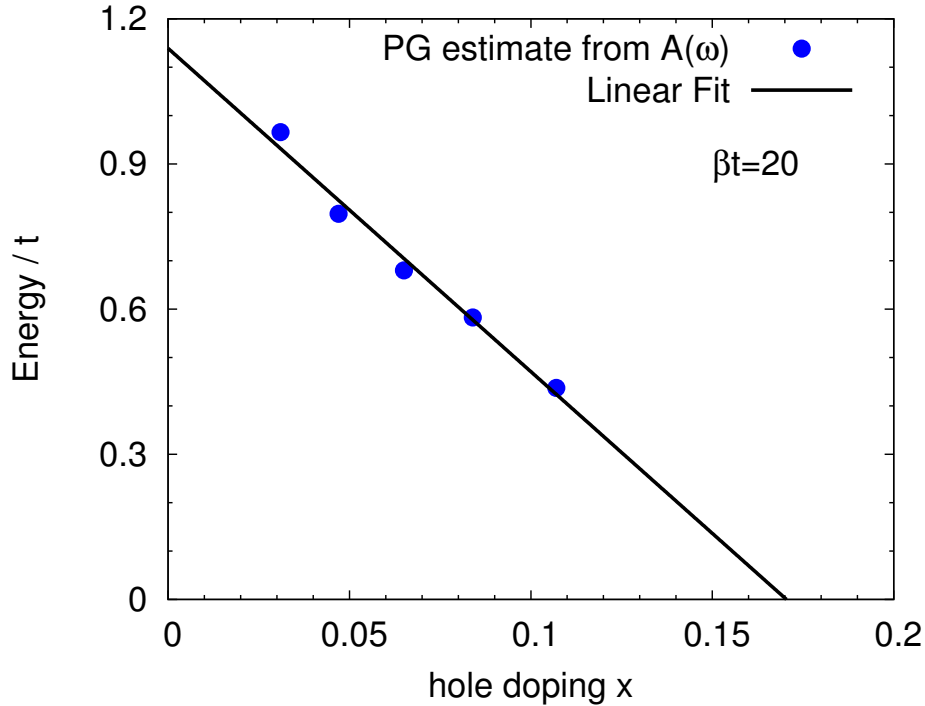


**Figure 4.17:** Points: pseudogap size determined from electron spectral function as a function of hole doping  $x$  for  $U = 7t$  and inverse temperature  $\beta = 20/t \approx 200$  K. Line: linear fit to results.

our results to lower temperatures is therefore of interest. It is also interesting to note that this larger doping is comparable with the value  $x = 0.15$  at which a quantum critical point was reported from analysis of the electron lifetime in a model with  $U = 6t$  [Vidhyadhiraja et al. (2009)].

Fig. 4.17 should however be interpreted with caution. At low dopings (see e. g. the  $x = 0.05$  results in Fig. 4.2) the low  $T$  limit of the spectral function exhibits a clear gap (region of vanishing density of states) and the peak to peak distance plotted in Fig. 4.17 corresponds well to the gap edge. As doping is increased the gap fills in and it is less clear whether as  $T \rightarrow 0$  the density of states would develop a true gap, or whether for  $x \geq 0.1$  the peaks represent the boundary of a region with reduced, but non-vanishing density of states. If the second possibility occurs then  $x \sim 0.1$  is a critical doping separating a low doping region where sector  $C$  is gapped

from an intermediate region where sector  $C$  has a non-zero, but possibly suppressed Fermi level density of states. This latter possibility is suggested by the imaginary axis analysis of previous papers [Werner et al. (2009); Gull et al. (2009)] which defined the critical doping for the orbital selective transition in terms of the chemical potential at which carriers were first added to sector  $C$ . This chemical potential value implies a critical  $x \sim 0.1$ .

A closely related question concerns the possible formation of Fermi arcs. A natural interpretation of the results is that as doping is decreased the pseudogap first forms at  $(0, \pi)/(\pi, 0)$  and with further decrease of doping an increasing portion of the Fermi surface is gapped, leaving a ‘‘Fermi arc’’ whose width is doping dependent. In this interpretation the sector  $B$  finding of a scattering rate which becomes large as doping is decreased would represent an average over a region (increasing as doping is decreased) where the Fermi surface is gapped and a Fermi arc region (decreasing as doping is decreased) with good quasiparticles. Analysis of this possibility requires a finer momentum resolution than is presently available to us.

While differences remain on the quantitative level between calculation and experiment and indeed between calculations performed on different clusters, the results indicate clearly that the Hubbard model at intermediate correlations and low dopings does exhibit a pseudogap with many of the features exhibited by the experimentally-defined high energy pseudogap. A transition to a phase with long ranged order is not necessary to produce the effect. The calculation does not reproduce many of the lower energy anomalies which may be associated with onset of significant superconducting, nematic, or orbital current order, perhaps because these are long wavelength effects beyond the scale provided by the cluster sizes or because they involve physics beyond the one-band model we are presently able to study.

# Chapter 5

## Quantum Chemistry

### 5.1 Overview

In this chapter we discuss the application of dynamical mean-field theory to quantum chemistry. Sec. 5.2 introduces the background and the motivation to our work. In Sec. 5.3 we present the formalism to apply dynamical mean-field concept to finite systems. Sec. 5.4 presents the performance of dynamical mean-field method in hydrogen clusters. In Sec. 5.5 we show the application to transition metal dioxide molecules. We summarize in Sec. 5.6. Part of this chapter follows [Lin et al. \(2011\)](#).

### 5.2 Introduction: Quantum Chemistry

Determining the ground state energy and dynamical properties of a system of  $N$  interacting electrons is a fundamental unsolved problem, crucial for both condensed matter physics and quantum chemistry. The properties of systems with “strong correlations”, those dominated by local interaction effects, have been proven particularly difficult to treat. Over the years many approaches have been developed, both in the domain of condensed matter physics and the domain of quantum chemistry [[Ceperley and Alder \(1980\)](#); [White \(1993\)](#); [Bartlett and Musiał \(2007\)](#); [Hohenberg and Kohn \(1964\)](#); [Kohn and Sham \(1965\)](#); [White and Martin \(1999\)](#); [Chan and](#)

Head-Gordon (2002); Barthel et al. (2009); Verstraete et al. (2008); Tsuchimochi and Scuseria (2009); Bajdich et al. (2010); Hybertsen and Louie (1986); Holzmann et al. (2009); Sharma et al. (2008); Anisimov et al. (1991)] but no one method has emerged as generally useful. In particular, for all but the smallest molecules the treatment of correlation effects in quantum chemistry (for example bond-breaking, or the energetics, dynamics and magnetic properties of transition metal clusters) remains a frontier research area.

In recent years the theoretical study of strongly correlated condensed matter systems has been revolutionized by the development of dynamical mean-field theory (DMFT), first in its single-site [Georges and Kotliar (1992); Georges et al. (1996)] and then in its cluster [Hettler et al. (2000); Kotliar et al. (2001); Maier et al. (2005)] forms. DMFT is a Green's function based method, in contrast to many of the quantum chemical methods which are wave function based, and is often presented in terms of an impurity self-consistently coupled to a non-interacting bath of states. To date, the main applications [Georges et al. (1996); Maier et al. (2005); Kotliar et al. (2006)] of DMFT have been to extended systems (typically periodic although an interesting recent application to a nanoscopic conductor should be noted [Jacob et al. (2010)]), characterized by a continuous density of states. Here, we show that DMFT can be used for finite systems, for which the "bath" is characterized by a discrete (even small) density of states. Application to a benchmark quantum chemical system ( $H_n$ , the  $n$ -hydrogen molecule in various configurations) discussed in Sec. 5.4 suggests the method may be useful for treating the strong correlation problems of quantum chemistry, which motivates the examination of the quantum impurity model representation of the transition metal dioxide molecules as discussed in Sec. 5.5.

### 5.3 Formalism

In the same way that density functional theory is derived from the Hohenberg-Kohn density functional [Kohn and Sham (1965)], a framework for many-body physics may be derived from the Luttinger-Ward functional  $\Phi_{\text{LW}}$  [Luttinger and Ward (1960)], which is a functional of the electron Green's function  $G$ , the interparticle interaction  $\hat{\mathbf{I}}$  and an external potential  $V(\mathbf{r})$ .  $G$  is defined in terms of the operator  $\psi_\sigma(\mathbf{r}, t)$  which annihilates an electron at position  $\mathbf{r}$  and time  $t$  as  $G_{\sigma\sigma'}(\mathbf{r}, \mathbf{r}', t - t') = \langle T_t [\psi_\sigma(\mathbf{r}, t), \psi_{\sigma'}^\dagger(\mathbf{r}', t')] \rangle$ . The appropriate  $G$  for a given external potential  $V$  satisfies  $\delta\Phi_{\text{LW}}/\delta G = 0$ . Not only the ground state energy and charge density, but also dynamical response functions can be obtained from  $\Phi_{\text{LW}}$  [Luttinger and Ward (1960)].

In analogy to density functional theory,  $\Phi_{\text{LW}}$  may be written as the sum of two terms: a “universal” term  $\Phi_{\text{LW}}^{\text{univ}}$  defined in terms of the sum of all vacuum to vacuum Feynman diagrams which has explicit dependence only on  $G$  and  $\hat{\mathbf{I}}$  (not on  $V$ ) and a material-specific term which depends explicitly on  $V$  and  $G$  but not  $\hat{\mathbf{I}}$ . DMFT is an exact extremization of an approximation to  $\Phi_{\text{LW}}^{\text{univ}}$ , in the same way that practical implementations of density functional theory are exact extremizations of approximations (such as the local density approximation) to the exact density functional.

In practice most correlated electron calculations proceed by reducing the full problem (which may be viewed as a matrix in the space spanned by the complete set of states  $\phi_a(\mathbf{r})$ ) to a “correlated” subspace spanned by a set of correlated states,  $\phi_a^{\text{corr}}(\mathbf{r})$ . One defines a correlated problem by retaining only the matrix elements of  $\mathbf{G}$  and  $\hat{\mathbf{I}}$  within the correlated subspace and writing a Luttinger Ward functional for the correlated degrees of freedom as

$$\Phi_{\text{LW}}^{\text{corr}} = \Phi_{\text{univ}}^{\text{corr}} - \text{Tr} \ln [\mathbf{G}_0^{-1} \mathbf{G}_{\text{corr}}] + \text{Tr} [\mathbf{G}_0^{-1} \mathbf{G}_{\text{corr}}] \quad (5.1)$$

$\mathbf{G}_0 \equiv (i\partial_t \mathbf{1} - \mathbf{H}_{\text{eff}}^{\text{corr}})^{-1}$  is the non-interacting Green's function defined in the usual



way in terms of the  $\phi_a$  and restricted to the subspace of correlated states while  $\Phi_{\text{univ}}^{\text{corr}}$  is formally defined as the sum of all vacuum to vacuum diagrams (with appropriate symmetry factors) involving  $\mathbf{G}_{\text{corr}}$  and interactions  $\hat{\mathbf{I}}^{\text{corr}}$ .

Within the active subspace we define the dynamical self-energy  $\Sigma = \mathbf{G}_0^{-1} - \mathbf{G}_{\text{corr}}^{-1}$ . If the active subspace contains  $M$  states (summed over atoms and orbitals),  $\Sigma$  may be represented as  $M(M+1)/2$  functions of frequency. The DMFT method approximates the self-energy as a sum of a much smaller number of functions. Different versions exist [Georges and Kotliar (1992); Hettler et al. (2000); Kotliar et al. (2001)], corresponding to different approximations to  $\Sigma$ . Each approximation to  $\Sigma$  implies an approximation to the Luttinger-Ward functional, which is such that the extremization may be carried out by solving a quantum impurity model with parameters fixed by a self-consistency condition. For specifics, see Georges et al. (1996); Maier et al. (2005). The results presented here were obtained with the ‘‘CDMFT’’ version [Kotliar et al. (2001)], which has a real space interpretation naturally suited to the non-translationally invariant problem posed by a molecule. The ‘‘DCA’’ formulation [Hettler et al. (2000)] is applicable to periodic configurations and extensions may exist to other cases.

In CDMFT one divides the full set of states into  $P$  cells, labelled by cell index  $J = 1 \dots P$ , with each cell containing some small number  $N$  of orbitals, labelled by an orbital index  $a = 1 \dots N$ . (Note that each cell may contain more than one atom.) The total number of correlated states is  $M = PN$ . The approximation is to retain only those components  $\Sigma^{(J_1 a_1)(J_2 a_2)}$  of  $\Sigma$  for which  $J_1 = J_2$  (i.e the two orbitals are in the same cell) and correspondingly only the intra-cell terms in  $\hat{\mathbf{I}}^{\text{corr}}$ . Defining the

resulting self-energy as  $\Sigma_{\text{CDMFT}}$ :

$$\Sigma_{\text{CDMFT}} = \begin{pmatrix} \Sigma_1 & \mathbf{0} & \dots & \mathbf{0} \\ \mathbf{0} & \Sigma_2 & \dots & \mathbf{0} \\ \vdots & \vdots & \ddots & \vdots \\ \mathbf{0} & \mathbf{0} & \dots & \Sigma_P \end{pmatrix}, \quad (5.2)$$

we obtain an approximation to the Green's function

$$\mathbf{G}_{\text{approx}} = (\mathbf{G}_0^{-1} - \Sigma_{\text{CDMFT}})^{-1}. \quad (5.3)$$

An approximate Luttinger-Ward functional is constructed by using  $\mathbf{G}_{\text{approx}}$  in the Tr and Trln terms in Eq. (5.1) and approximating the universal part as the sum of  $P$   $N$ -orbital quantum impurity models (different in each cell in non-periodic cases) defined in terms of a local Green's function and the intra-cell portions of the interaction  $\hat{\mathbf{I}}^{\text{corr}}$ . The  $\Sigma_{\text{CDMFT}}^J$  are found from the solution of the quantum impurity model for cell  $J$ . The stationarity condition on the approximate Luttinger-Ward functional is that the quantum impurity model Green's function for cell  $J$  equals the  $J - J$  component of  $\mathbf{G}_{\text{approx}}$  (Eq. (5.3)); enforcing this condition fixes the parameters of the quantum impurity model [Georges et al. (1996)]. The procedure becomes exact as cluster size  $N$  approaches system size  $M$  and provides a reasonable approximation for the small values of  $N$  which are computationally accessible [Koch et al. (2008)]. Nothing in this derivation requires that  $\mathbf{G}_0$  arise from a system with  $P = \infty$  and a continuous density of states.

We apply the procedure outlined above to the molecular system described by the

Hamiltonian:

$$H = \sum_{ij\sigma} t_{i,j} c_{i,\sigma}^\dagger c_{j,\sigma} + \frac{1}{2} \sum_{ij,\sigma,i',j',\sigma'} I_{i,j,i',j'} c_{i\sigma}^\dagger c_{i'\sigma'}^\dagger c_{j'\sigma'} c_{j\sigma} \quad (5.4)$$

$$H_{\text{tot}} = H + \frac{1}{2} \sum_{i \neq j} \frac{1}{|\mathbf{R}_i - \mathbf{R}_j|} \quad (5.5)$$

where

$$t_{ij} = \int d^3\mathbf{r} \psi(\mathbf{r} - \mathbf{R}_i) \left( -\frac{1}{2} \nabla^2 + V_{\text{ion}}(\mathbf{r}) \right) \psi(\mathbf{r} - \mathbf{R}_j), \quad (5.6)$$

$$I_{i,j,i',j'} = \int d^3\mathbf{r}_1 d^3\mathbf{r}_2 \frac{\psi^*(\mathbf{r}_1 - \mathbf{R}_i) \psi(\mathbf{r}_1 - \mathbf{R}_j) \psi^*(\mathbf{r}_2 - \mathbf{R}_{i'}) \psi(\mathbf{r}_2 - \mathbf{R}_{j'})}{|\mathbf{r}_1 - \mathbf{r}_2|}. \quad (5.7)$$

The one-electron part  $t_{i,j}$  describes the kinetic energy and the nuclear attraction energy, and the two-electron part  $I_{i,j,i',j'}$  describes the Coulomb interaction between electrons. The long range of the interaction means that all orbitals are coupled. The Hilbert space of the Hamiltonian described by Eq. 5.4 grows exponentially as the system size increases. Therefore in practice one can treat accurately only a subset of the interactions; the others must be treated by a more approximate method. After the correlated subspace is defined, we treat the interactions of interest in the correlated subspace dynamically by DMFT (or CDMFT), and use Hartree-Fock (HF) approximation to decouple the farther-neighbor interactions in the correlated subspace and the interactions in the uncorrelated subspace; other choices (e.g. density functional theory) are also possible [Kotliar et al. (2006)].

Fig. 5.1 shows the sketch of the DMFT method combined with the Hartree-Fock approximation. We start with an initial guess for the density matrix (for example, Hartree-Fock solutions), from which we construct the effective Hamiltonian by making Hartree-Fock approximations to relatively weak interactions. The effective Hamiltonian is solved by DMFT, producing the self-consistent solution (the electron self-energy  $\Sigma$ ). We then approximate the molecular Green's function using Eq. 5.3

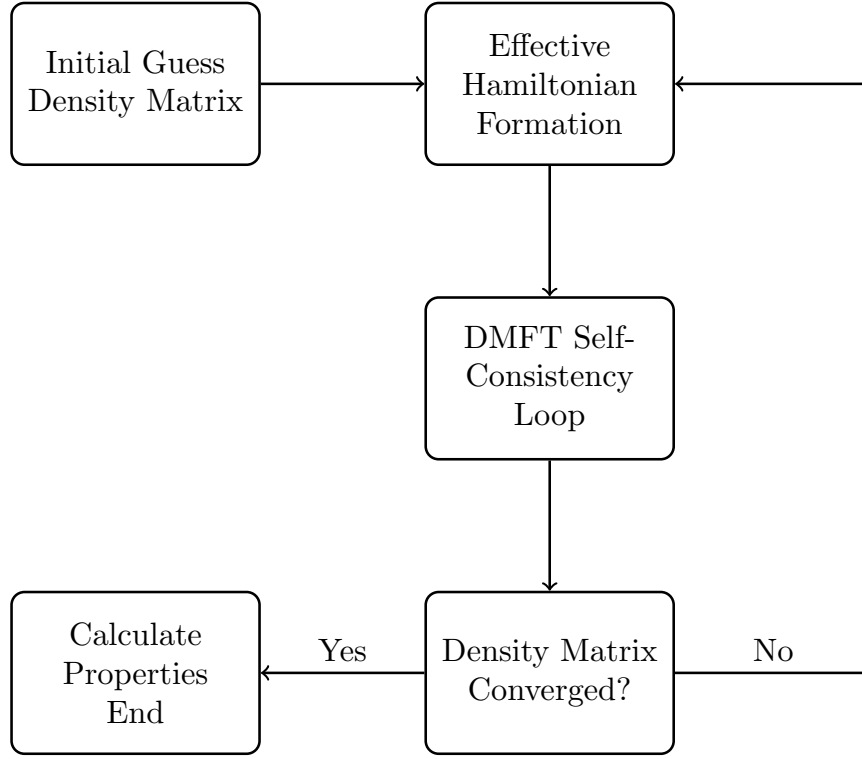


**Figure 5.1:** Sketch of the DMFT method combined with the Hartree-Fock approximation in finite systems.

and update the density matrix. The procedure is iterated until convergence. Finally the total energy can be evaluated via [Kotliar et al. (2001)]

$$\langle H \rangle = T \sum_{\sigma, \omega_n} \text{Tr} \left[ \mathbf{H}_{0, \sigma} \mathbf{G}_{\sigma} + \frac{1}{2} \boldsymbol{\Sigma}_{\sigma} \mathbf{G}_{\sigma} \right], \quad (5.8)$$

with  $\mathbf{H}_0$  the non-interacting one-electron Hamiltonian. The spectral function (density of states) can be obtained from the electron Green's function:

$$A(\omega) = -\frac{1}{\pi} \text{Im} G(\omega). \quad (5.9)$$

## 5.4 Hydrogen Cluster

We apply the CDMFT approximation to a standard quantum chemical reference system, the  $H_n$  molecule consisting of  $n$  hydrogen atoms which was recently studied by [Tsuchimochi and Scuseria \(2009\)](#) using a constrained-pairing mean-field theory (CPMFT). We present here results for  $H_n$  chains and rings with  $n = 6$  and  $n = 50$ , as well as the  $H_4$  tetrahedron. By chain we mean a linear arrangement of atoms with open boundary conditions and interatomic spacing  $R$  and by ring we mean a circular arrangement with chord distance  $R$  between nearest neighbor atoms. We follow [Tsuchimochi and Scuseria \(2009\)](#) and define the correlated subspace as the set of hydrogen  $1s$  orbitals (with both spin directions) centered on each of the hydrogen atom positions  $\vec{R}_a$ :  $\phi_{a,\sigma} = \psi_{1s}(\vec{R} - \vec{R}_a)$ . The interaction  $\hat{\mathbf{I}}^{\text{corr}}$  is obtained from the appropriately antisymmetrized Coulomb integrals. To perform the integrals we approximate the atomic wave functions as Gaussians using the standard minimal STO-6G basis [[Hehre et al.](#)].

To determine which interactions must be retained we observe that for  $n = 6$  the problem posed by the correlated ( $1s$ ) subspace with the complete interaction can be diagonalized exactly. The upper panel of [Fig. 5.2](#) compares the resulting energies to those obtained by treating some parts of the interaction via HF and the other parts exactly. We focus on the on-site term, conventionally denoted  $U = \hat{\mathbf{I}}_{a,a,a,a}^{\text{corr}}$  and the first neighbor terms  $\hat{\mathbf{I}}_{a,a,a,b}^{\text{corr}}, \hat{\mathbf{I}}_{a,a,b,b}^{\text{corr}}, \hat{\mathbf{I}}_{a,b,a,b}^{\text{corr}}$  with  $b$  a nearest neighbor of site  $a$ , which we lump together into a term  $V_1$ . We define two models, “Exact( $U$ )”, where we treat the  $U$  term exactly and all other interactions by HF, and “Exact( $U, V_1$ )” where we treat the  $U$  and all  $V_1$  terms exactly and all other interactions by HF. The solid curve with small squares (black on-line), the dashed trace with solid up-pointing triangles (blue on-line) and the dotted trace with down-pointing triangles (magenta on-line) compare these three energies. The “Exact( $U, V_1$ )” approximation is much closer to the exact energy than the “Exact( $U$ )” approximation. We conclude that it is important to use

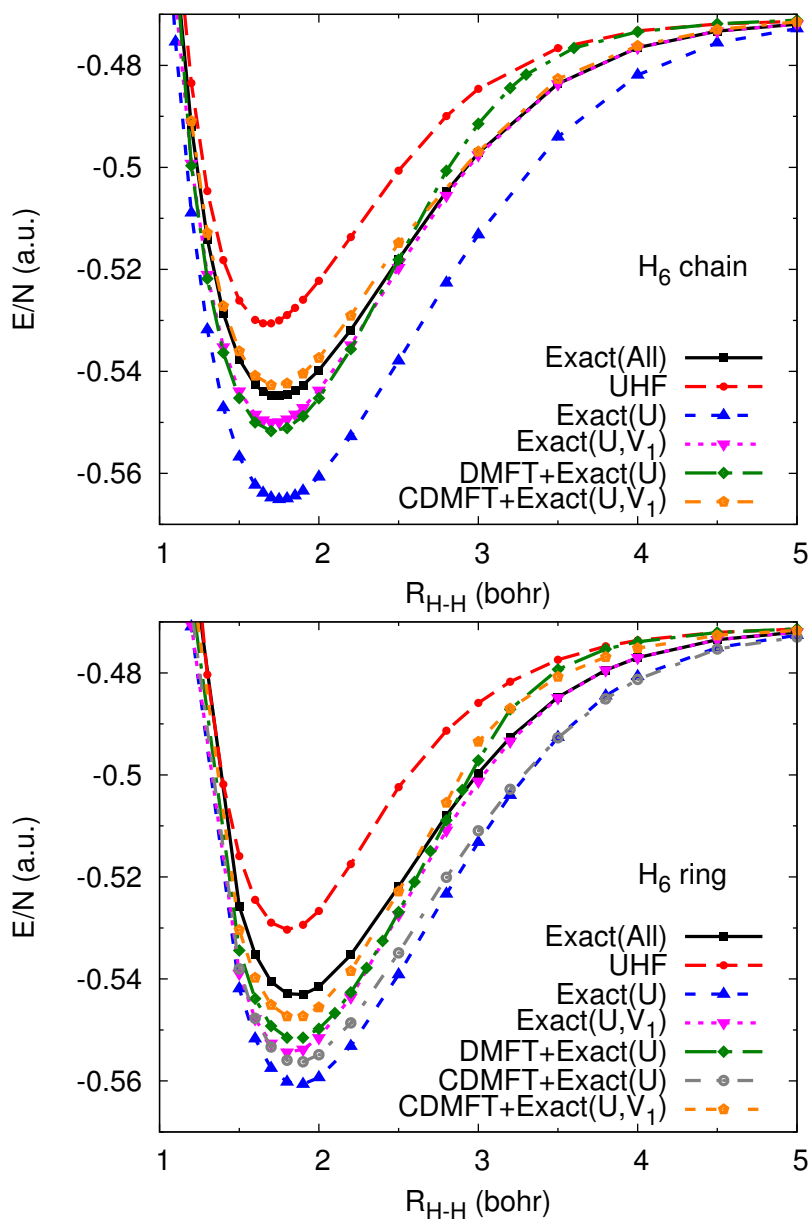


**Figure 5.2:** Energy of  $H_6$  chain (upper panel) and ring (lower panel) as a function of interatomic spacing  $R$  calculated with different methods as indicated.

a method which incorporates the on-site and first neighbor interactions, while the remaining terms may be treated approximately.

Each site has two (counting spin degeneracy) orbitals, so as defined in Sec. 5.3 the CDMFT method with  $N = 2$  means the cluster contains one atom. At this level we have an approximation to the “Exact( $U$ )” Hamiltonian which we refer to as “DMFT+Exact( $U$ )”. The CDMFT method with  $N = 4$  corresponds to a two-atom cluster and constitutes approximation to the “Exact( $U, V_1$ )” Hamiltonian which we refer to as “CDMFT+Exact( $U, V_1$ )”. We have also used CDMFT as an approximation to the “Exact( $U$ )” Hamiltonian. We refer to this approximation as “CDMFT+Exact( $U$ )”.

We have used these methods to calculate the ground state energies of the  $H_6$  chain and ring. In most of our calculations we have used the “exact diagonalization” (ED) method [Caffarel and Krauth (1994)] to solve the quantum impurity model. Up to 10 bath sites were used in the “CDMFT+Exact( $U, V_1$ )” calculation of the  $H_{50}$  chain; convergence with number of bath sites was verified. In a few cases we also verified that a continuous-time quantum Monte Carlo (CT-QMC) method [Werner et al. (2006)] gives identical results. The two panels of Fig. 5.2 shows that each approximation produces a result which lies somewhat above the exact result for the Hamiltonian which it approximates, with CDMFT providing a better approximation than DMFT. (Note that some of the errors arising from the restriction to the “Exact( $U$ )” or “Exact( $U, V_1$ )” Hamiltonians are compensated by errors in the DMFT solution.) Both DMFT approximations locate the minimum in the  $E(R)$  curve at essentially the exact position ( $\sim 1.75$  bohr), unlike the HF approximation ( $\sim 1.7$  bohr). Also, although it is difficult to perceive in the figures, the “DMFT+Exact( $U$ )” equations have a phase transition at  $R \sim 4$  bohr while the “Exact( $U, V_1$ )” does not have any phase transition. In extensive studies of Hubbard model systems with only local interactions Sangiovanni and co-workers found that going from single-site to 2-site

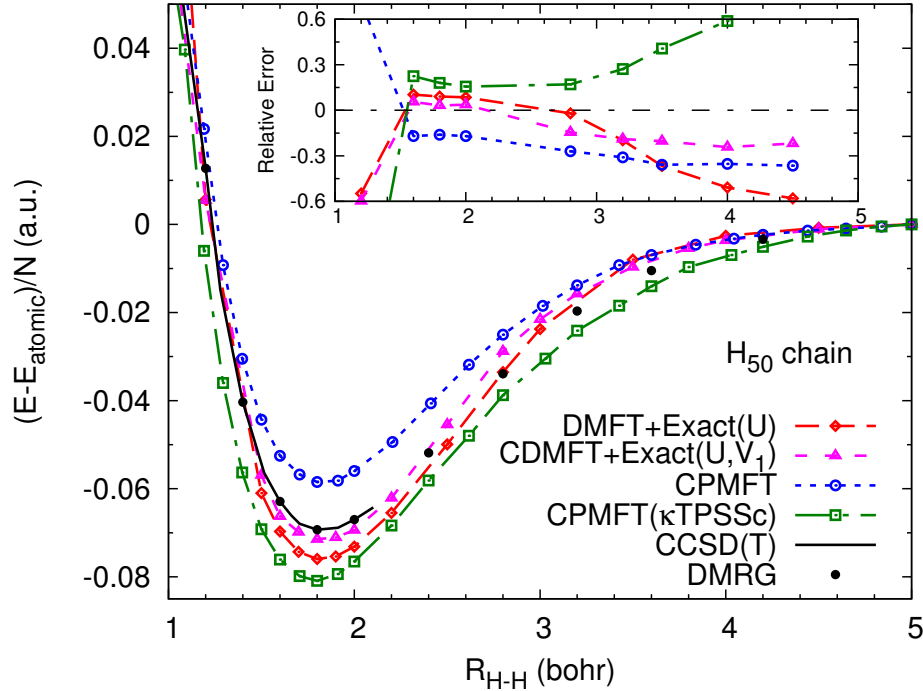


**Figure 5.3:** Main panel: energy of H<sub>50</sub> chain as a function of interatomic separation  $R$  calculated by the methods of this paper and compared to digitization of data presented in Tsuchimochi and Scuseria (2009) for coupled cluster methods (CCSD), density matrix renormalization group (DMRG, see Hachmann et al. (2006)) and other wave function based methods (CPMFT). Inset: Relative error of CPMFT and DMFT methods, defined as  $(E_{\text{method}} - E_{\text{DMRG}})/(E_{\text{DMRG}} - E_{\text{isolated atom}})$ .

clusters improved the energy substantially; going to large cluster sizes produced a slow and oscillating convergence to the exact result [Koch et al. (2008)]. The differences between 2-site and exact results are less than the errors involved in constructing the approximate Hamiltonians, and will not be of interest here.

The main panel and inset of Fig. 5.3 compares the energies of a 50 atom hydrogen chain obtained by our single-site and two-site cluster DMFT methods to the energies obtained from other approximate methods [Tsuchimochi and Scuseria (2009)] and from the density matrix renormalization group, which is believed to provide a



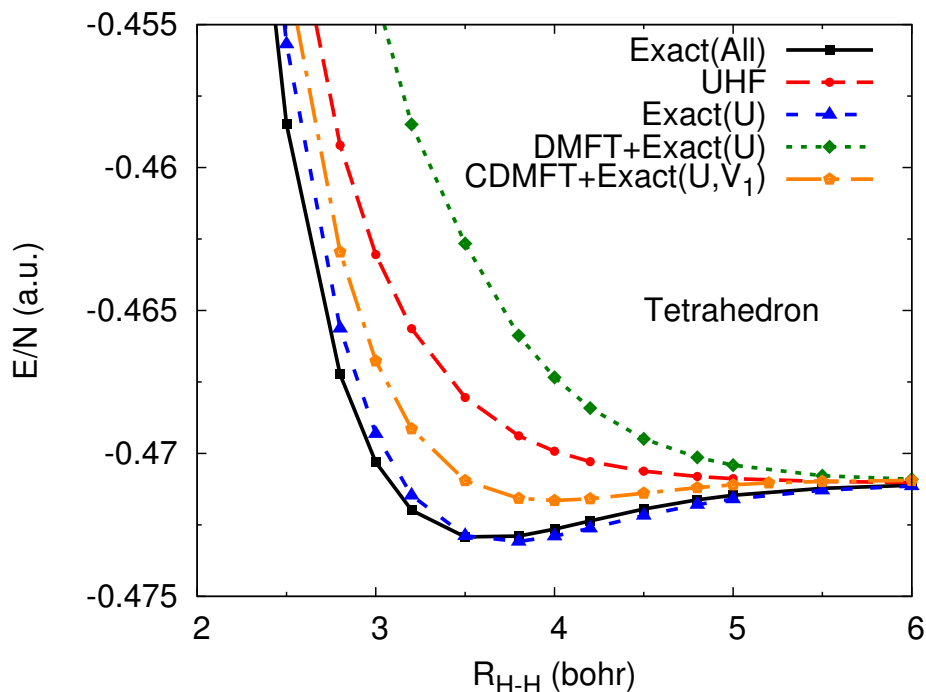


**Figure 5.4:** Energy curves of tetrahedrally configured  $H_4$  calculated by different methods as indicated.

numerically exact solution to the problem. The solid line is a coupled cluster calculation also reported in [Tsuchimochi and Scuseria \(2009\)](#); this weak coupling method fails to converge as the separation increases beyond  $R > 2.1$  bohr. The dotted and dashed lines labelled CPMFT are obtained from a variational wave function method [[Tsuchimochi and Scuseria \(2009\)](#)]. The inset, which shows errors relative to DMRG, demonstrates that even the relatively primitive DMFT methods used here are generically accurate over the whole intermediate to strongly correlated regime ( $R \geq 1.5$  bohr). In the weakly correlated ( $R < 1.5$  bohr) regime other methods (for example coupled cluster) are preferred but it should be emphasized that these methods fail in the strongly correlated (here  $R \geq 2.1$  bohr) regime.

Fig. 5.4 shows energies obtained for the tetrahedrally coordinated  $H_4$  molecule, which is methodologically challenging because it is only weakly bound. Here HF fails qualitatively, predicting that the molecule is not bound at all. “DMFT+Exact( $U$ )” is

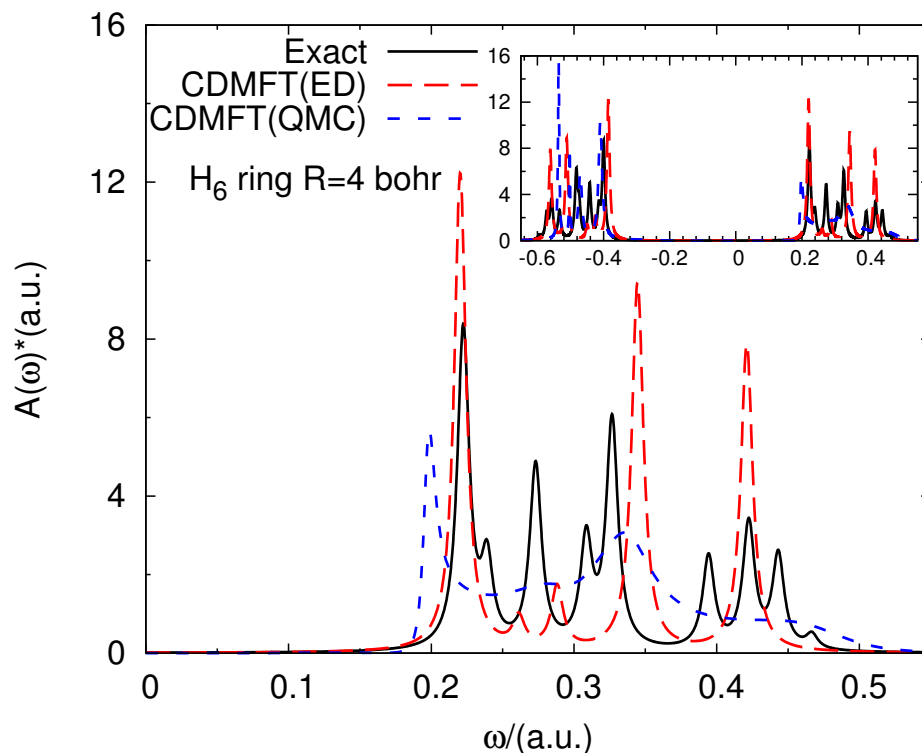


**Figure 5.5:** Main panel: electron addition spectra for  $H_6$  ring calculated from exact diagonalization of the full Hamiltonian in the correlated subspace and from the “CDMFT+Exact( $U, V_1$ )” equations using both ED and CT-QMC solvers. Inset: full frequency range.

qualitatively worse, even though the intersite terms in the Hamiltonian make only a small contribution to the ground state energy, as is seen from the close correspondence of the “Exact( $U$ )” and exact energy traces. Remarkably, the “CDMFT+Exact( $U, V_1$ )” trace (applied, of course, to the “Exact( $U, V_1$ )” model) produces a reasonable approximation to the energy, lying much closer to the exact curve and in particular predicting a minimum (although not quite at the correct location) even though the HF curve does not. This illustrates that appropriately chosen cluster methods can capture even quite subtle behavior.

We turn next to spectra. Fig. 5.5 presents the electron spectral function (many-body density of states) projected onto one site of an  $H_6$  ring. The spectra are of

course discrete, and (for the exact solution and the ED curves) have been artificially broadened. For the CT-QMC curve we have used Maximum Entropy method to continue the self-energy [Wang et al. (2009)], without any additional broadening. We see that “CDMFT+Exact( $U, V_1$ )” (with either solver) provides a good approximation to the exact curve, reproducing the gap in the excitation spectrum and the basic structure of the electron addition and removal spectra.

To summarize this section, we have shown that in the intermediate to strong correlation regime, appropriately chosen DMFT methods give results which are superior to other approximate methods. This, and the observation that the computational cost scales linearly with the system size (with a prefactor which depends strongly on the DMFT cluster) motivate a broader exploration of DMFT based methods in more complicated molecular systems, e.g., transition metal dioxide molecules as discussed in Sec. 5.5.

## 5.5 Transition Metal Dioxides

The dynamical mean-field concept involves isolating a small set of orbitals, whose correlations are treated exactly and which are embedded in a weakly correlated subspace, so a quantum impurity model results. In this section we examine the quantum impurity model representation of a more complicated system, a transition metal dioxide molecule. We consider here two molecules: the weakly correlated  $\text{TiO}_2$  ( $\text{Ti}^{4+}$ :  $3d^0$ ) and the more strongly correlated  $\text{CrO}_2$  ( $\text{Cr}^{4+}$ :  $3d^2$ ). The  $\text{VO}_2$  molecule ( $\text{V}^{4+}$ :  $3d^1$ ) which has an odd number of electrons is not considered as one has to perform the unrestricted calculations that we don’t want to address in this study.

We approximate the atomic wave functions using standard minimal STO-3G basis [Hehre et al.], which consists of the following atomic orbitals:

M	1s, 2s, 2p, 3s, 3p, 3d, 4s, 4p
O	1s, 2s, 2p

where M stands for the transition metal Ti or Cr. These orbitals are orthogonalized following the Gram-Schmidt (GS) algorithm in a way such that the M  $3d$  orbitals remain atomic-like which are orthogonal between each other. We define the correlated subspace as the set of M  $3d$  orbitals. Appendix B presents a note on the non-orthogonal basis set.

The Hamiltonian of the system is given by Eq. 5.4 with  $i, j, i', j'$  running over all the orbitals. Eq. 5.4 can be solved exactly for small systems (number of orbitals  $\leq \sim 15$ ), but difficulties arise when the system grows for which approximations are needed. In the DMFT method, we map the molecular system to an effective quantum impurity model. As in the hydrogen cluster, we use Hartree-Fock approximation to decouple the interactions between uncorrelated orbitals, and the interactions that involve both correlated and uncorrelated orbitals, whereas the interactions between correlated orbitals (M  $3d$ ) are treated dynamically in the quantum impurity model which is solved by the Exact Diagonalization method [Caffarel and Krauth (1994)].

To avoid the complications introduced by the non-diagonal hybridization functions such as the fitting of the hybridization function with a small number of bath states in the ED solver (or the fermionic sign problem in the QMC solver), we consider collinear geometry with varying M-O bond length. But we do note that the fitting problem gets improved when one increases the number of the discrete bath states to which the correlated orbitals are coupled (see Appendix C for an example). Therefore numerical methods that allow for more states to describe the hybridization function would enable us to easily treat the non-collinear case. The assumption of the collinear transition metal dioxide molecules leads to further simplification since the transition metal  $3d_{\pm 2}$  orbitals are decoupled from all other atomic orbitals and thus from the non-interacting bath states in the quantum impurity model, reducing the number of

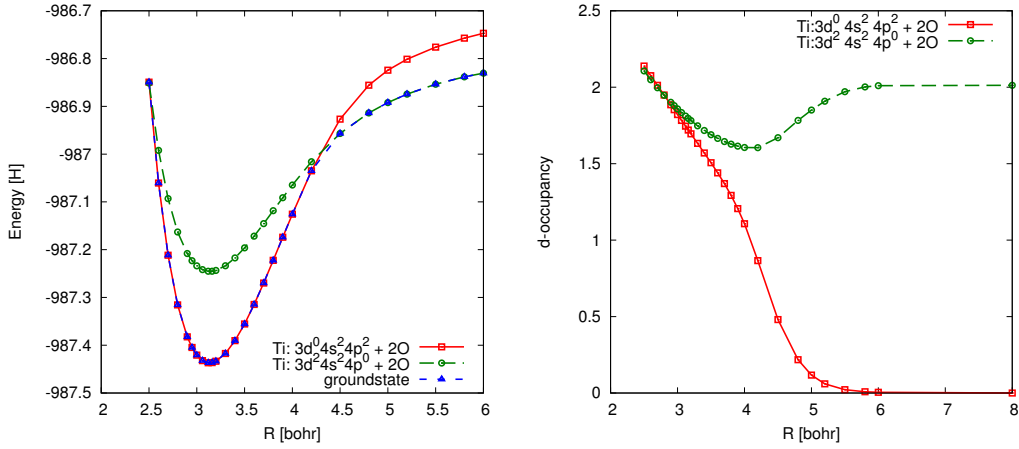


**Figure 5.6:** Restricted Hartree-Fock solutions for the collinear  $\text{TiO}_2$  molecule. Left panel: the potential energy. Right panel: the Ti  $3d$ -orbital occupancy defined in Eq. 5.10.

quantities (hybridization functions) to be parameterized. This allows for the orbitals  $3d_0, 3d_{\pm 1}$  to couple with slightly more bath states when the total number is fixed.

One also has to note that, different from the hydrogen clusters, since there is only one set of correlated orbitals in the approximate model of transition metal dioxide molecules, the DMFT self-consistency loop is unnecessary. Consideration of large clusters would require a DMFT self-consistency loop. For consistency, we denote the method “DMFT+Exact( $U_{dd}$ )”.

Fig. 5.6 presents the restricted Hartree-Fock solutions for the collinear  $\text{TiO}_2$  molecule. The left panel shows the Hartree-Fock energy as a function of the bond length between Ti and O in two symmetry groups, separating to  $\text{Ti} : 3d^0 4s^2 4p^2 + 2\text{O}$  and  $\text{Ti} : 3d^2 4s^2 4p^0 + 2\text{O}$  respectively at large  $R$  as seen in the collinear Ti  $3d$ -orbital occupancy shown in the right panel of Fig. 5.6. A “phase transition” is seen at  $R \approx 4.2$  bohr in the ground state energy, which also occurs in other approximate methods. The  $3d$ -orbital occupancy is defined as:

$$n_d = \text{Tr}_{[M \ 3d]} \mathbf{P}\mathbf{S} \quad (5.10)$$

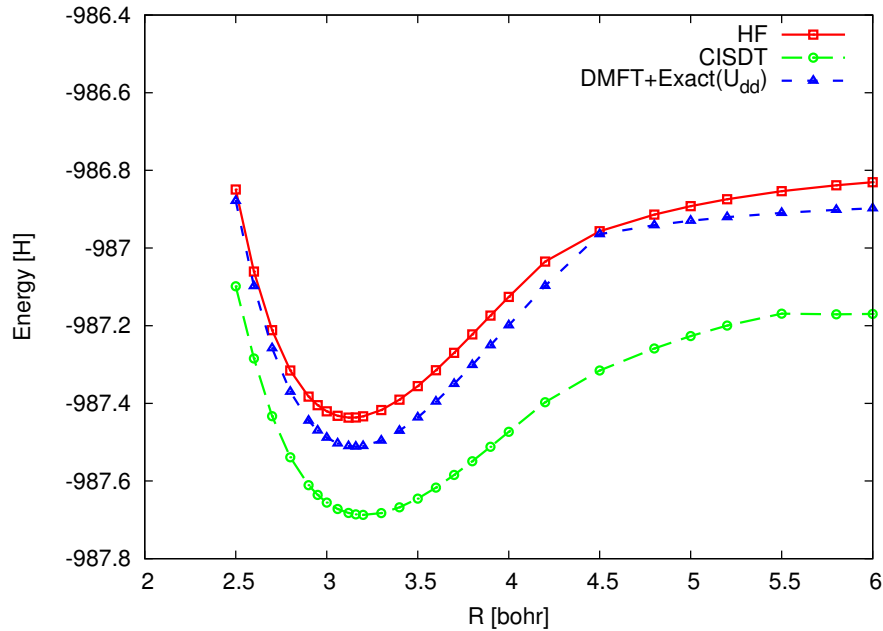


**Figure 5.7:** Comparison of the ground state energies as a function of the Ti-O bond length for the collinear  $\text{TiO}_2$  molecule obtained from “DMFT+Exact( $U_{dd}$ )” method and other quantum chemical approaches.

where the matrices  $\mathbf{S}$  and  $\mathbf{P}$  are the atomic orbital overlap matrix (defined in Eq. B.1) and density matrix. For calculations performed on a different set of orbitals other than the atomic orbitals, e.g. the GS orthogonal orbitals in the “DMFT+Exact( $U_{dd}$ )” method,  $n_d$  is obtained by first transforming the calculated density matrix to the atomic orbitals via the relation given in Eq. B.8 and then evaluating Eq. 5.10.

We compare the ground state energies for the collinear  $\text{TiO}_2$  molecule obtained from different methods in Fig. 5.7. The wave-function based quantum chemical method CISDT is believed to provide a very accurate approximation to this system. We see that the equilibrium bond length known as the position corresponding to the minimum energy in the potential energy curve is approximately consistent in all the methods. We define the correlation energy as the difference between the approximate energy and the CISDT energy, which is considered one of the most important quantities for the purpose of comparison. It is seen that the “DMFT+Exact( $U_{dd}$ )”

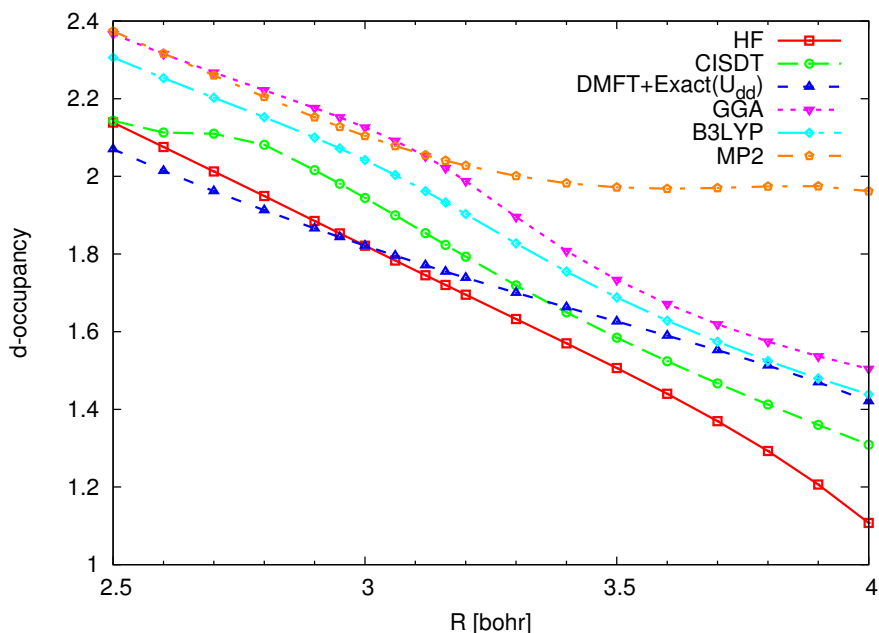


**Figure 5.8:** Comparison of Ti 3*d*-orbital occupancy in the collinear TiO<sub>2</sub> molecule obtained from “DMFT+Exact( $U_{dd}$ )” method and other quantum chemical approaches.

method applied to the chosen correlated orbitals improves the HF energy by about 20-30%. Fig. 5.8 shows the Ti 3*d*-orbital occupancy in the collinear TiO<sub>2</sub> molecule obtained from the “DMFT+Exact( $U_{dd}$ )” method, which is compared to the same quantity approximated by the Hartree-Fock and CISDT methods, two density functional theory methods and the perturbation theory method. A broad spread in the Ti 3*d*-orbital occupancy from different methods is observed. The “DMFT+Exact( $U_{dd}$ )” estimate is not worse than other methods under investigation. We also note that the “DMFT+Exact( $U_{dd}$ )” method correctly predicts the singlet ground state around equilibrium and the triplet ground state as the atoms separate far way from each other.

The ground state energies and the Cr 3*d*-orbital occupancy for the collinear CrO<sub>2</sub> molecule are presented in Fig. 5.9 and Fig. 5.10, for which the “CISDTQ triplet” approximation is considered the best quantum chemical solution. We see very similar

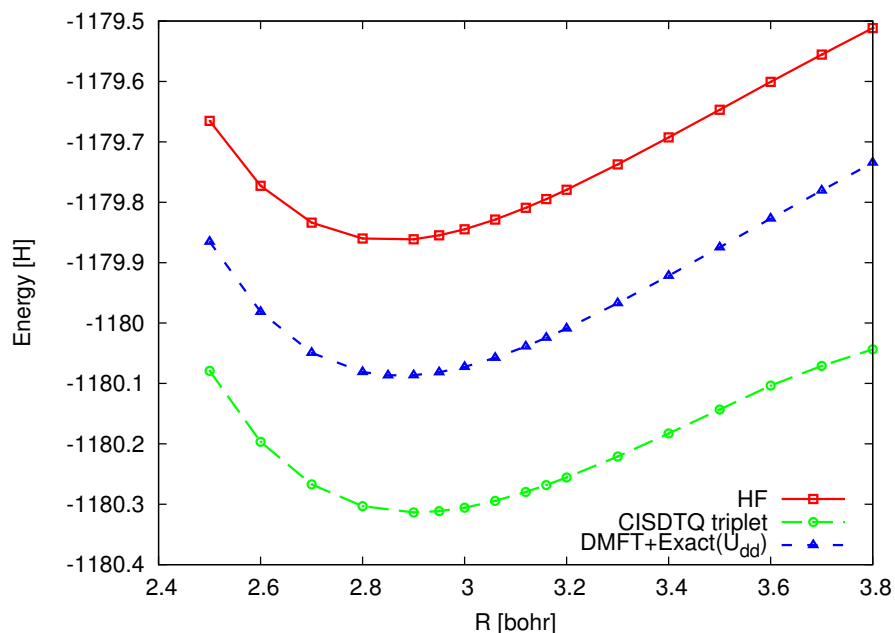


**Figure 5.9:** Comparison of the ground state energies as a function of the Cr-O bond length for the collinear  $\text{CrO}_2$  molecule obtained from “DMFT+Exact( $U_{dd}$ )” method and other quantum chemical approaches.

phenomenon as in the collinear  $\text{TiO}_2$  molecule, but the “DMFT+Exact( $U_{dd}$ )” method improves the HF energy by about 50% for the more strongly correlated  $\text{CrO}_2$  molecule.

For completeness, we show the spectral function for the collinear  $\text{CrO}_2$  molecule around equilibrium obtained from the “DMFT+Exact( $U_{dd}$ )” method. Fig. 5.11 should be compared to one or more of the quantum chemical methods, which we are lack of so far. But this demonstrates the easy access to the information of the dynamics in DMFT methods which is a great advantage over many wave-function based methods.

We have shown that the “DMFT+Exact( $U_{dd}$ )” method recovers part of the correlation energy, i.e. the difference between the “Exact” energy and the HF energy, in the transition metal dioxide molecules. One question immediately comes up: where is the energy lost? To investigate this question, we consider a reduced model which consists of M  $3d$  and O  $2p$  orbitals (11 orbitals in total). The model is constructed by taking the Hartree-Fock solution, building the Fock matrix, and removing the contri-



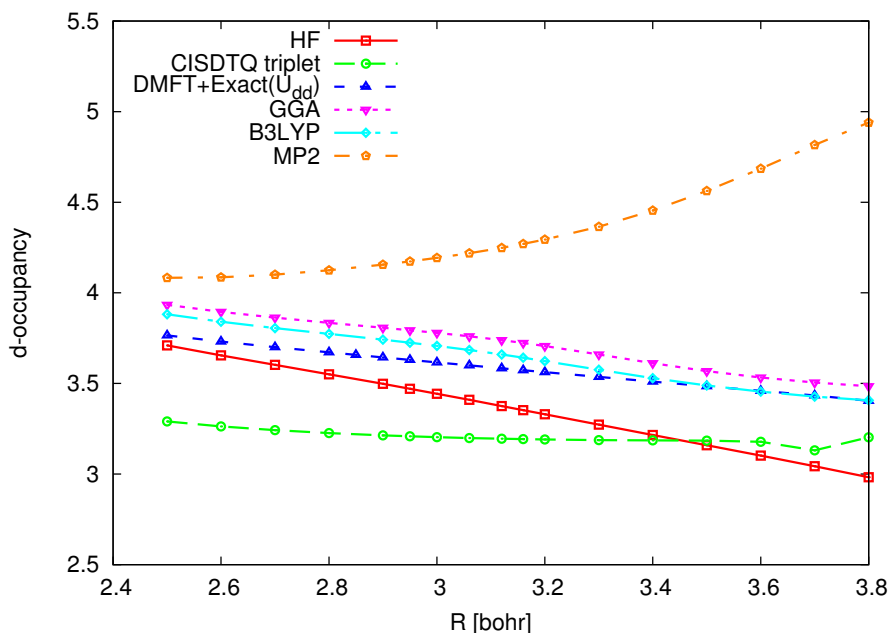


**Figure 5.10:** Comparison of Cr 3d-orbital occupancy in the collinear  $\text{CrO}_2$  molecule obtained from “DMFT+Exact( $U_{dd}$ )” method and other quantum chemical approaches.

contributions from the interactions within these 11 orbitals. The submatrix corresponding to the 11 orbitals of interest is taken as the one-body Hamiltonian.

Similarly, the Hamiltonian of the reduced model is in the form of Eq. 5.4. The model is small enough to be solved exactly. We consider the following levels of approximations to the interactions:

- Exact: all interactions are retained;
- HF: all interactions are treated via HF approximation;
- Exact( $U_{dd}$ ): the interactions between M 3d orbitals are retained;
- Exact( $U_{pp}$ ): the interactions between O 2p orbitals are retained;
- Exact( $U_{dd}+U_{pp}$ ): the interactions retained in both “Exact( $U_{dd}$ )” and “Exact( $U_{pp}$ )” are retained;

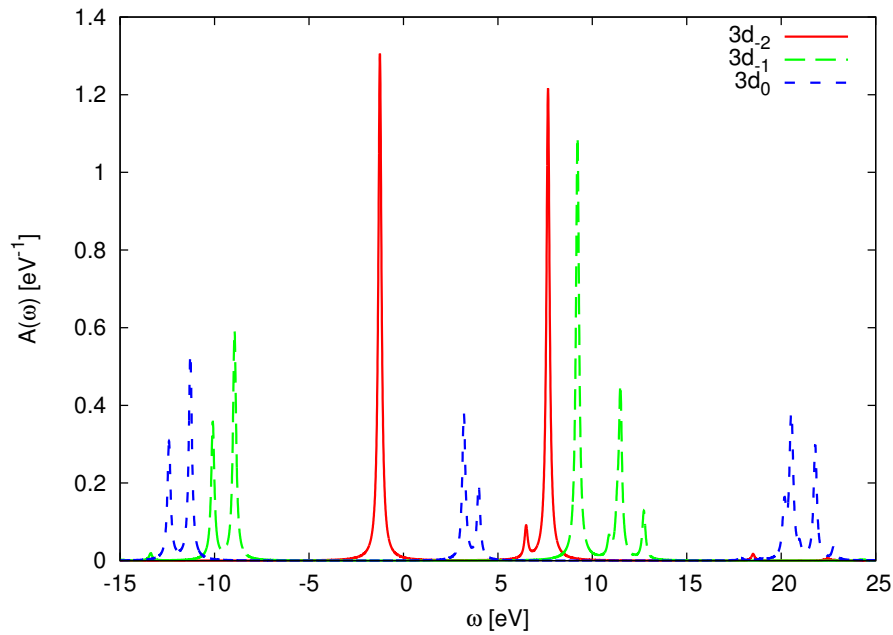


**Figure 5.11:** The spectral function for the collinear  $\text{CrO}_2$  molecule at  $R = 2.8$  bohr (around equilibrium) calculated from the “DMFT+Exact( $U_{dd}$ )” method using the ED solver.

- Exact( $U_{dd} + U_{pp} + U_{dp}$ ): the interactions retained in “Exact( $U_{dd} + U_{pp}$ )” and the inter-site interactions between M  $3d$  and O  $2p$  orbitals are retained.

**Table 5.1:** Comparison of different approximations in the reduced model for the collinear  $\text{CrO}_2$  model with Cr-O bond length  $R = 3.5$  bohr.

	$\Delta E = \frac{E - E_{\text{Exact}}}{E_{\text{HF}} - E_{\text{Exact}}}$	$n_d$	$S_z^2$
Exact	0	4.250	1.011
HF	1	3.948	0.314
Exact( $U_{dd}$ )	0.47	4.006	0.888
Exact( $U_{pp}$ )	0.50	4.244	0.196
Exact( $U_{dd} + U_{pp}$ )	-0.22	4.246	0.936
Exact( $U_{dd} + U_{pp} + U_{dp}$ )	-0.004	4.252	1.006

Table 5.1 presents one representative comparison of the ground state energy, the  $3d$ -orbital occupancy and the magnetic momenta  $[S_z]_d^2$  defined in orthogonal orbitals

as

$$\begin{aligned} n_d &= \sum_{m=-2}^2 (n_{d_m,\uparrow} + n_{d_m,\downarrow}), \\ [S_z]_d^2 &= \frac{1}{4} \sum_{m=-2}^2 (n_{d_m,\uparrow} - n_{d_m,\downarrow})^2. \end{aligned} \tag{5.11}$$

The calculations are done for the reduced model for the collinear CrO<sub>2</sub> molecule with Cr-O bond length  $R = 3.5$  bohr. Treating the interactions within the Cr  $3d$  orbitals dynamically in the “Exact( $U_{dd}$ )” approximation improves the HF energy by about 53% which is a similar level as seen in Fig. 5.9. “Exact( $U_{pp}$ )” provides a slightly worse approximation, whereas the “Exact( $U_{dd} + U_{pp}$ )” approximation underestimates the ground state energy but is much closer to the exact ground state energy. By further retaining the inter-site interactions between the Cr  $3d$  and O  $2p$  orbitals the “Exact( $U_{dd} + U_{pp} + U_{dp}$ )” approximation produces a very accurate estimate to the ground state energy. There is noticeable deviation in the “Exact( $U_{dd}$ )” approximation of the Cr  $3d$ -orbital occupancy from the exact solution. Remarkably, we observe that the interactions between the Cr  $3d$  orbitals have to be treated properly in order to get a reasonable approximation of the magnetic momenta.

The preceding discussion demonstrates that treating only local interactions on the transition metal  $3d$  orbitals dynamically is not a good enough approximation for the transition metal dioxide molecules. The inter-site interactions should be considered in a more appropriate manner in order to give a good account of the correlation energy. This requires a correlated subspace consisting of both the M  $3d$  and O  $2p$  orbitals asking for more effort in solving the effective quantum impurity model.

## 5.6 Summary

In summary, we have presented the application of dynamical mean-field theory to the hydrogen clusters with superior performance in the intermediate to strong correlation regime, and the transition metal dioxide molecules which require more consideration of the interactions to be treated dynamically. The linear scaling with the system size (although probably with a large prefactor) in the computational cost makes the DMFT based method a worth pursuing alternative in the quantum chemical context. Many questions immediately arise. A more systematic comparative investigation of the merits of the different solvers available for the quantum impurity model is needed. The relation between cluster geometry and molecule geometry should be more fully explored. We used a HF method to treat the interactions not included in our DMFT calculation; use of other approaches, such as density functional or GW methods, may improve the energetics. Also, the cluster DMFT methods presently available were formulated in the infinite-system context relevant to condensed matter physics. Alternative formulations better suited to finite systems may exist.

More careful examination of complicated systems, where the partitioning into correlated and “passive” subspaces and determination of which interactions to treat becomes more of an issue, is important. More generally, molecules provide a new context in which to examine basic theoretical issues including the “double counting correction” needed when combining dynamical mean-field and density functional theory, as well as the possibility (discussed in [Kotliar et al. \(2006\)](#)) of using dynamical mean-field self-consistency ideas to more systematically define the correlated subspace. Research in all of these directions is in progress.

## Appendix A

# Note on the technical details for computing the vertex calculations of two-particle response functions

The calculation of vertex corrections in quantum Monte Carlo requires two steps: the calculation of the two-frequency Green's function  $G(\omega_1, \omega_2)$ , and the assembly of  $\Gamma_{a\sigma, b\sigma'}^\Omega$  from  $G$  using Wick's theorem. The main purpose of this note is to present the technical details in the calculation of the vertex corrections for two-particle response functions discussed in Chap. 3.

### A.1 Two dimensional Fourier transform

Computing  $G(\omega_1, \omega_2)$  is the computationally dominating part, as it involves a two-dimensional Fourier transform. Improvement can be made by efficient implementation of the Fourier transform, for which we have used the NFFT 3.0 library developed by [Keiner et al. \(2009\)](#) for various nonequispaced fast Fourier transforms. And we thank Thomas Maier and Thomas Schulthess for private communication on this subject.

The  $d$ -dimensional NFFT computes the discrete Fourier transform:

$$\hat{h}_{\mathbf{k}} := \sum_{j=0}^{M-1} f_j e^{2\pi i \mathbf{k} \mathbf{x}_j} \quad (\text{A.1})$$

from the  $d$ -dimensional torus

$$\mathbb{T}^d := \{\mathbf{x} = (x_t)_{t=0,\dots,d-1} \in \mathbb{R}^d : -\frac{1}{2} \leq x_t < \frac{1}{2}, t = 0, \dots, d-1\} \quad (\text{A.2})$$

which serves as domain for the nonequispaced nodes  $\mathbf{x}$ . Possible frequencies  $\mathbf{k} \in \mathbb{Z}^d$  are collected in the multi-index set

$$I_{\mathbf{N}} := \{\mathbf{k} = (k_t)_{t=0,\dots,d-1} \in \mathbb{Z}^d : -\frac{N_t}{2} \leq k_t < \frac{N_t}{2}, t = 0, \dots, d-1\}, \quad (\text{A.3})$$

with  $\mathbf{N} = (N_t)_{t=0,\dots,d-1}$  being the even multibandlimit, i.e.,  $N_t \in 2\mathbb{N}$ .

In our problem, we need to evaluate the Green's function in Matsubara frequencies, as a function of two frequency indices:

$$G_{kk'}(i\omega_n, i\omega_m) = \beta \mathcal{G}_{kk'}^0(i\omega_n) \delta_{nm} - \frac{\mathcal{G}_{kk}^0(i\omega_n) \mathcal{G}_{k'k'}^0(i\omega_m)}{N_c} \sum_{pq} e^{i\omega_n \tau_p} e^{ik s_p} M_{pq} e^{-ik' s_q} e^{-i\omega_m \tau_q}. \quad (\text{A.4})$$

The main difficulty is the computation of the sum on the right hand side of Eq. A.4, which can be rewritten as

$$M_{nm} = \sum_{pq} e^{i\omega_n \tau_p} M'_{pq} e^{-i\omega_m \tau_q} \quad (\text{A.5})$$

with  $M'_{pq} = e^{ik s_p} M_{pq} e^{-ik' s_q}$ . Eq. A.5 can be evaluated by a  $2d$  Fourier transform. Alternatively we can factorize Eq. A.5 as:

$$M_{nm} = \sum_q \left[ \sum_p e^{i\omega_n \tau_p} M'_{pq} \right] e^{-i\omega_m \tau_q}. \quad (\text{A.6})$$

The time consumed is reduced considerably by evaluating Eq. A.6 with a set of  $1d$  NFFT instead of applying a  $2d$  NFFT to Eq. A.5.

One difficulty in our implementation is that the imaginary time points are spaced between 0 and  $\beta$ , not between  $-1/2$  and  $1/2$ . It is therefore necessary to rescale the variables as:

$$\begin{aligned}
M_{nm} &= \sum_q \left[ \sum_p e^{i\omega_n \tau_p} M'_{pq} \right] e^{-i\omega_m \tau_q} \\
&= \sum_q \left[ \sum_p e^{i(2n+1)\pi \frac{\tau_p}{\beta}} M'_{pq} \right] e^{-i\omega_m \tau_q} \\
&= \sum_q \left[ \sum_p e^{i\pi \frac{\tau_p}{\beta}} e^{i\pi n} M'_{pq} e^{i2\pi n(\frac{\tau_p}{\beta} - \frac{1}{2})} \right] e^{-i\omega_m \tau_q} \\
&= e^{i\pi n} \sum_q \left[ \sum_p e^{i\pi \frac{\tau_p}{\beta}} M'_{pq} e^{i2\pi n \tau'_p} \right] e^{-i\omega_m \tau_q} \tag{A.7} \\
&= e^{i\pi n} \sum_q e^{-i(2m+1)\pi \frac{\tau_q}{\beta}} F''_{qn} \\
&= e^{i\pi n} \sum_q e^{i\pi \frac{\tau_q}{\beta}} e^{-i\pi(m+1)} e^{i2\pi(-m-1)(\frac{\tau_q}{\beta} - \frac{1}{2})} F''_{qn} \\
&= e^{i\pi(n-m-1)} \sum_q e^{i\pi \frac{\tau_q}{\beta}} e^{i2\pi m' \tau'_q} F''_{qn}.
\end{aligned}$$

We have introduced  $-1/2 \leq \tau'_{p(q)} = \tau_{p(q)}/\beta - 1/2 < 1/2$  and  $-N \leq m' = -m-1 < N$ , thus satisfying the restriction in Eq. A.1.

## A.2 Symmetry

The symmetry of the perturbation (Eq. 3.13) implies that, on the 8-site cluster as shown in Fig. 4.1, the contributions of sectors  $A, B$  and  $D$  average to zero in the case of Raman  $B_{1g}$  scattering, and the contributions of sectors  $A, C$  and  $D$  average to zero in the case of Raman  $B_{2g}$  scattering and the optics. Therefore for the four-point

function

$$\Gamma_{K\sigma,K'\sigma'}^\Omega = \left\langle c_{K\sigma}(\omega + \Omega) c_{K\sigma}^\dagger(\omega) c_{K'\sigma'}(\omega') c_{K'\sigma'}^\dagger(\omega' + \Omega) \right\rangle, \quad (\text{A.8})$$

only terms with  $K, K' \in \{(0, \pi), (\pi, 0)\}$  (or  $K, K' \in \{(\pm\pi/2, \pm\pi/2)\}$ ) need to be measured. Similar symmetry restrictions apply to the four-site and to larger clusters.

Let us take the Raman  $B_{1g}$  scattering in an 8-site cluster for example. We define the quadruple quantities

$$\begin{aligned} G_Q^1 &= \left( G_{C_x\uparrow}^1 - G_{C_y\uparrow}^1 + G_{C_x\downarrow}^1 - G_{C_y\downarrow}^1 \right) / 4; \\ a_Q^1 &= (\mathcal{G}_0^{-1})_Q^1 = \left( a_{C_x\uparrow}^1 - a_{C_y\uparrow}^1 + a_{C_x\downarrow}^1 - a_{C_y\downarrow}^1 \right) / 4; \end{aligned} \quad (\text{A.9})$$

and rewrite Eq. 3.26 as

$$G_Q^1(\omega + \Omega, \omega) = T^2 \sum_{\omega_1} \Gamma_Q^\Omega(\omega, \omega_1) a_Q^1(\omega_1 + \Omega, \omega_1) \quad (\text{A.10})$$

with

$$\begin{aligned} \Gamma_Q^\Omega(\omega, \omega_1) &= \frac{1}{4} \left[ \left( \Gamma_{C_x\uparrow, C_x\uparrow}^\Omega + \Gamma_{C_y\uparrow, C_y\uparrow}^\Omega + \Gamma_{C_x\downarrow, C_x\downarrow}^\Omega + \Gamma_{C_y\downarrow, C_y\downarrow}^\Omega \right) \right. \\ &\quad - \left( \Gamma_{C_x\uparrow, C_y\uparrow}^\Omega + \Gamma_{C_y\uparrow, C_x\uparrow}^\Omega + \Gamma_{C_x\downarrow, C_y\downarrow}^\Omega + \Gamma_{C_y\downarrow, C_x\downarrow}^\Omega \right) \\ &\quad + \left( \Gamma_{C_x\uparrow, C_x\downarrow}^\Omega + \Gamma_{C_y\uparrow, C_y\downarrow}^\Omega + \Gamma_{C_x\downarrow, C_x\uparrow}^\Omega + \Gamma_{C_y\downarrow, C_y\uparrow}^\Omega \right) \\ &\quad \left. - \left( \Gamma_{C_x\uparrow, C_y\downarrow}^\Omega + \Gamma_{C_y\uparrow, C_x\downarrow}^\Omega + \Gamma_{C_x\downarrow, C_y\uparrow}^\Omega + \Gamma_{C_y\downarrow, C_x\uparrow}^\Omega \right) \right] \end{aligned} \quad (\text{A.11})$$

Eq. A.11 can be evaluated using the Wick's Theorem:

$$\begin{aligned} \Gamma_{K\sigma, K'\sigma'}^\Omega(\omega + \Omega, \omega, \omega', \omega' + \Omega) &= G_{K\sigma, K\sigma}(\omega + \Omega, \omega) G_{K'\sigma', K'\sigma'}(\omega', \omega' + \Omega) \\ &\quad - \delta_{\sigma\sigma'} G_{K\sigma, K'\sigma}(\omega + \Omega, \omega' + \Omega) G_{K'\sigma, K\sigma}(\omega', \omega). \end{aligned} \quad (\text{A.12})$$

Similar considerations apply to the Raman  $B_{1g}$  scattering in a 4-site cluster with the sectors  $P_x$  and  $P_y$  analogy to the sectors  $C_x$  and  $C_y$  in the 8-site cluster, as well



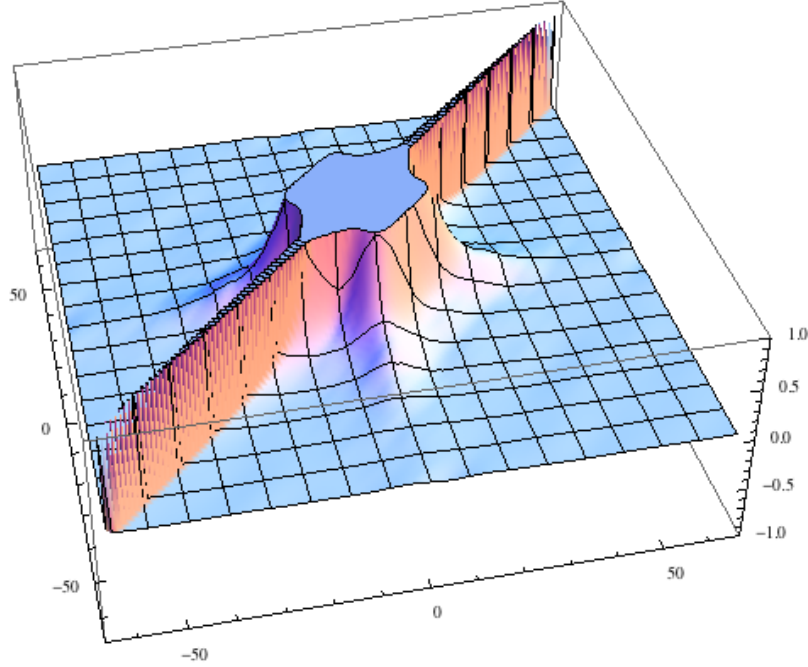


**Figure A.1:** The characteristic four-point function for Raman  $B_{1g}$  scattering at zero external frequency ( $\Omega = 0$ ) as a function of internal frequencies  $(\omega, \omega')$ .

as the Raman  $B_{2g}$  scattering and optical conductivity in an 8-site cluster for which the sector  $B$ 's centered at  $(\pm\pi/2, \pm\pi/2)$  make non-trivial contributions to the vertex corrections.

### A.3 Data Storing

We show one representative plot of the four-point function in Raman  $B_{1g}$  scattering at zero external frequency ( $\Omega = 0$ ) in Fig. A.1. The  $x$ -axis and  $y$ -axis denote the internal frequencies  $\omega, \omega'$ , and the  $z$ -axis denotes the four-point function  $\Gamma_Q^{\Omega=0}(\omega, \omega')$ . It is obvious that the function has significant value along the diagonal ( $\omega = \omega'$ ) and the nearby region, and decays quickly away from the diagonal.

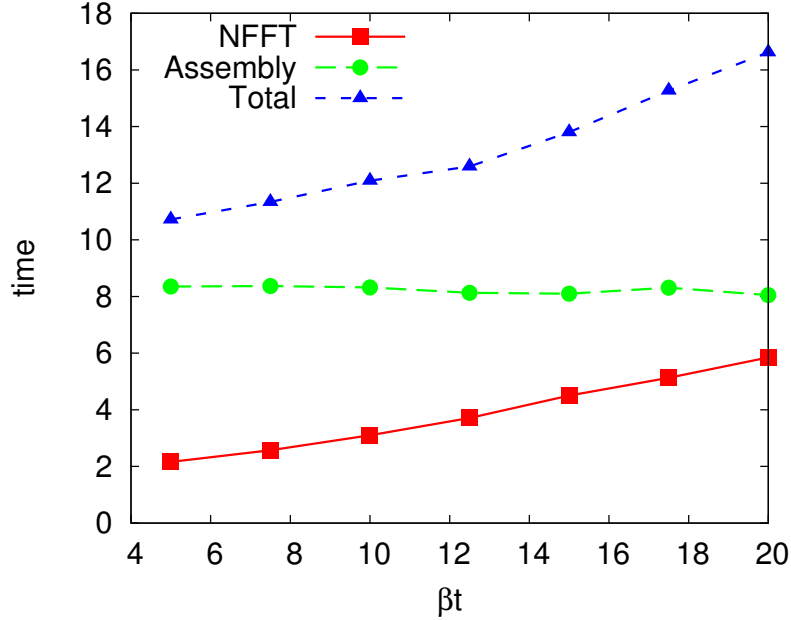


**Figure A.2:** Consuming time of the four-point function ( $\Gamma_{K\sigma, K'\sigma'}^\Omega$ ) measurement.

Storing the three frequency ( $\Omega, \omega, \omega'$ ) dependent  $\Gamma_Q^\Omega$  is memory intensive but the high frequency behavior is known as seen in Fig. A.1: for  $\omega \neq \omega'$   $\Gamma_Q^\Omega$  decays faster than  $\omega^2$ . We therefore choose to measure more frequencies along the diagonal  $\omega = \omega'$  than away from the diagonal, where we measure  $\Gamma_Q^\Omega$  on a stripe of size  $4\Delta_1\Delta_2$  with extent  $\Delta_1$  along the diagonal  $\omega = \omega'$  and  $\Delta_2$  perpendicular to it:  $|\omega + \omega' + \Omega| \leq \Omega + \Delta_1, |\omega - \omega'| \leq \Delta_2$ .  $\Delta_1, \Delta_2$  are determined empirically to cover the region in which  $\Gamma_Q^\Omega$  is non-trivial.

Fig. A.2 shows the time cost for the Fourier transform (square), the assembly by applying Wick's theorem (circle), and the total time (triangle) as a function of the inverse temperature. Apparently the assembly procedure is the dominating step for the four-point function measurement which is roughly independent of the temperature. The time consumed for the NFFT increases approximately linearly as the temperature is decreased.

## A.4 The Covariance

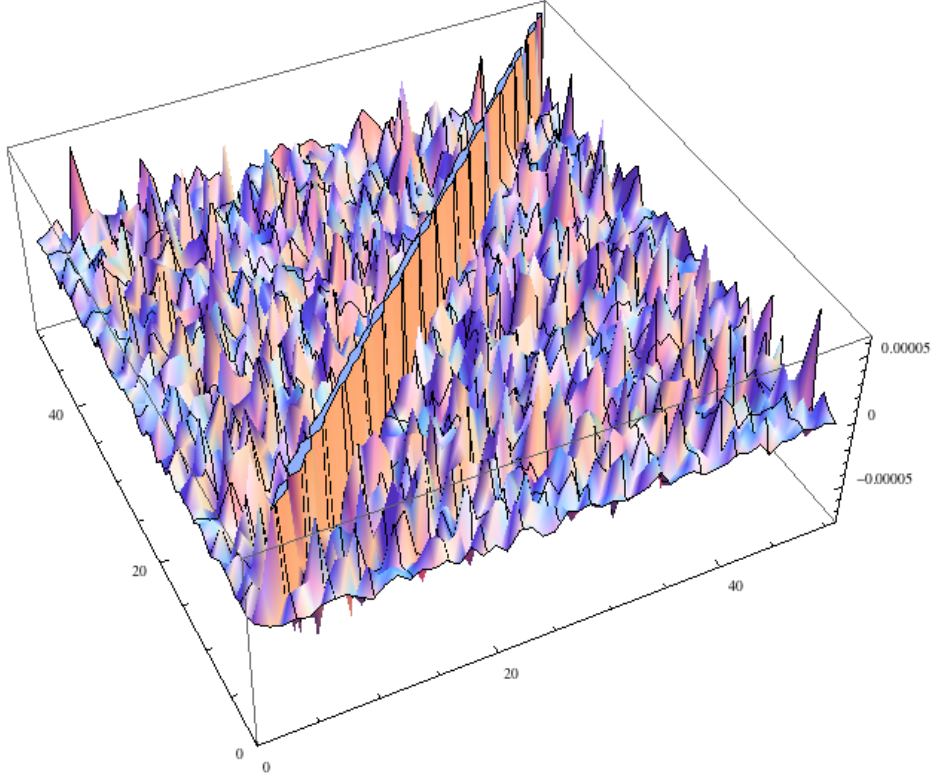


**Figure A.3:** The characteristic covariance matrix for the two-particle response function (e.g. Raman scattering) measured on Matsubara frequencies.

To properly treat the noise correlations which are encoded in the covariance matrix required for the Maximum Entropy analytic continuation, we perform a jackknife analysis based on  $M \approx 16$  independent quantum Monte Carlo solutions of the mean-field equations.

We denote  $\chi_i(\omega)$  for  $i = 1, \dots, M$  the jackknife averages of the two-particle response function when all measurements but the  $i$ -th measurement are used for the estimate:

$$\chi_i(\omega) = \frac{1}{M-1} \sum_{j \neq i} \chi_j(\omega). \quad (\text{A.13})$$

The jackknife estimate for  $\chi(\omega)$  is given by

$$\chi(\omega) = \bar{\chi}(\omega) = \frac{1}{M} \sum_{i=1}^M \chi_i(\omega) \quad (\text{A.14})$$

with the covariance matrix

$$\text{Cov}(\chi(\omega_1, \omega_2)) = \frac{M-1}{M} \sum_{i=1}^M (\chi_i(\omega_1) - \bar{\chi}(\omega_1)) (\chi_i(\omega_2) - \bar{\chi}(\omega_2)). \quad (\text{A.15})$$

Our analysis presented in Fig. A.3 shows that the resulting covariance matrix for the two-particle response functions measured on Matsubara frequency axis is essentially diagonal, meaning that the response functions at different Matsubara frequencies are uncorrelated.

## Appendix B

# Note on the non-orthogonal basis set

The basis sets that are used in the molecular calculations are usually normalized but not orthogonal to each other. However for the formalism of second quantization and the many-body Green's function theory, it is sometimes necessary to use an orthogonal set of one-particle basis states. For a set of functions  $\{\phi_\mu\}$  that are not orthogonal, i.e.,

$$\int d\mathbf{r} \phi_\mu^*(\mathbf{r}) \phi_\nu(\mathbf{r}) = S_{\mu\nu}, \quad (\text{B.1})$$

where  $\mathbf{S}$  is called the overlap matrix, it is always possible to find a transformed set of functions  $\{\phi'_\mu\}$  given by

$$\phi'_\mu = \sum_\nu X_{\nu\mu} \phi_\nu \quad (\text{B.2})$$

that form an orthogonal set. There are various ways to orthogonal the basis set  $\{\phi_\mu\}$ , e.g., the Gram-Schmidt orthogonalization process and the Löwdin transformation (also called symmetric orthogonalization which uses the inverse square root of  $\mathbf{S}$  for the transformation matrix  $\mathbf{X}$ ).

We denote the quantities in the transformed orthogonal set by  $'$ . The overlap

matrix in the transformed orthogonal set is the identity matrix:

$$\mathbf{S}' = \mathbf{X}^\dagger \mathbf{S} \mathbf{X} = \mathbf{1}. \quad (\text{B.3})$$

In the language of second quantization, the non-orthogonal version of the fundamental anti-commutation relation

$$\{c_\alpha, c_\beta^\dagger\} = S_{\alpha\beta}^{-1} \quad (\text{B.4})$$

is converted to the familiar fermionic anti-commutation relation

$$\{c_\alpha, c_\beta^\dagger\} = \delta_{\alpha\beta} \quad (\text{B.5})$$

after the orthogonal transformation.

The overlap matrix  $\mathbf{S}$ , one-electron Hamiltonian  $\mathbf{H}$  and two-electron integrals  $\mathbf{I}$  can be easily obtained from quantum chemical programs such as Dalton [DALTON2011 (2011)], but in the unorthogonal atomic orbitals. The one-electron Hamiltonian in the transformed orthogonal orbitals  $\mathbf{H}'$  is related to  $\mathbf{H}$  by the relation:

$$\mathbf{H}' = \mathbf{X}^\dagger \mathbf{H} \mathbf{X}, \quad (\text{B.6})$$

whereas the two-electron integrals  $\mathbf{I}'$  can be evaluated via

$$I_{ijkl} = \sum_{\mu\nu\sigma\lambda} X_{\mu i} X_{\nu j} X_{\sigma k} X_{\lambda l} I_{\mu\nu\sigma\lambda}. \quad (\text{B.7})$$

The relation between the density matrix in the non-orthogonal and orthogonal sets is:

$$\mathbf{P}' = \mathbf{X}^\dagger \mathbf{S} \mathbf{P} \mathbf{S} \mathbf{X}. \quad (\text{B.8})$$

Other quantities are related in a similar manner.

## Appendix C

# Note on the fitting of the bare Green's function in the Exact Diagonalization solver

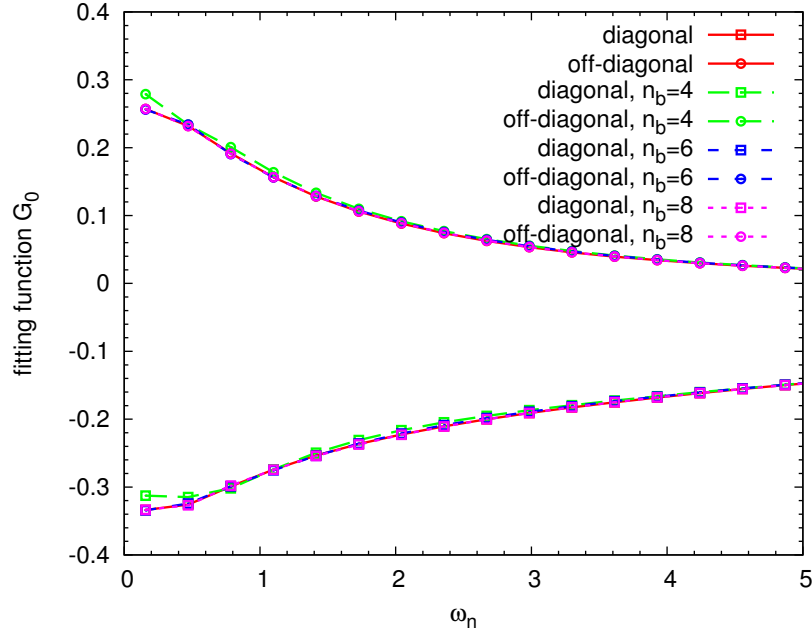


**Figure C.1:** Demonstration of the fitting problem for a non-diagonal bare Green's function  $\mathcal{G}_0(i\omega_n)$  in a 2-site CDMFT calculation. Different numbers of bath states (as indicated) are used to fit the diagonal (squares) and off-diagonal (circles) elements of  $\mathcal{G}_0(i\omega_n)$ .

In the Exact Diagonalization (ED) solver, the impurity sites are coupled to a discrete set of bath states and the hybridization function is approximated in terms of a finite number of holes. One important step is the estimation of the unknown parameters  $\varepsilon_k$  and  $V_{k\mu}$  in Eq. 2.33.

We have technical difficulties for the fitting of a non-diagonal bare Green's function with a small number of bath states. Fig. C.1 shows a characteristic example of the fitting problem for a non-diagonal bare Green' function in a 2-site CDMFT calculation. We see noticeable deviation from the function to be fitted (red traces) when the two impurity sites are coupled to only 4 bath states (green traces). The fitting quality gets improved significantly by increasing the number of bath states to 6 (and even better when 8 bath states are considered). Therefore we believe that numerical methods that allow for more bath states would enable calculations for more complicated systems.



# Bibliography

- Abanov, A., Chubukov, A. V. and Schmalian, J., Singularities in the optical response of cuprates, *Phys. Rev. B* **63**, 180510 (2001), [URL](#).
- Alloul, H., Ohno, T. and Mendels, P.,  $^{89}\text{Y}$  NMR evidence for a fermi-liquid behavior in  $\text{YBa}_2\text{Cu}_3\text{O}_{6+x}$ , *Phys. Rev. Lett.* **63**, 1700 (1989), [URL](#).
- Altshuler, B. L., Ioffe, L. B. and Millis, A. J., Theory of the spin gap in high-temperature superconductors, *Phys. Rev. B* **53**, 415 (1996), [URL](#).
- Andersen, O. K., Liechtenstein, A. I., Jepsen, O. and Paulsen, F., LDA energy bands, low-energy hamiltonians,  $t'$ ,  $t''$ ,  $t_{\perp}(k)$ , and  $J_{\perp}$ , *J. Phys. Chem. Solids* **56**, 1573 (1995), [URL](#).
- Anderson, P. W., The Resonating Valence Bond State in  $\text{La}_2\text{CuO}_4$  and superconductivity, *Science* **235**, 1196 (1987), [URL](#).
- Anisimov, V. I., Zaanen, J. and Andersen, O. K., Band theory and Mott insulators: Hubbard  $U$  instead of Stoner  $I$ , *Phys. Rev. B* **44**, 943 (1991), [URL](#).
- Aranov, A., Chubukov, A. V. and Schmalian, J., Quantum-critical superconductivity in underdoped cuprates, *EPL* **55**, 369 (2001), [URL](#).
- Bajdich, M., Tiago, M. L., Hood, R. Q., Kent, P. R. C. and Reboredo, F. A., Systematic Reduction of Sign Errors in Many-Body Calculations of Atoms and Molecules, *Phys. Rev. Lett.* **104**, 193001 (2010), [URL](#).

- Barthel, T., Schollwöck, U. and White, S. R., Spectral functions in one-dimensional quantum systems at finite temperature using the density matrix renormalization group, *Phys. Rev. B* **79**, 245101 (2009), [URL](#).
- Bartlett, R. J. and Musiał, M., Coupled-cluster theory in quantum chemistry, *Rev. Mod. Phys.* **79**, 291 (2007), [URL](#).
- Basov, D. N. and Timusk, T., Electrodynamics of high- $T_c$  superconductors, *Rev. Mod. Phys.* **77**, 721 (2005), [URL](#).
- Bednorz, J. G. and Müller, K. A., Possible high- $T_c$  superconductivity in the Ba-La-Cu-O system, *Z. Phys. B: Condens. Matter* **64**, 189 (1986), [URL](#).
- Bethe, H. A., Theorie der Beugung von Elektronen an Kristallen, *Ann. Phys. (Leipzig)* **87**, 55 (1928), [URL](#).
- Bickers, N. E., Review of techniques in the large- $N$  expansion for dilute magnetic alloys, *Rev. Mod. Phys.* **59**, 845 (1987), [URL](#).
- Blanc, S., Gallais, Y., Sacuto, A., Cazayous, M., Méasson, M. A., Gu, G. D., Wen, J. S. and Xu, Z. J., Quantitative Raman measurement of the evolution of the Cooper-pair density with doping in  $\text{Bi}_2\text{Sr}_2\text{CaCu}_2\text{O}_{8+\delta}$  superconductors, *Phys. Rev. B* **80**, 140502 (2009), [URL](#).
- Bloch, F., Bemerkung zur Elektronentheorie des Ferromagnetismus und der elektrischen Leitfähigkeit, *Zeitschrift für Physik A Hadrons and Nuclei* **57**, 545 (1929), [URL](#).
- Blumberg, G., Liu, R., Klein, M. V., Lee, W. C., Ginsberg, D. M., Gu, C., Veal, B. W. and Dabrowski, B., Two-magnon Raman scattering in cuprate superconductors: Evolution of magnetic fluctuations with doping, *Phys. Rev. B* **49**, 13295 (1994), [URL](#).

- Born, M. and Oppenheimer, R., Zur Quantentheorie der Molekeln, *Ann. Phys.* (Leipzig) **389**, 457 (1927), [URL](#).
- Caffarel, M. and Krauth, W., Exact diagonalization approach to correlated fermions in infinite dimensions: Mott transition and superconductivity, *Phys. Rev. Lett.* **72**, 1545 (1994), [URL](#).
- Capone, M., de' Medici, L. and Georges, A., Solving the dynamical mean-field theory at very low temperatures using the Lanczos exact diagonalization, *Phys. Rev. B* **76**, 245116 (2007), [URL](#).
- Carbone, F., Kuzmenko, A. B., Molegraaf, H. J. A., van Heumen, E., Lukovac, V., Marsiglio, F., van der Marel, D., Haule, K., Kotliar, G., Berger, H., Courjault, S., Kes, P. H. and Li, M., Doping dependence of the redistribution of optical spectral weight in  $\text{Bi}_2\text{Sr}_2\text{CaCu}_2\text{O}_{8+\delta}$ , *Phys. Rev. B* **74**, 064510 (2006), [URL](#).
- Cava, R. J., van Dover, R. B., Batlogg, B. and Rietman, E. A., Bulk superconductivity at 36 K in  $\text{La}_{1.8}\text{Sr}_{0.2}\text{CuO}_4$ , *Phys. Rev. Lett.* **58**, 408 (1987), [URL](#).
- Ceperley, D. M. and Alder, B. J., Ground State of the Electron Gas by a Stochastic Method, *Phys. Rev. Lett.* **45**, 566 (1980), [URL](#).
- Chakraborty, S., Galanakis, D. and Phillips, P., Spectral kinks and mid-infrared optical conductivity of doped Mott insulators from strong electron correlations, *Phys. Rev. B* **78**, 212504 (2008), [URL](#).
- Chan, G. K.-L. and Head-Gordon, M., Highly correlated calculations with a polynomial cost algorithm: A study of the density matrix renormalization group, *J. Chem. Phys.* **116**, 4462 (2002), [URL](#).
- Chen, X. K., Naeini, J. G., Hewitt, K. C., Irwin, J. C., Liang, R. and Hardy, W. N.,

- Electronic Raman scattering in underdoped  $\text{YBa}_2\text{Cu}_3\text{O}_{6.5}$ , Phys. Rev. B **56**, R513 (1997), [URL](#).
- Choy, T.-P., Leigh, R. G. and Phillips, P., Hidden charge- $2e$  boson: Experimental consequences for doped Mott insulators, Phys. Rev. B **77**, 104524 (2008), [URL](#).
- Civelli, M., Doping-driven evolution of the superconducting state from a doped Mott insulator: Cluster dynamical mean-field theory, Phys. Rev. B **79**, 195113 (2009), [URL](#).
- Civelli, M., Capone, M., Georges, A., Haule, K., Parcollet, O., Stanescu, T. D. and Kotliar, G., Nodal-Antinodal Dichotomy and the Two Gaps of a Superconducting Doped Mott Insulator, Phys. Rev. Lett. **100**, 046402 (2008), [URL](#).
- Civelli, M., Capone, M., Kancharla, S. S., Parcollet, O. and Kotliar, G., Dynamical Breakup of the Fermi Surface in a Doped Mott Insulator, Phys. Rev. Lett. **95**, 106402 (2005), [URL](#).
- Coester, F. and Kümmel, H., Short-range correlations in nuclear wave functions, Nucl. Phys. **17**, 477 (1960), [URL](#).
- Comanac, A., Dynamical mean-field theory of correlated electron systems: New algorithms and applications to local observables, Ph. D. thesis (2007), [URL](#).
- Comanac, A., de' Medici, L., Capone, M. and Millis, A. J., Optical conductivity and the correlation strength of high-temperature copper-oxide superconductors, Nature Physics **4**, 287 (2008), [URL](#).
- DALTON2011, a molecular electronic structure program (2011), [URL](#).
- Damascelli, A., Hussain, Z. and Shen, Z.-X., Angle-resolved photoemission studies of the cuprate superconductors, Rev. Mod. Phys. **75**, 473 (2003), [URL](#).

- de Boer, J. H. and Verwey, E. J. W., Semi-conductors with partially and with completely filled  $3d$ -lattice bands, Proc. Phys. Soc. **49**, 59 (1937), [URL](#).
- de' Medici, L., Wang, X., Capone, M. and Millis, A. J., Correlation strength, gaps, and particle-hole asymmetry in high- $T_c$  cuprates: A dynamical mean field study of the three-band copper-oxide model, Phys. Rev. B **80**, 054501 (2009), [URL](#).
- Devereaux, T. P. and Hackl, R., Inelastic light scattering from correlated electrons, Rev. Mod. Phys. **79**, 175 (2007), [URL](#).
- Ding, H., Yokoya, T., Campuzano, J. C., Takahashi, T., Randeria, M., Norman, M. R., Mochiku, T., Kadowaki, K. and Giapintzakis, J., Spectroscopic evidence for a pseudogap in the normal state of underdoped high- $T_c$  superconductors, Nature **382**, 51 (1996), [URL](#).
- Dulić, D., Pimenov, A., van der Marel, D., Broun, D. M., Kamal, S., Hardy, W. N., Tsvetkov, A. A., Sutjaha, I. M., Liang, R., Menovsky, A. A., Loidl, A. and Saxena, S. S., Observation of the Transverse Optical Plasmon in  $\text{SmLa}_{0.8}\text{Sr}_{0.2}\text{CuO}_{4-\delta}$ , Phys. Rev. Lett. **86**, 4144 (2001), [URL](#).
- Elbio Dagotto, T. M. R., Surprises on the Way from One- to Two-Dimensional Quantum Magnets: The Ladder Materials, Science **271**, 618 (1996), [URL](#).
- Emery, V. J. and Kivelson, S. A., Importance of phase fluctuations in superconductors with small superfluid density, Nature **374**, 434 (1995), [URL](#).
- Fauqué, B., Sidis, Y., Hinkov, V., Pailhès, S., Lin, C. T., Chaud, X. and Bourges, P., Magnetic Order in the Pseudogap Phase of High- $T_C$  Superconductors, Phys. Rev. Lett. **96**, 197001 (2006), [URL](#).
- Ferrero, M., Cornaglia, P. S., De Leo, L., Parcollet, O., Kotliar, G. and Georges,

- A., Pseudogap opening and formation of Fermi arcs as an orbital-selective Mott transition in momentum space, *Phys. Rev. B* **80**, 064501 (2009), [URL](#).
- Ferrero, M., Cornaglia, P. S., Leo, L. D., Parcollet, O., Kotliar, G. and Georges, A., Valence bond dynamical mean-field theory of doped Mott insulators with nodal/antinodal differentiation, *EPL* **85**, 57009 (2009), [URL](#).
- Ferrero, M., Parcollet, O., Georges, A., Kotliar, G. and Basov, D. N., Interplane charge dynamics in a valence-bond dynamical mean-field theory of cuprate superconductors, *Phys. Rev. B* **82**, 054502 (2010), [URL](#).
- Feynman, R. P. and Vernon, F. L., The theory of a general quantum system interacting with a linear dissipative system, *Ann. Phys. (N.Y.)* **24**, 118 (1963), [URL](#).
- Fuhrmann, A., Okamoto, S., Monien, H. and Millis, A. J., Fictive-impurity approach to dynamical mean-field theory: A strong-coupling investigation, *Phys. Rev. B* **75**, 205118 (2007), [URL](#).
- García, D. J., Hallberg, K. and Rozenberg, M. J., Dynamical Mean Field Theory with the Density Matrix Renormalization Group, *Phys. Rev. Lett.* **93**, 246403 (2004), [URL](#).
- Georges, A., in Lectures on the physics of highly correlated electron systems VIII: Eighth Training Course in the Physics of Correlated Electron Systems and High- $T_c$  Superconductors, Salerno (Italy), edited by A. Avella and F. Mancini (AIP conference proceedings), volume 715, Chapter 1, “Strongly correlated electron materials: dynamical-mean-field theory and electronic structure”, p.3 (2004), [URL](#).
- Georges, A. and Kotliar, G., Hubbard model in infinite dimensions, *Phys. Rev. B* **45**, 6479 (1992), [URL](#).

- Georges, A., Kotliar, G., Krauth, W. and Rozenberg, M. J., Dynamical mean-field theory of strongly correlated fermion systems and the limit of infinite dimensions, *Rev. Mod. Phys.* **68**, 13 (1996), [URL](#).
- Gubernatis, J. E., Jarrell, M., Silver, R. N. and Sivia, D. S., Quantum Monte Carlo simulations and maximum entropy: Dynamics from imaginary-time data, *Phys. Rev. B* **44**, 6011 (1991), [URL](#).
- Gull, E., Ferrero, M., Parcollet, O., Georges, A. and Millis, A. J., Momentum-space anisotropy and pseudogaps: A comparative cluster dynamical mean-field analysis of the doping-driven metal-insulator transition in the two-dimensional Hubbard model, *Phys. Rev. B* **82**, 155101 (2010), [URL](#).
- Gull, E., Millis, A. J., Lichtenstein, A. I., Rubtsov, A. N., Troyer, M. and Werner, P., Continuous-time Monte Carlo methods for quantum impurity models, *Rev. Mod. Phys.* **83**, 349 (2011), [URL](#).
- Gull, E., Parcollet, O., Werner, P. and Millis, A. J., Momentum-sector-selective metal-insulator transition in the eight-site dynamical mean-field approximation to the Hubbard model in two dimensions, *Phys. Rev. B* **80**, 245102 (2009), [URL](#).
- Gull, E., Staar, P., Fuchs, S., Nukala, P., Summers, M. S., Pruschke, T., Schulthess, T. C. and Maier, T., Submatrix updates for the continuous-time auxiliary-field algorithm, *Phys. Rev. B* **83**, 075122 (2011), [URL](#).
- Gull, E., Werner, P., Parcollet, O. and Troyer, M., Continuous-time auxiliary-field Monte Carlo for quantum impurity models, *EPL* **82**, 57003 (2008), [URL](#).
- Gull, E., Werner, P., Wang, X., Troyer, M. and Millis, A. J., Local order and the gapped phase of the Hubbard model: A plaquette dynamical mean-field investigation, *EPL* **84**, 37009 (2008), [URL](#).

- Hachmann, J., Cardoen, W. and Chan, G. K.-L., Multireference correlation in long molecules with the quadratic scaling density matrix renormalization group, *J. Chem. Phys.* **125**, 144101 (2006), [URL](#).
- Hackl, R., Tassini, L., Venturini, F., Hartinger, C., Erb, A., Kikugawa, N. and Fujita, T., Ordering Phenomena in Cuprates, *Adv. in Solid State Phys.* **45**, 227 (2005), [URL](#).
- Haule, K. and Kotliar, G., Optical conductivity and kinetic energy of the superconducting state: A cluster dynamical mean field study, *EPL* **77**, 27007 (2007), [URL](#).
- Hehre, W. J., Stewart, R. F. and Pople, J. A., SelfConsistent MolecularOrbital Methods. I. Use of Gaussian Expansions of SlaterType Atomic Orbitals, *J. Chem. Phys.* **51**, 2657, [URL](#).
- Hettler, M. H., Mukherjee, M., Jarrell, M. and Krishnamurthy, H. R., Dynamical cluster approximation: Nonlocal dynamics of correlated electron systems, *Phys. Rev. B* **61**, 12739 (2000), [URL](#).
- Hettler, M. H., Tahvildar-Zadeh, A. N., Jarrell, M., Pruschke, T. and Krishnamurthy, H. R., Nonlocal dynamical correlations of strongly interacting electron systems, *Phys. Rev. B* **58**, R7475 (1998), [URL](#).
- Hirsch, J. E. and Fye, R. M., Monte Carlo Method for Magnetic Impurities in Metals, *Phys. Rev. Lett.* **56**, 2521 (1986), [URL](#).
- Hohenberg, P. and Kohn, W., Inhomogeneous Electron Gas, *Phys. Rev.* **136**, B864 (1964), [URL](#).
- Holzmann, M., Bernu, B., Olevano, V., Martin, R. M. and Ceperley, D. M., Renormalization factor and effective mass of the two-dimensional electron gas, *Phys. Rev. B* **79**, 041308 (2009), [URL](#).



- Homes, C. C., Timusk, T., Liang, R., Bonn, D. A. and Hardy, W. N., Optical conductivity of  $c$  axis oriented  $\text{YBa}_2\text{Cu}_3\text{O}_{6.70}$ : Evidence for a pseudogap, *Phys. Rev. Lett.* **71**, 1645 (1993), [URL](#).
- Hubbard, J., Electron Correlations in Narrow Energy Bands, *Proc. R. Soc. Lond. A* **276**, 238 (1963), [URL](#).
- Hüfner, S., Hossain, M. A., Damascelli, A. and Sawatzky, G. A., Two gaps make a high-temperature superconductor, *Rep. Prog. Phys.* **71**, 062501 (2008), [URL](#).
- Huscroft, C., Jarrell, M., Maier, T., Moukouri, S. and Tahvildarzadeh, A. N., Pseudogaps in the 2D Hubbard Model, *Phys. Rev. Lett.* **86**, 139 (2001), [URL](#).
- Hybertsen, M. S. and Louie, S. G., Electron correlation in semiconductors and insulators: Band gaps and quasiparticle energies, *Phys. Rev. B* **34**, 5390 (1986), [URL](#).
- Imada, M., Fujimori, A. and Tokura, Y., Metal-insulator transitions, *Rev. Mod. Phys.* **70**, 1039 (1998), [URL](#).
- Ito, T., Takenaka, K. and Uchida, S., Systematic deviation from  $T$ -linear behavior in the in-plane resistivity of  $\text{YBa}_2\text{Cu}_3\text{O}_{7-y}$ : Evidence for dominant spin scattering, *Phys. Rev. Lett.* **70**, 3995 (1993), [URL](#).
- Jacob, D., Haule, K. and Kotliar, G., Dynamical mean-field theory for molecular electronics: Electronic structure and transport properties, *Phys. Rev. B* **82**, 195115 (2010), [URL](#).
- Jaklič, J. and Prelovšek, P., Finite-temperature properties of doped antiferromagnets, *Advances in Physics* **49**, 1 (2000), [URL](#).
- Jarrell, M., Freericks, J. K. and Pruschke, T., Optical conductivity of the infinite-dimensional Hubbard model, *Phys. Rev. B* **51**, 11704 (1995), [URL](#).

- Jarrell, M. and Gubernatis, J., Bayesian inference and the analytic continuation of imaginary-time quantum Monte Carlo data, *Physics Reports* **269**, 133 (1996), [URL](#).
- Katsufuji, T., Tokura, Y., Ido, T. and Uchida, S., Symmetry-dependent electronic Raman scattering in  $\text{La}_{2-x}\text{Sr}_x\text{CuO}_4$ : Evidence for doping-induced change in the  $k$ -space anisotropy of charge dynamics, *Phys. Rev. B* **48**, 16131 (1993), [URL](#).
- Keiner, J., Kunis, S. and Potts, D., Using NFFT 3 - A Software Library for Various Nonequispaced Fast Fourier Transforms, *ACM Trans. Math. Software* **36**, 19:1 (2009), [URL](#).
- Kivelson, S. A., Fradkin, E. and Emery, V. J., Electronic liquid-crystal phases of a doped Mott insulator, *Nature* **393**, 550 (1998), [URL](#).
- Koch, E., Sangiovanni, G. and Gunnarsson, O., Sum rules and bath parametrization for quantum cluster theories, *Phys. Rev. B* **78**, 115102 (2008), [URL](#).
- Kohn, W. and Sham, L. J., Self-Consistent Equations Including Exchange and Correlation Effects, *Phys. Rev.* **140**, A1133 (1965), [URL](#).
- Kotliar, G. and Liu, J., Superexchange mechanism and  $d$ -wave superconductivity, *Phys. Rev. B* **38**, 5142 (1988), [URL](#).
- Kotliar, G., Savrasov, S. Y., Haule, K., Oudovenko, V. S., Parcollet, O. and Marianetti, C. A., Electronic structure calculations with dynamical mean-field theory, *Rev. Mod. Phys.* **78**, 865 (2006), [URL](#).
- Kotliar, G., Savrasov, S. Y., Pálsson, G. and Biroli, G., Cellular Dynamical Mean Field Approach to Strongly Correlated Systems, *Phys. Rev. Lett.* **87**, 186401 (2001), [URL](#).

- Kyung, B., Kancharla, S. S., Sénéchal, D., Tremblay, A.-M. S., Civelli, M. and Kotliar, G., Pseudogap induced by short-range spin correlations in a doped Mott insulator, Phys. Rev. B **73**, 165114 (2006), [URL](#).
- Landsberg, G. S. and Mandelstam, L. I., Eine neue Erscheinung bei der Lichtzerstreuung in Krystallen, Naturwissenschaften **16**, 557 (1928), [URL](#).
- Lawson, C. L. and Hanson, R. J., *Solving Least Squares Problems*, Society for Industrial and Applied Mathematics, Philadelphia (1995).
- Lee, P. A. and Nagaosa, N., Gauge theory of the normal state of high- $T_c$  superconductors, Phys. Rev. B **46**, 5621 (1992), [URL](#).
- Lee, P. A., Rice, T. M. and Anderson, P. W., Fluctuation Effects at a Peierls Transition, Phys. Rev. Lett. **31**, 462 (1973), [URL](#).
- Lichtenstein, A. I. and Katsnelson, M. I., Antiferromagnetism and d-wave superconductivity in cuprates: A cluster dynamical mean-field theory, Phys. Rev. B **62**, R9283 (2000), [URL](#).
- Lieb, E. H. and Wu, F. Y., Absence of Mott Transition in an Exact Solution of the Short-Range, One-Band Model in One Dimension, Phys. Rev. Lett. **20**, 1445 (1968), [URL](#).
- Lieb, E. H. and Wu, F. Y., The one-dimensional Hubbard model: a reminiscence, Physica A: Statistical Mechanics and its Applications **321**, 1 (2003), [URL](#).
- Liebsch, A. and Tong, N.-H., Finite-temperature exact diagonalization cluster dynamical mean-field study of the two-dimensional Hubbard model: Pseudogap, non-Fermi-liquid behavior, and particle-hole asymmetry, Phys. Rev. B **80**, 165126 (2009), [URL](#).

- Lin, N., Gull, E. and Millis, A. J., Optical conductivity from cluster dynamical mean-field theory: Formalism and application to high-temperature superconductors, *Phys. Rev. B* **80**, 161105 (2009), [URL](#).
- Lin, N., Gull, E. and Millis, A. J., Physics of the pseudogap in eight-site cluster dynamical mean-field theory: Photoemission, Raman scattering, and in-plane and *c*-axis conductivity, *Phys. Rev. B* **82**, 045104 (2010), [URL](#).
- Lin, N., Marianetti, C. A., Millis, A. J. and Reichman, D. R., Dynamical Mean-Field Theory for Quantum Chemistry, *Phys. Rev. Lett.* **106**, 096402 (2011), [URL](#).
- Loeser, A. G., Shen, Z.-X., Dessau, D. S., Marshall, D. S., Park, C. H., Fournier, P. and Kapitulnik, A., Excitation Gap in the Normal State of Underdoped  $\text{Bi}_2\text{Sr}_2\text{CaCu}_2\text{O}_{8+\delta}$ , *Science* **273**, 325 (1996), [URL](#).
- Luttinger, J. M. and Ward, J. C., Ground-State Energy of a Many-Fermion System. II, *Phys. Rev.* **118**, 1417 (1960), [URL](#).
- Macridin, A., Jarrell, M., Maier, T., Kent, P. R. C. and D'Azevedo, E., Pseudogap and Antiferromagnetic Correlations in the Hubbard Model, *Phys. Rev. Lett.* **97**, 036401 (2006), [URL](#).
- Maier, T., Jarrell, M., Pruschke, T. and Hettler, M. H., Quantum cluster theories, *Rev. Mod. Phys.* **77**, 1027 (2005), [URL](#).
- Maple, M. B., Bauer, E. D., Zapf, V. S. and Wosnitza, J., Unconventional Superconductivity in Novel Materials, in *Superconductivity*, p. 639 (2008), [URL](#).
- Metzner, W. and Vollhardt, D., Correlated Lattice Fermions in  $d = \infty$  Dimensions, *Phys. Rev. Lett.* **62**, 324 (1989), [URL](#).

- Millis, A. J., in *Strong Interactions in Low Dimensions*, edited by Baeriswyl, D. and Degiorgi, L., chap. 7, “Optical conductivity and correlated electron physics”, p. 195, Kluwer Academic Publishers (2004), [URL](#).
- Millis, A. J. and Monien, H., Spin Gaps and Spin Dynamics in  $\text{La}_{2-x}\text{Sr}_x\text{CuO}_4$  and  $\text{YBa}_2\text{Cu}_3\text{O}_{7-\delta}$ , *Phys. Rev. Lett.* **70**, 2810 (1993), [URL](#).
- Millis, A. J., Zimmers, A., Lobo, R. P. S. M., Bontemps, N. and Homes, C. C., Mott physics and the optical conductivity of electron-doped cuprates, *Phys. Rev. B* **72**, 224517 (2005), [URL](#).
- Møller, C. and Plesset, M. S., Note on an Approximation Treatment for Many-Electron Systems, *Phys. Rev.* **46**, 618 (1934), [URL](#).
- Mott, N. F., *The Basis of the Electron Theory of Metals, with Special Reference to the Transition Metals*, *Proc. Phys. Soc. A* **62**, 416 (1949), [URL](#).
- Mott, N. F., On the Transition to Metallic Conduction in Semiconductors, *Canadian Journal of Physics* **34**, 1356 (1956), [URL](#).
- Mott, N. F., Metal-Insulator Transition, *Rev. Mod. Phys.* **40**, 677 (1968), [URL](#).
- Mott, N. F. and Peierls, R., Discussion of the paper by de Boer and Verwey, *Proc. Phys. Soc.* **49**, 72 (1937), [URL](#).
- Negele, J. W. and Orland, H., *Quantum Many-Particle Systems*, Addison-Wesley, Reading, MA (1988).
- Nemetschek, R., Opel, M., Hoffmann, C., Müller, P. F., Hackl, R., Berger, H., Forró, L., Erb, A. and Walker, E., Pseudogap and Superconducting Gap in the Electronic Raman Spectra of Underdoped Cuprates, *Phys. Rev. Lett.* **78**, 4837 (1997), [URL](#).

- Orenstein, J., Thomas, G. A., Millis, A. J., Cooper, S. L., Rapkine, D. H., Timusk, T., Schneemeyer, L. F. and Waszczak, J. V., Frequency- and temperature-dependent conductivity in  $\text{YBa}_2\text{Cu}_3\text{O}_{6+x}$  crystals, *Phys. Rev. B* **42**, 6342 (1990), [URL](#).
- Parcollet, O., Biroli, G. and Kotliar, G., Cluster Dynamical Mean Field Analysis of the Mott Transition, *Phys. Rev. Lett.* **92**, 226402 (2004), [URL](#).
- Park, H., Haule, K. and Kotliar, G., Cluster Dynamical Mean Field Theory of the Mott Transition, *Phys. Rev. Lett.* **101**, 186403 (2008), [URL](#).
- Pople, J. A. and Nesbet, R. K., Self-Consistent Orbitals for Radicals, *J. Chem. Phys.* **22**, 571 (1954), [URL](#).
- Potthoff, M., Wegner, T. and Nolting, W., Interpolating self-energy of the infinite-dimensional Hubbard model: Modifying the iterative perturbation theory, *Phys. Rev. B* **55**, 16132 (1997), [URL](#).
- Prelovšek, P. and Jaklič, J., Raman response in doped antiferromagnets, *Phys. Rev. B* **53**, 15095 (1996), [URL](#).
- Rabani, E., Reichman, D. R., Krilov, G. and Berne, B. J., The calculation of transport properties in quantum liquids using the maximum entropy numerical analytic continuation method: Application to liquid para-hydrogen, *Proc. Natl. Acad. Sci.* **99**, 1129 (2002), [URL](#).
- Raman, C. V. and Krishnan, K. S., A New Type of Secondary Radiation, *Nature* **121**, 501 (1928), [URL](#).
- Renner, C., Revaz, B., Genoud, J.-Y., Kadowaki, K. and Fischer, O., Pseudogap Precursor of the Superconducting Gap in Under- and Overdoped  $\text{Bi}_2\text{Sr}_2\text{CaCu}_2\text{O}_{8+\delta}$ , *Phys. Rev. Lett.* **80**, 149 (1998), [URL](#).

- Reznik, D., Cooper, S. L., Klein, M. V., Lee, W. C., Ginsberg, D. M., Maksimov, A. A., Puchkov, A. V., Tartakovskii, I. I. and Cheong, S.-W., Plane-polarized Raman continuum in the insulating and superconducting layered cuprates, *Phys. Rev. B* **48**, 7624 (1993), [URL](#).
- Roothaan, C. C. J., *New Developments in Molecular Orbital Theory*, *Rev. Mod. Phys.* **23**, 69 (1951), [URL](#).
- Rotter, L. D., Schlesinger, Z., Collins, R. T., Holtzberg, F., Field, C., Welp, U. W., Crabtree, G. W., Liu, J. Z., Fang, Y., Vandervoort, K. G. and Fleshler, S., Dependence of the infrared properties of single-domain  $\text{YBa}_2\text{Cu}_3\text{O}_{7-y}$  on oxygen content, *Phys. Rev. Lett.* **67**, 2741 (1991), [URL](#).
- Rübhausen, M., Hammerstein, O. A., Bock, A., Merkt, U., Rieck, C. T., Guptasarma, P., Hinks, D. G. and Klein, M. V., Doping Dependence of the Electronic Interactions in Bi-2212 Cuprate Superconductors: Doped Antiferromagnets or Antiferromagnetic Fermi Liquids?, *Phys. Rev. Lett.* **82**, 5349 (1999), [URL](#).
- Rubtsov, A. N., Savkin, V. V. and Lichtenstein, A. I., Continuous-time quantum Monte Carlo method for fermions, *Phys. Rev. B* **72**, 035122 (2005), [URL](#).
- Sakai, O. and Kuramoto, Y., Application of the numerical renormalization group method to the hubbard model in infinite dimensions, *Solid State Communications* **89**, 307 (1994), [URL](#).
- Sakai, S., Motome, Y. and Imada, M., Evolution of Electronic Structure of Doped Mott Insulators: Reconstruction of Poles and Zeros of Green's Function, *Phys. Rev. Lett.* **102**, 056404 (2009), [URL](#).
- Sakai, S., Motome, Y. and Imada, M., Doped high- $T_c$  cuprate superconductors elucidated in the light of zeros and poles of the electronic Green's function, *Phys. Rev. B* **82**, 134505 (2010), [URL](#).

- Sandvik, A. W., Capponi, S., Poilblanc, D. and Dagotto, E., Numerical calculations of the  $B_{1g}$  Raman spectrum of the two-dimensional Heisenberg model, Phys. Rev. B **57**, 8478 (1998), [URL](#).
- Santander-Syro, A. F., Lobo, R. P. S. M., Bontemps, N., Konstantinovic, Z., Li, Z. Z. and Raffy, H., Pairing in cuprates from high-energy electronic states, EPL **62**, 568 (2003), [URL](#).
- Schachinger, E., Tu, J. J. and Carbotte, J. P., Angle-resolved photoemission spectroscopy and optical renormalizations: Phonons or spin fluctuations, Phys. Rev. B **67**, 214508 (2003), [URL](#).
- Schilling, A., Cantoni, M., Guo, J. D. and Ott, H. R., Superconductivity above 130 K in the Hg-Ba-Ca-Cu-O system, Nature **363**, 56 (1993), [URL](#).
- Schmalian, J., Pines, D. and Stojković, B., Weak Pseudogap Behavior in the Underdoped Cuprate Superconductors, Phys. Rev. Lett. **80**, 3839 (1998), [URL](#).
- Schollwöck, U., The density-matrix renormalization group, Rev. Mod. Phys. **77**, 259 (2005), [URL](#).
- Schreiffer, J. R., *Theory of Superconductivity*, Perseus Books (1999).
- Shah, N. and Millis, A. J., Superconductivity, phase fluctuations, and the  $c$ -axis conductivity of bilayer high-temperature superconductors, Phys. Rev. B **65**, 024506 (2001), [URL](#).
- Sharma, S., Dewhurst, J. K., Lathiotakis, N. N. and Gross, E. K. U., Reduced density matrix functional for many-electron systems, Phys. Rev. B **78**, 201103 (2008), [URL](#).
- Shavitt, I., The history and evolution of configuration interaction, Molecular Physics **94**, 3 (1998), [URL](#).



- Silver, R. N., Sivia, D. S. and Gubernatis, J. E., Maximum-entropy method for analytic continuation of quantum Monte Carlo data, *Phys. Rev. B* **41**, 2380 (1990), [URL](#).
- Sommerfeld, A., Zur Elektronentheorie der Metalle auf Grund der Fermischen Statistik, *Z. Phys.* **47**, 1 (1928), [URL](#).
- Sonier, J. E., Pacradouni, V., Sabok-Sayr, S. A., Hardy, W. N., Bonn, D. A., Liang, R. and Mook, H. A., Detection of the Unusual Magnetic Orders in the Pseudogap Region of a High-Temperature Superconducting  $\text{YBa}_2\text{Cu}_3\text{O}_{6.6}$  Crystal by Muon-Spin Relaxation, *Phys. Rev. Lett.* **103**, 167002 (2009), [URL](#).
- Sordi, G., Haule, K. and Tremblay, A.-M. S., Finite Doping Signatures of the Mott Transition in the Two-Dimensional Hubbard Model, *Phys. Rev. Lett.* **104**, 226402 (2010), [URL](#).
- Stanescu, T. D. and Kotliar, G., Fermi arcs and hidden zeros of the Green function in the pseudogap state, *Phys. Rev. B* **74**, 125110 (2006), [URL](#).
- Sugai, S., Suzuki, H., Takayanagi, Y., Hosokawa, T. and Hayamizu, N., Carrier-density-dependent momentum shift of the coherent peak and the LO phonon mode in  $p$ -type high- $T_c$  superconductors, *Phys. Rev. B* **68**, 184504 (2003), [URL](#).
- Tajima, S., Schützmann, J., Miyamoto, S., Terasaki, I., Sato, Y. and Hauff, R., Optical study of  $c$ -axis charge dynamics in  $\text{YBa}_2\text{Cu}_3\text{O}_y$ :nnCarrier self-confinement in the normal and the superconducting states, *Phys. Rev. B* **55**, 6051 (1997), [URL](#).
- Takahashi, H., Igawa, K., Arii, K., Kamihara, Y., Hirano, M. and Hosono, H., Superconductivity at 43K in an iron-based layered compound  $\text{LaO}_{1-x}\text{F}_x\text{FeAs}$ , *Nature* **453**, 376 (2008), [URL](#).

- Timusk, T., Homes, C. C. and Reichardt, W., in International Workshop on the Anharmonic Properties of High  $T_c$  Cuprates, Bled (Slovenia), edited by G. Ruani (World Scientific, Singapore), p.121 (1995).
- Timusk, T. and Statt, B., The pseudogap in high-temperature superconductors: an experimental survey, *Rep. Prog. Phys.* **62**, 61 (1999), [URL](#).
- Tokura, Y., Takagi, H. and Uchida, S., A superconducting copper oxide compound with electrons as the charge carriers, *Nature* **337**, 345 (1989), [URL](#).
- Tranquada, J. M., Lorenzo, J. E., Buttrey, D. J. and Sachan, V., Cooperative ordering of holes and spins in  $\text{La}_2\text{NiO}_{4.125}$ , *Phys. Rev. B* **52**, 3581 (1995), [URL](#).
- Tsuchimochi, T. and Scuseria, G. E., Strong correlations via constrained-pairing mean-field theory, *J. Chem. Phys.* **131**, 121102 (2009), [URL](#).
- Uchida, S., Ido, T., Takagi, H., Arima, T., Tokura, Y. and Tajima, S., Optical spectra of  $\text{La}_{2-x}\text{Sr}_x\text{CuO}_4$ : Effect of carrier doping on the electronic structure of the  $\text{CuO}_2$  plane, *Phys. Rev. B* **43**, 7942 (1991), [URL](#).
- Varma, C. M., Theory of the pseudogap state of the cuprates, *Phys. Rev. B* **73**, 155113 (2006), [URL](#).
- Varma, C. M., Littlewood, P. B., Schmitt-Rink, S., Abrahams, E. and Ruckenstein, A. E., Phenomenology of the normal state of Cu-O high-temperature superconductors, *Phys. Rev. Lett.* **63**, 1996 (1989), [URL](#).
- Venturini, F., Opel, M., Devereaux, T. P., Freericks, J. K., Tüttő, I., Revaz, B., Walker, E., Berger, H., Forró, L. and Hackl, R., Observation of an Unconventional Metal-Insulator Transition in Overdoped  $\text{CuO}_2$  Compounds, *Phys. Rev. Lett.* **89**, 107003 (2002), [URL](#).

- Verstraete, F., Murg, V. and Cirac, J. I., Matrix product states, projected entangled pair states, and variational renormalization group methods for quantum spin systems, *Advances in Physics* **57**, 143 (2008), [URL](#).
- Vidhyadhiraja, N. S., Macridin, A., Şen, C., Jarrell, M. and Ma, M., Quantum Critical Point at Finite Doping in the 2D Hubbard Model: A Dynamical Cluster Quantum Monte Carlo Study, *Phys. Rev. Lett.* **102**, 206407 (2009), [URL](#).
- Vilk, Y. and Tremblay, A.-M., Non-Perturbative Many-Body Approach to the Hubbard Model and Single-Particle Pseudogap, *J. Phys. I France* **7**, 1309 (1997), [URL](#).
- Wang, X., Dang, H. T. and Millis, A. J.,  $d_3z^2-r^2$  orbital in high- $T_c$  cuprates: Excitonic spectrum, metal-insulator phase diagram, optical conductivity, and orbital character of doped holes, *Phys. Rev. B* **84**, 014530 (2011), [URL](#).
- Wang, X., de' Medici, L. and Millis, A. J., Role of oxygen-oxygen hopping in the three-band copper-oxide model: Quasiparticle weight, metal insulator and magnetic phase boundaries, gap values, and optical conductivity, *Phys. Rev. B* **83**, 094501 (2011), [URL](#).
- Wang, X., Gull, E., de' Medici, L., Capone, M. and Millis, A. J., Antiferromagnetism and the gap of a Mott insulator: Results from analytic continuation of the self-energy, *Phys. Rev. B* **80**, 045101 (2009), [URL](#).
- Wang, Y., Ong, N. P., Xu, Z. A., Kakeshita, T., Uchida, S., Bonn, D. A., Liang, R. and Hardy, W. N., High Field Phase Diagram of Cuprates Derived from the Nernst Effect, *Phys. Rev. Lett.* **88**, 257003 (2002), [URL](#).
- Warren, W. W., Walstedt, R. E., Brennert, G. F., Cava, R. J., Tycko, R., Bell, R. F. and Dabbagh, G., Cu spin dynamics and superconducting precursor effects in planes above  $T_c$  in  $\text{YBa}_2\text{Cu}_3\text{O}_{6.7}$ , *Phys. Rev. Lett.* **62**, 1193 (1989), [URL](#).

- Werner, P., Comanac, A., de' Medici, L., Troyer, M. and Millis, A. J., Continuous-Time Solver for Quantum Impurity Models, *Phys. Rev. Lett.* **97**, 076405 (2006), [URL](#).
- Werner, P., Gull, E., Parcollet, O. and Millis, A. J., Momentum-selective metal-insulator transition in the two-dimensional Hubbard model: An 8-site dynamical cluster approximation study, *Phys. Rev. B* **80**, 045120 (2009), [URL](#).
- White, S. R., Density-matrix algorithms for quantum renormalization groups, *Phys. Rev. B* **48**, 10345 (1993), [URL](#).
- White, S. R. and Martin, R. L., Ab initio quantum chemistry using the density matrix renormalization group, *J. Chem. Phys.* **110**, 4127 (1999), [URL](#).
- Wilson, K. G., The renormalization group: Critical phenomena and the Kondo problem, *Rev. Mod. Phys.* **47**, 773 (1975), [URL](#).
- Yu, L., Munzar, D., Boris, A. V., Yordanov, P., Chaloupka, J., Wolf, T., Lin, C. T., Keimer, B. and Bernhard, C., Evidence for Two Separate Energy Gaps in Underdoped High-Temperature Cuprate Superconductors from Broadband Infrared Ellipsometry, *Phys. Rev. Lett.* **100**, 177004 (2008), [URL](#).
- Zaanen, J., Sawatzky, G. A. and Allen, J. W., Band gaps and electronic structure of transition-metal compounds, *Phys. Rev. Lett.* **55**, 418 (1985), [URL](#).
- Zhang, Y. Z. and Imada, M., Pseudogap and Mott transition studied by cellular dynamical mean-field theory, *Phys. Rev. B* **76**, 045108 (2007), [URL](#).

# Curriculum Vitae

**Nan Lin**

928 Pupin, Mail Code 5277  
538 West 120th Street  
New York, NY 10027, USA

TEL: (347) 604-0661  
Email: linnan12@phys.columbia.edu

## BIOGRAPHICAL DATA

---

Year and Place of Birth	1984, Fujian, P. R. China
Citizenship	Citizen of P. R. China

## RESEARCH INTEREST

---

Theoretical Condensed Matter Physics: strongly correlated electrons, superconductivity, optical conductivity and related probes, dynamical mean-field theory.

## EDUCATION

---

- 2006 - Graduate studies at Department of Physics, Columbia University in the city of New York. Advisor: Prof. Andrew J. Millis and Prof. David R. Reichman. M.A. degree received in February 2008, M.Phil. received in October 2010. Ph.D. degree is expected in October 2012.
- 2002 - 2006 Undergraduate studies in Department of Materials Science and Engineering, University of Science and Technology of China, Anhui, China. B. S. degree received in June 2006.

## AWARDS

---

- Faculty Teaching Fellowship, Columbia University, 2006.
- Guo Moruo Scholarship (the supreme honor of USTC), USTC, 2005.
- Outstanding Student Scholarship (Grade One), USTC, 2005.

- MEDY Scholarship, USTC, 2004.
- National Scholarship (Grade Two), USTC, 2003.

## PUBLICATIONS

---

### Peer Reviewed Publications

1. Dynamical Mean-Field Theory for Quantum Chemistry  
**Nan Lin**, C. A. Marianetti, Andrew J. Millis, and David R. Reichman  
*Phys. Rev. Lett.* **106**, 096402 (2011)
2. Physics of the pseudogap in eight-site cluster dynamical mean-field theory: photoemission, Raman scattering, and in-plane and  $c$ -axis conductivity  
**Nan Lin**, Emanuel Gull, and Andrew J. Millis  
*Phys. Rev. B* **82**, 045104 (2010)
3. Optical conductivity from cluster dynamical mean-field theory: Formalism and application to high-temperature superconductors  
**Nan Lin**, Emanuel Gull, and Andrew J. Millis  
*Phys. Rev. B* **80**, 161105(R) (2009) (Editor's Suggestion)

## CONTRIBUTED PRESENTATIONS

---

1. Dynamical mean-field theory for transition metal dioxide molecules, Boston, MA, APS March Meeting, Mar 2nd, 2012.
2. Dynamical Mean-Field Theory for Quantum Chemistry, Dallas, TX, APS March meeting, Mar 23th, 2011.
3. Dynamical Mean-Field Theory for Quantum Chemistry, New York, NY, 4th Gotham-Metro Condensed Matter Meeting, New York Academy of Sciences, November 12nd, 2010.
4. Poster: Physics of the pseudogap in eight-site cluster dynamical mean-field theory: Photoemission, Raman scattering, and in-plane and  $c$ -axis conductivity, Boulder, CO, Boulder summer school for condensed matter and materials physics, July 15th, 2010.
5. Optical conductivity from cluster dynamical mean-field theory: Formalism and application to high-temperature superconductors, Portland, OR, APS March meeting, March 16th, 2010.

6. Poster: Optical conductivity from cluster dynamical mean-field theory: Formalism and application to high-temperature superconductors, New York, NY, 2nd Gotham-Metro Condensed Matter Meeting, New York Academy of Sciences, November 21st, 2009.

#### TEACHING EXPERIENCE

---

- Teaching assistant for General physics lab (Spring 2007, Fall 2010, Spring 2011)
- Preceptor/Head TA of Physics Department (Fall 2007, Spring 2008)
- Teaching assistant for Electromagnetic waves & optics (Prof. Szabolcs Marka, Fall 2007), Electricity-magnetism (Prof. Alberto Nicolis, Spring 2008), Statistical Mechanics (Prof. Malvin Ruderman, Fall 2010)